Computational Investigations of Boundary Condition Effects on Simulations of Thermoacoustic Instabilities

Qingzhao Wang

Dissertation submitted to the faculty of the
Virginia Polytechnic Institute and State University
in partial fulfillment of the requirements for the degree of

Doctor of Philosophy
in
Mechanical Engineering

Robert L. West, Chair
Uri Vandsburger
Jeffrey T. Borggaard
Danesh K. Tafti
Brian Vick

June 1st, 2015
Blacksburg, Virginia

Keywords: thermoacoustic instability; CFD; CSEM.

Computational Investigations of Boundary Condition Effects on Simulations of Thermoacoustic Instabilities

Qingzhao Wang

ABSTRACT

This dissertation presents a formulation of the Continuous Sensitivity Equation Method (CSEM) applied to the Computational Fluid Dynamics (CFD) simulation of thermoacoustic instability problems. The proposed sensitivity analysis approach only requires a single run of the CFD simulation. Moreover, the sensitivities of field variables, pressure, velocity and temperature to boundary-condition parameters are directly obtained from the solution to sensitivity equations. Thermoacoustic instability is predicted by the Rayleigh criterion. The sensitivity of the Rayleigh index is computed utilizing the sensitivities of field variables.

The application of the CSEM to thermoacoustic instability problems is demonstrated by two classic examples. The first example explores the effects of the heated wall temperature on the one-dimensional thermoacoustic convection. The sensitivity of the Rayleigh index, which is the indicator of thermoacoustic instabilities, is computed by the sensitivity of field variables. As the heat wall temperature increases, the sensitivity of the Rayleigh index decreases. The evolution from positive to negative sensitivity values suggests the transition from a destabilizing trend to stabilizing trend of the thermoacoustic system.

Thermoacoustic instabilities in a self-excited Rijke tube are investigated following the relatively simple thermoacoustic convection problem. The complexity of simulating the Rijke tube increases in both dimensions and mechanisms which incorporate the species transport process and chemical reactions. As a representative model of the large lean premixed combustor, Rijke tube has been extensively studied. Quantitative sensitivity analysis sets the present work apart from previous research on the prediction and control of thermoacoustic instabilities. The effects of two boundary-condition parameters, i.e. the inlet mass flow rate and the equivalence

ratio, are tested respectively. Small variations in both parameters predict a rapid change in sensitivities of field variables in the early stage of the total time length of 1.2s with a time step size of 1 μs for numerical simulations. The sensitivity of the Rayleigh index "blows up" at a specific time point of the early stage. In addition, variations in the inlet mass flow rate and the equivalence ratio lead to opposite effects on the sensitivity of the Rayleigh index.

There exist some common findings on the application of the CSEM. For both thermoacoustic problems, the sensitivities of field variables and the Rayleigh index exhibit oscillatory nature, confirming that thermoacoustic instability is an overall effect of the coupling process between fluctuations of pressure and heat release rate. All the sensitivities of the Rayleigh index show rapid changes and "blow up" in the early stage. Although the numerical errors could influence the fidelity of computational results, it is believed that the rapid changes reflect the susceptibility to thermoacoustic instabilities in the studied systems. It should also be noted that the sensitivities are obtained for small variations in influential parameters. Therefore, the resulting sensitivities do not predict the occurrence of thermoacoustic instabilities under a condition that is far from the reference state determined by either CFD simulation results (employed in this dissertation) or experimental data.

The sensitivity solver developed for the present research has the feature of flexibility. Additional mechanisms and more complicated instability criteria could be easily incorporated into the solver. Moreover, the sensitivity equations formulated in this dissertation are derived from the full set of nonlinear governing equations. Therefore, it is possible to extend the use of the sensitivity solver to other CFD problems. The developed sensitivity solver needs to be optimized to gain better performance, which is considered to be the primary future work of this research.

Acknowledgments

I would like to thank my advisor Professor Robert West for his guidance and encouragement throughout my doctoral studies. He is an amazing advisor who always listens to my opinions and trusts my own judgment. The numerous discussions on this project brought me into this wonderful world of sensitivity analysis of thermoacoustic instabilities, and taught me to think as a researcher.

I also would like to thank my co-advisor Professor Uri Vandsburger. He shared his experiences in China, which made me feel warm. He also shared his knowledge in combustion, which helped my understanding of the fundamental aspects of this research.

Thanks also to Professor Jeff Borggaard, Professor Danesh Tafti and Profesosr Brian Vick for serving on my committee and their suggestions and encouragement.

I am also very grateful to my colleagues and friends for their help and support. Ben Poe and James Archual have always been helpful whenever my work station gets naughty. All our research group members have been so friendly and all the friends of mine have been so lovely. Because of them, my life has been colorful in this place far from home.

Finally, I would like to express my love to my parents and other family members. I spent so little time with them and owed them a lot. I always feel that I am the luckiest kid dwelling in their endless love.

This project was funded by the United States Department of Energy. Their financial support is also gratefully acknowledged.

Contents

List of Figures

List of Tables

Chapter 1

Introduction

1.1 Motivation

Increasing awareness of environmental issues and stringent emission legislation have led to the use of lean premixed combustion technology in gas turbine engines. Lean premixed combustion has brought NO_x emissions down to a significantly low level by decreasing the combustion temperature. However, the combustion systems operated under lean premixed condition are more susceptible to thermoacoustic instabilities. Thermoacoustic instabilities in the combustion systems are observed as large pressure oscillations causing loud noise, violent vibration, performance degradation, structural destruction, and cost in time and economy. Because of the impact on the limits of flame blow-off and flame flashback, and the occurrence of thermoacoustic instabilities, the use of alternative fuels due to the increasing demand for energy became a challenge to the design and operability of gas turbine engines. The large variations in the composition of alternative fuels influence characteristics of combustion processes, and consequently affect the condition under which thermoacoustic instabilities occur. Experience in developing low emission gas turbines for conventional fuels like natural gas may not be feasible for syngas and high-hydrogen fuels which have significant variations in composition. The consequences are an estimated cost of one billion dollars annually for the repair and replacement of structural components that are destroyed by thermoacoustic instability related problems, as well as the cost due to the downtime of the equipment [1]. It is essential to understand the

mechanisms of thermoacoustic instabilities, predict their occurrence under different operating conditions, and improve the design of gas turbine engines with high performance and low emissions.

1.1.1 Background on thermoacoustic instabilities

Thermoacoustic instability exists in many industrial activities. Although thermoacoustic instabilities are used for developing thermoacoustic engines, thermoacoustic instabilities are generally undesirable for their destructive power, from thermoacoustic vibrations in the furnace system to combustion-driven thermoacoustic instabilities in the lean premixed gas turbine engine.

Thermoacoustic instability is a complicated phenomenon involving the interaction of fluctuations in pressure, flow velocity, heat release rate, etc. The essential process responsible for thermoacoustic instabilities was first explained by Rayleigh [2]. If the heat release fluctuations are in phase with the pressure oscillations in time, the unsteady heat additions amplify the acoustic oscillations. The explanation of the condition under which thermoacoustic instabilities may occur is called Rayleigh criterion which constitutes the basis for the subsequent investigations of thermoacoustic instabilities.

In the combustion system of a gas turbine engine, combustion processes are subject to change due to variations in the flow in time. There are two major mechanisms responsible for the generation of unsteady heat release in the premixed combustion systems. One is flow unsteadiness. The oscillating velocity or mass flux in the flame region causes fluctuations in the burning rate of the fuel and air mixture. Vortex structures in the flow induce rapid changes in the flow rate of reactants which perturb the reaction rate. The other big factor is inhomogeneity of the fuel and air mixture. Uneven mixing caused by pressure or velocity disturbance convects from the fuel injection point to the flame, changing the flame behaviors and exciting heat release fluctuations. When the fluctuations of pressure and heat release rate are in phase, unsteady heat release is fed into the acoustic field, while there is usually not enough damping in the combustion system of gas turbines to suppress the growth of pressure oscillations. Acoustic pressure oscillations grow in time until they reach some “saturated” status, which is referred to as the limit cycle in which the amplitude of pressure oscillations remains constant. Figure 1.1 depicts interactions between flow, acoustics and heat release in a thermoacoustic system.

Acoustic waves play an important role in the feedback path by perturbing combustion processes in the combustion chamber and affecting the fuel and air mixing at the flow inlet. The propagation of acoustic waves relates the boundary conditions with heat sources, driving the system instabilities at certain frequencies.

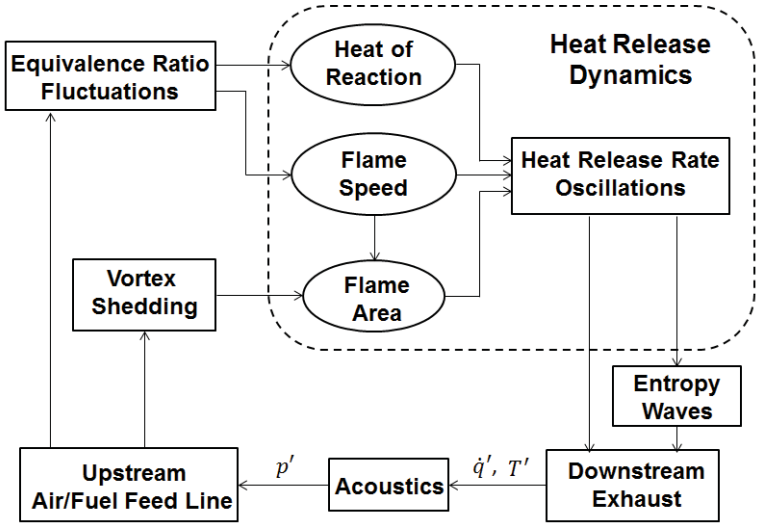

Figure 1.1: Relevant elements of combustion-driven thermoacoustic instabilities.

As an interdisciplinary subject, the study of thermoacoustic instabilities requires a wide range of knowledge. The physical phenomenon itself involves fluid dynamics (laminar or turbulent, reacting, compressible flow), heat transfer (conduction, convection and radiation), combustion (flame dynamics), and acoustics. The tools for exploring the mechanisms of this phenomenon are numerous. Experimental, analytical and numerical studies on thermoacoustic instabilities have been carried out. Unsteady simulation, linear stability analysis, and acoustic energy budget are effective approaches to assess the stability of a thermoacoustic system. Computational Aeroacoustics, Computational Fluid Dynamics (CFD), Network Models and Galerkin Methods are popular approaches to model the onset of thermoacoustic instability. Because of the interdisciplinary nature, thermoacoustic instabilities have attracted researchers from different areas with different backgrounds.

1.1.2 State of the art

There are intensive efforts put into understanding the mechanisms and control of the occurrence of thermoacoustic instabilities. These efforts are not limited to exploring thermoacoustic instabilities in modern gas turbines, previous studies on solid and liquid rockets, ramjets and other thermoacoustic systems also provide substantial insight into the nature of thermoacoustic instabilities.

Thermoacoustic instabilities have been investigated experimentally, theoretically and numerically. Experimental investigations have revealed important factors that influence stabilities in different thermoacoustic systems. Under certain conditions, the variations in flow velocity, mean pressure, inlet air temperature, equivalence ratio, and vortex structures affect system stabilities. Among these factors, equivalence ratio fluctuations are of particular significance to the occurrence of thermoacoustic instabilities in lean premixed combustors. Pressure oscillations in the combustor perturb the fuel and air flow rates, producing equivalence ratio fluctuations of the mixture. The fluctuating mixture is covected to the flame by the mean flow, causing the heat release rate oscillations which could drive thermoacoustic instabilities. Under lean combustion conditions, the amplitude of heat release rate oscillations produced by equivalence ratio fluctuations increases rapidly with lower mean reaction rate as the equivalence ratio decreases. Equivalently, the lean premixed combustors become more sensitive to equivalence ratio fluctuations as the mean equivalence ratio decreases. Heat release rate oscillations drive instabilities when they are in phase with pressure oscillations. Variations in fuel composition have a significant impact on the flame structure and combustion dynamics, resulting in a change of the phase between oscillations of pressure and heat release rate. Thus, the fuel composition influences the stability of thermoacoustic systems as stated at the beginning of Section 1.1. Although prior experimental investigations qualitatively found the dependence of thermoacoustic instabilities on system parameters and operating conditions, very few experimental data sets are capable of providing reliable correlations that represent the dependence.

Theoretical investigations provided systematic ways of explaining the interactions between different field variables. Due to the complexity of thermoacoustic problems, theoretical studies usually make simplifying assumptions that are not representative of detailed features of thermoacoustic instability phenomenon in real combustion systems. For example, the flame is

often treated as a concentrated heat source with omitted spatial distribution. Such simplifications reduce the fidelity of the prediction of thermoacoustic instabilities, especially for self-excited thermoacoustic instabilities which require a full representation of all processes involved.

Numerical investigations have shown the power to capture the details of the generation and development of thermoacoustic instabilities and the transition to the limit cycle due to nonlinear effects. The responses of various variables to variations in system parameters and boundary conditions can be acquired by perturbing the corresponding parameters and simulating the coupling processes under new conditions. However, there is often a tradeoff between the detailed physics and the computational cost for numerical methods.

Considering both the advantages and limitations, various approaches for investigations are often combined to achieve a balance between the accuracy of results and economy and efficiency of employed methods. For example, Kopitz *et al*. [3] examined the stability of an annular combustor at different operating points by incorporating an experimentally measured flame transfer function (FTF), which describes the linear response of heat release rate to the velocity fluctuations, into a low-order acoustic network model. The complex eigenmodes were determined to simulate the transition to instability. Kopitz and Polifke [4] later proposed a method integrating CFD, low-order acoustic modeling and the Nyquist stability criterion to analyze thermoacoustic instabilities. This method does not require explicit knowledge of the frequency response of the heat source to perturbations in the flow, providing an analysis tool for thermoacoustic systems with complex geometries at modest computational cost. The FTF appeared in the first example can also be determined by an analytical model. Palies *et al*. [5] derived the theoretical transfer functions for premixed swirling flames, based on a perturbed G-equation that represents the flame dynamics. The results were in good agreement with experimentally measured transfer functions for two operating points corresponding to two bulk velocities.

1.2 Concept for solution, scope and objectives

The prior investigations of thermoacoustic instabilities have proposed several mechanisms that are responsible for the onset of thermoacoustic instabilities and the transition to the limit

cycle. The key elements in the feedback loop are identified, and the feedback path is established. However, there is a lack of reliable and effective methods to provide a quantitative description of the influence of a certain system parameter or operating condition on the occurrence and development of thermoacoustic instabilities.

This dissertation proposes an innovative way of evaluating the sensitivities of the driving forces of thermoacoustic instabilities to various influencing parameters, addressing the challenging problem of predicting thermoacoustic instabilities under different operating conditions. The proposed method resolves the physical details of thermoacoustic phenomenon and saves computational efforts.

1.2.1 Concept for solution

The Continuous Sensitivity Equation Method (CSEM) is applied to a CFD framework of thermoacoustic instability problems. The CFD simulations, Rayleigh index calculations and CSEM applications constitute the standard steps of approaching the above concept. The Rayleigh index is a term in the mathematical expression of the Rayleigh criterion statement, and will be introduced in Section 2.2.1. Two classical thermoacoustic instability problems are chosen to demonstrate the concept by following the steps described as below.

1. CFD simulations

A MATLAB code has been developed to model the one-dimensional thermally induced acoustics problem by solving the full set of one-dimensional governing equations. The commercial CFD software ANSYS Fluent 14.0 has been employed to simulate the thermoacoustic instability phenomenon in a self-excited Rijke tube. The Direct Numerical Simulation (DNS) is performed to resolve all the physical details that are representative of interactions occurred in a thermoacoustic system. Given the proper problem definition and appropriate numerical methods, experiences [6, 7] have shown that Fluent is capable of capturing the phenomenon of thermally induced amplification of pressure oscillations and the important coupling processes involved, providing reliable solutions for the field variables, pressure, velocity and temperature that are critical to the sensitivity analysis.

2. Stability criterion

This research chooses the Rayleigh criterion as the reference criterion for thermoacoustic instability and measures the sensitivity of CFD predictions on the thermoacoustic instability by calculating the sensitivity of the Rayleigh index.

3. Sensitivity analysis

The CSEM analysis is performed to investigate the boundary condition effects on the CFD simulation results of thermoacoustic instability problems. Continuous Sensitivity Equations (CSEs) are first derived from the governing equations representative of CFD problems. The formulated sensitivity equations consist of both the unknown sensitivities of field variables and the known values of field variables obtained from Step 1. A solver for the set of CSEs is developed in MATLAB. The sensitivity solver incorporates the reference CFD solution from Step 1, solves the CSEs, and yields the sensitivities of all field variables to a specified parameter, which is a specific boundary condition in this research. The acquired sensitivities of field variables are manipulated to evaluate the sensitivity of a decisive term in the thermoacoustic instability criterion, namely the Rayleigh index, to the specified parameter. The sensitivity of Rayleigh index indicates the tendency of stability of a thermoacoustic system with variations in this specified parameter.

1.2.2 Scope

The thermoacoustic instability phenomenon has been widely investigated using different approaches as discussed in the above sections. Figure 1.2(a) exhibits the different approaches that were used, and the shaded area shows the approach that has been chosen and employed to perform the proposed analysis in Section 1.2.1. The size assigned for each approach does not intend to display the actual popularity of the application to thermoacoustic instability investigations. This research is focused on the sensitivity analysis development based on the CFD simulation of thermoacoustic instabilities.

The implementation of the proposed approach contains five important units, the detailed information of which is shown in Figure 1.2(b), and described as follows:

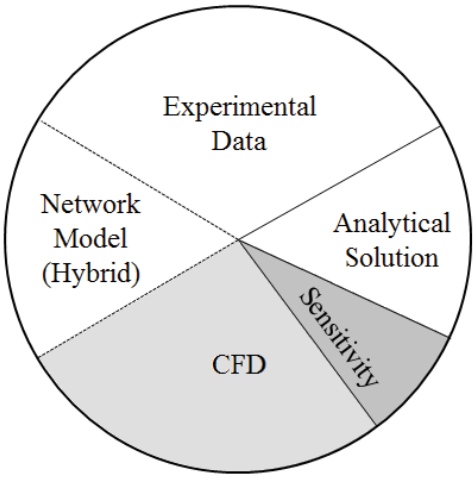

(a)

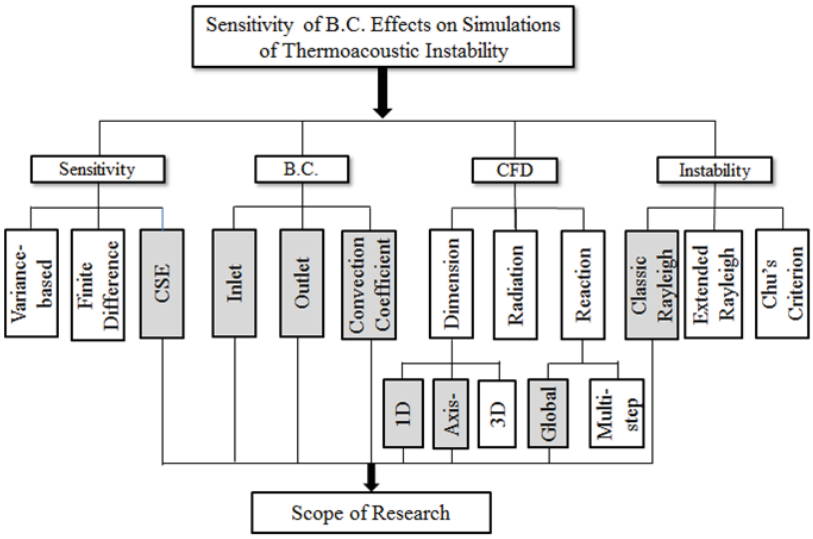

(b)

Figure 1.2: Scope of the research (a) investigation approach (b) detailed implementation.

1. Boundary conditions

With the goal of studying the boundary condition effects on thermoacoustic instabilities, the representation of boundary conditions becomes critical to this work for both CFD simulation and sensitivity computation. Due to limitations in ANSYS Fluent 14.0 for the implementation of acoustic impedance boundary conditions, the inlet boundary of the self-excited Rijke tube model is defined as a mass-flow-rate type which is acoustically closed and the outlet boundary is of a

pressure type, which is acoustically open. The outside wall of Rijke tube is simulated by imposing a constant convection coefficient. The imposed boundary conditions play an important role in numerically stable and physically meaningful simulations. Misrepresentation of the boundary conditions leads to incorrect CFD solutions to field variables that reflect thermoacoustic instability. The deviation of impact of one choice of boundary-condition representation on the field-variable solution from another can be measured by sensitivity analysis, which is the primary work and final goal of this research. Although the boundary conditions defined for the inlet, outlet and walls all have potentials to influence the prediction of thermoacoustic instabilities, investigating all potential factors that affect thermoacoustic instabilities is not indispensable for demonstrating the function of the CSEM applied to thermoacoustic problems. Only the effects of a heated wall boundary are investigated for the one-dimensional thermally induced acoustics problem, and the effects of the inlet mass flow rate and equivalence ratio are explored for the thermoacoustic instabilities in a self-excited Rijke tube. The boundary condition parameters studied in this dissertation are perturbed in magnitude. All the field variable responses to these boundary conditions are obtained and studied to have an understanding of the driving mechanisms of thermoacoustic instabilities.

2. CFD modeling

The simulation of thermoacoustic instability problems is conducted with incremental complexity in physical mechanisms, spatial dimensions and temporal evolution.

The one-dimensional thermally induced acoustics problem is modeled first by solving a system of partial differential equations (PDEs) using a MATLAB code developed specifically for one-dimensional transient compressible flows. The heat source is a heated wall maintained at a constant temperature. To simulate combustion-driven thermoacoustic instabilities, a self-excited Rijke tube with reacting flow is modeled in ANAYS Fluent 14.0. The configuration of this conceptual Rijke tube makes the acoustic wave one dimensional and other physical phenomena primarily axisymmetric, reducing the computational efforts significantly. Solutions for both steady and transient states are obtained. The steady state solution aims at verifying the fundamental physics in the simulation results, while the main focus and efforts are on the transient state simulation, which reproduces the whole process of the thermoacoustic phenomenon observed in experiments. Specifically, the combustion processes are represented by

the global and two-step reaction mechanisms. The impact of different reaction mechanisms on simulation results is demonstrated by comparing and studying the temperature and heat of reaction distributions obtained using the global and two-step mechanisms, respectively. Radiation is also modeled in the CFD simulation to have a more realistic representation of the temperature filed. Three-dimensional problems are not considered in this research, but the proposed approach of applying the CSEM to thermoacoustic instability problems could be easily extended to three-dimensional.

As to the combustion model, it is impossible and unnecessary to replicate the thousands of reactions involved. Instead, the global reaction mechanism and two-step reaction mechanism are applied and compared. Previous computational work [7-9] has shown that these two mechanisms are adequate in modeling the premixed combustion process. Mantel *et al*. [8] showed that both one-step and two-step mechanisms with realistic kinetic parameters were able to predict flame behaviors, which were tested for premixed laminar flames in two different configurations. The test also found that the two-step mechanism provided a better description of the interaction between vortex and flames. Chatterjee [7] successfully used a one-step model to simulate the methane-air reaction in a Rijke tube, with kinetic parameters providing good agreement between experimental and calculated flame speeds. Zambon and Chelliah [9] investigated the interactions between acoustic waves and premixed flames. Their research suggested that the one-step reaction mechanism promoted the pressure amplification, but the optimal two-step mechanism provided similar results to the detailed mechanism.

3. Stability criterion

This dissertation adopts the classic Rayleigh criterion to determine the stability of the thermoacoustic systems. The usual term in Rayleigh criterion is the driving force for the acoustic pressure amplification. Although Nicoud and Poinsot [10] pointed out that the classic Raleigh criterion does not include the important term accounting for acoustic losses, and the Chu criterion based on the conservation equation derived in the form of fluctuation energy is appropriate for thermoacoustic instability problems, little work has been done to check the applicable range and validate the theory by experimental or simulation data. There remains a lot of work to go beyond the Rayleigh criterion.

4. Sensitivity analysis

With the restriction of the long run time for a single CFD simulation case, the traditional sensitivity analysis approaches that are commonly used are impractical for exploring the impact of boundary conditions and modeling parameters on thermoacoustic instabilities. The variance-based sensitivity analysis [11], which computes the sensitivity indices by variances to identify influencing input variables and highlight interactions among variables for calibration and optimization purposes, requires a large number of samples and consequently considerable execution time for CFD simulations. The finite difference method requires fewer samples than the variance-based method. However, the accuracy of computed sensitivity to one influencing parameter using the finite difference method is limited for complicated problems, and additional CFD simulations are required to estimate the effects of other parameters that have potential influence. In contrast to the traditional sensitivity analysis approaches, the CSEM adopted in this dissertation meets the need to save computational efforts by calculating the sensitivity of the thermoacoustic instability criterion to different boundary conditions or modeling parameters from a single CFD result.

Although the role of radiation in reacting flows is taken into account for the CFD simulations, the inclusion of radiation in the sensitivity equations is beyond the scope of the sensitivity analysis in this project which is focused on the fundamental mechanisms.

The impact of reaction mechanism is qualitatively studied by comparing CFD results obtained from the global mechanism and two-step mechanism, respectively. Only the CFD results from the global mechanism are used for the continuous sensitivity analysis. Thus, the CSEs for the Rijke tube problem are formulated based on the global reaction mechanism.

5. Validation

For the one-dimensional thermally induced acoustic problem, the simulation results obtained by a solver written in MATLAB is tested against those presented in a report [12]. The self-excited Rijke tube model is built resembling a laboratorial-scale Rijke tube configuration. However, experimental data are not available for this apparatus. As a result, the experience gained from years of research by other researchers is adopted to provide qualitative evaluation of the simulation results. It should be emphasized that the accuracy of sensitivity calculations depends on the representation of physical problems and the application of specific numerical schemes, but the formulation of sensitivity equations is rigorous and the application of the

CSEM is strictly based on the representation of CFD problems. Thus, this dissertation puts more efforts on the development of the continuous sensitivity analysis, and features of the proposed approach are demonstrated in detail and in depth.

1.2.3 Objectives

The broad objective of this project is to formulate a sensitivity method that can be applied to boundary conditions which affect the prediction of thermoacoustic instability. To achieve this goal, the CFD simulation and continuous sensitivity analysis are performed for one-dimensional and two-dimensional thermoacoustic systems.

Execution procedure of the proposed sensitivity method is demonstrated through the detailed objectives in two main aspects, namely the CFD modeling and sensitivity analysis.

1. CFD modeling

Reliable CFD simulation results of thermoacoustic instability problems are essential to the corresponding sensitivity calculations. This dissertation starts with a one-dimensional non-reacting flow problem with reference data, and extends to the classic Rijke tube with reacting flow that is representative of the primary features of thermoacoustic instabilities occurred in gas turbine engines. Specifically, the CFD simulations include the following two objectives:

1) To develop a CFD model for the thermally induced acoustic problem using MATLAB, with a constant temperature wall temperature defined as the heat source.
2) To develop a CFD model for the self-excited generalized Rijke tube using ANSYS Fluent 14.0, with heat released from a laminar flame in this combustion-driven thermoacoustic device.

2. Sensitivity analysis

The continuous sensitivity analysis is performed for CFD simulations of both one-dimensional and two-dimensional thermoacoustic problems. The standard procedure is as follows.

1) Determine the boundary conditions to be investigated, and develop CSEs based on the governing equations and different boundary condition representations.

2) Use transient CFD simulation results obtained previously as the reference state (compared to the predicted results subject to boundary condition variations) to solve corresponding CSEs in time.
3) Extract the sensitivities of field variables to specified boundary condition changes and compute the sensitivity of the Rayleigh index, which is the indicator of the occurrence of thermoacoustic instabilities.
4) Demonstrate the effects of investigated boundary conditions on the thermoacoustic results, evaluate the application of proposed sensitivity method to thermoacoustic problems, and further discuss the potential value and significant impact of this method on control of operating conditions for thermoacoustic systems and design of equipment that possesses both good efficiency and performance.

1.3 Overview of the dissertation

This dissertation is divided into four main parts. The first part consists of Chapter 1 and 2. Chapter 1 introduces the motivation behind this research, and discusses the status of understanding of mechanisms responsible for the onset of thermoacoustic instabilities and active approaches employed for investigations. Considering the limitations of prior research in exploring the primary parameters impacting thermoacoustic instabilities, an innovative sensitivity analysis approach applied to the CFD framework of thermoacoustic problems is proposed, followed by the scope and objectives of this research. Chapter 2 reviews the literature on the relevant thermoacoustic instability issues supporting the development and validation of the proposed sensitivity analysis approach. The previous applications of CSEM to flow problems are included.

Chapter 3 alone is the second part of this dissertation, and devoted to the development of CSEs based on the general form of governing equations for CFD problems with two types of boundary conditions. Sensitivity of the Rayleigh index is also formulated using sensitivities of field variables.

Applications of the CSEM to thermoacoustic problems are demonstrated in Chapter 4 and 5. Chapter 4 presents the sensitivity calculation of the pressure response to wall-temperature

changes in a compressible fluid bounded by two parallel plates under low gravity. Chapter 5 investigates the boundary condition effects on CFD simulations of thermoacoustic instabilities in a self-excited Rijke tube. Magnitudes of the mass flow rate and equivalence ratio at the inlet boundary are perturbed as influencing factors. Sensitivities of the Rayleigh index to these two influencing factors are computed to predict the tendency of thermoacoustic instability due to the boundary condition changes.

Chapter 6 summarizes the conclusions and perspectives of the present work. Conclusions are drawn from two aspects, i.e. CFD simulation and sensitivity analysis.

Chapter 2

Background on Investigations of Thermoacoustic Instabilities

Since its first discovery more than two centuries ago, there has been extensive work related to thermoacoustic instabilities. A complete list of literature in this field is not practical. This review is dedicated to the work that is relevant to the present research, with a focus on those having the most influence on the establishment and development of this work.

2.1 Origin and history

The first recorded observation of thermoacoustic phenomenon dates back to the "singing flame" by Higgins in 1777 [13], which was created by a jet of hydrogen burning in an open tube. The investigations and explanations of thermoacoustic instabilities in the early age were documented by Tyndal [13] and Rayleigh [14]. Among the devices adopted for thermoacoustic instability studies, the Rijke tube has gained the most favor and most explorations experimentally, analytically and numerically [15-17]. In 1859, the Dutch physicist Pieter Rijke [14] used heat to successfully generate and sustain sound in a vertical tube open at both ends. In his experiments, a wire-gauze was inserted at the distance of a quarter of the tube from the bottom. By heating the gauze to glowing red hot, a loud sound was generated nearly the fundamental node of the tube. The popularity of the Rijke tube in the academic world lies

primarily in that it is convenient and flexible to perform experimental demonstrations without losing the similarity and comparability to instability in the modern thermoacoustic systems used for theoretical studies.

The influence of thermoacoustic instabilities arose in liquid and solid rockets in the late 1930s and early 1940s, in afterburners and ramjets with high-frequency instabilities in the late 1940s and early 1950s and low-frequency instabilities in the late 1970s and 1980s. With the development of lean premixed technology, thermoacoustic instabilities in gas turbine engines began to gain more attention in the 1990s [18]. Efforts have been put into the understanding of the mechanisms of thermoacoustic instabilities and the control guided by mechanisms.

2.2 Mechanisms of thermoacoustic instabilities

2.2.1 Rayleigh criterion

It is well known and experimentally and theoretically proven that thermoacoustic instability is the result of the interaction between the acoustic pressure and heat release rate fluctuations. This hypothesis, first proposed by Lord Rayleigh in 1878 [2] and later named Rayleigh criterion, provided a proper explanation for thermoacoustic instability phenomena and enlightenment for the subsequently deeper and more thorough investigations of thermoacoustic instability mechanisms. It is stated in the Rayleigh criterion that "If heat be periodically communicated to, and abstracted from, a mass of air vibrating in a cylinder bounded by a piston, the effect produced will depend upon the phase of the vibration at which the transfer of heat takes place. If heat be given to the air at the moment of greatest condensation or to be taken from it at the moment of greatest rarefaction, the vibration is encouraged. On the other hand, if heat be given at the moment of greatest rarefaction, or abstracted at the moment of greatest condensation, the vibration is discouraged." This literal description was later written as a mathematical expression by Putnam and Dennis [19] in the following form:

$$\int_{cycle} Hpdt > 0 \ , \tag{2.1}$$

where H denotes the heat release rate and p the oscillating component of the pressure. The oscillations are driven when the inequality is satisfied, or equivalently, when the phase between

the heat release rate and pressure oscillations is less 90°. Chu [20] derived the Rayleigh criterion from the energy point of view and applied his analytical results to two cases with different heat sources. Because the specific heat ratios before and after the heat source were the same, the first case with a plane heater as the heat source yielded a mathematical representation of the Rayleigh criterion in the form proposed by Putnam and Dennis [19]. While the second case with a flame front as the heat source has taken into account the change of specific heat ratios. This slight modification of the classic Rayleigh criterion suggested by Chu is not adopted by this dissertation, which has a focus on demonstration of the proposed sensitivity analysis method applied to thermoacoustic instabilities. Thermoacoustic instability is an overall effect of the heat release and acoustic pressure coupling, which is represented as the integral of the product of fluctuations of pressure and heat release rate over space and time. The most commonly used form is shown as below:

$$\int_0^{\tau}\int_0^{V} p'(\vec{x},t)\dot{Q}'(\vec{x},t)\,dVdt > 0 \quad , \tag{2.2}$$

where p' is the pressure fluctuation, and $\dot{Q}'$ is the heat release rate fluctuation. Both p' and $\dot{Q}'$ vary in space and time. τ denotes the period of oscillations, and V stands for the domain where the coupling effects are considered. The left-hand side of this inequality is called Rayleigh index, and denoted by Ω in this dissertation.

With intensive applications of the Rayleigh criterion, it has been noted by many researchers that the Rayleigh criterion is necessary but not sufficient in predicting the onset of thermoacoustic instabilities. The heat source term has to be greater than the acoustic losses in the system to excite thermoacoustic instabilities, constituting the extended Rayleigh criterion. Nicoud and Poinsot [10] revisited the derivations of the classical acoustic energy equation and fluctuation energy equation that lead to the extended Rayleigh criterion and the Chu criterion respectively, concluding that the entropy fluctuation should also be included for the growth of instabilities. With the main purpose of demonstrating the application of proposed sensitivity analysis method to thermoacoustic instability problems, this dissertation only adopts the classic Rayleigh criterion to predict the occurrence of thermoacoustic instabilities.

2.2.2 Driving mechanisms

There are numerous mechanisms driving oscillations, with several mechanisms identified and still many details to be explored. With two key elements of the Rayleigh criterion in mind, the driving mechanisms either account for fluctuations of pressure or contribute to the fluctuations of heat release rate. Because the mechanisms driving oscillations often occur at the same time, it is challenging to discern the individual mechanism in a certain thermoacoustic system. Some primary mechanisms [21-25] identified in gas turbine engines are listed below. Ducruix *et al*. [24] have proposed a driving or a coupling path for each studied mechanism to link the acoustic variables with heat release fluctuations.

1. Flame-vortex interactions

There are extensive studies on flame-vortex dynamics [26]. The effects of flame-vortex interactions on combustion instabilities are usually attributed to two distinct mechanisms [27-29]. One is associated with vortex roll up, which causes rapid changes in the flame area, consequently perturbing the heat release rate. The other is vortex interaction with walls and other structure, which carries the fresh fuel mixture and induces a sudden increase of heat release rate. Mcmanus *et al*. [21] reviewed this mechanism and summarized that "an important phenomenon involved in this instability mechanism is the time delay between the formation of a coherent vortex structure and the instant that energy is released due to combustion in the vortex. This delay may provide the proper phase relationship between the oscillating pressure field and unsteady heat release to drive the instability".

2. Acoustic-flame coupling

The effects of acoustic waves on the flame have been investigated by several forcing techniques. Disturbances in acoustic pressure cause velocity oscillations, which modulate the flame surface and therefore induce heat release rate fluctuations. Experimental, theoretical and numerical efforts have been put into definitions of transfer functions which relate the unsteady heat release to incident velocity fluctuations. For example, a combination of theoretical analysis and experimental measurements was conducted to determine the transfer function of a laminar premixed flame by Ducruix *et al*. [30], whose work was based on the same assumptions in previous studies by Fleifil *et al*. [31], but advanced by accounting for any operating condition.

3. Interactions of flames with boundaries

The interactions between flames and solid boundaries lead to rapid changes of flame areas, which in turn induce the fluctuations of heat release rate. Durox *et al*. [32] showed this mechanism by systematic experiments where a premixed flame anchored on a burner impinged on a flat plate, producing the source of sound that drove the system due to the modulation of flame areas.

4. Flame response to composition inhomogeneity

Many studies [33-35] have shown that the behavior of combustors is highly sensitive to the equivalence ratio variations under lean premixed combustion conditions. The pressure oscillations interact with fuel and air supply rates, inducing perturbations of equivalence ratio. The formed equivalence ratio perturbations are convected by the flow to the reaction zone, where heat release rate oscillations are produced. The convection time from the formation to consumption of the reactive mixture plays a dominant role in prediction of the occurrence of combustion instabilities. It is pointed out that "instabilities occur when the ratio of this convective time and the period of the oscillations equals a specific constant, whose magnitude depends upon the combustor design [35]."

5. Unsteady strain-rate effects

For premixed flames, the unsteady strain-rate field induced by the resonant acoustic motion acting on the flow influences the heat release oscillations by changing the flame surface area [36].

2.2.3 Damping mechanisms

Recall that the occurrence of combustion instabilities require the net acoustic energy is positive in a combustor, i.e. the energy fed into the acoustic field by the combustion process must exceed the acoustic energy losses through the combustor. A balance between the acoustic energy gained and lost also accounts for the limit cycle phenomenon. Various driving mechanisms have been discussed above, and the primary damping mechanisms are shown as follows [37]:

1. Viscous and thermal dissipation

There are two sub-mechanisms involved. Incident acoustic waves are only partially reflected at the rigid boundary, and a certain amount of acoustic energy is transferred to vortical velocity and entropy fluctuations through viscosity and thermal dissipation effects in the boundary layers respectively. On the other hand, the acoustic energy is converted into vortices when flow separation at sharp edges or rapid flow expansions is present.

2. Convection and radiation of acoustic energy

Acoustic energy leaves the system either by convection of the mean flow or propagation through open ends into the far field.

3. Transfer of energy to different frequencies

Combustion instabilities usually occur with one or more nearly pure tones at specific frequencies. Nonlinear combustion processes transfer acoustic energy from the unstable modes to other unexcited modes, which tends to stabilize the system.

2.3 Influence of inlet flow rate and equivalence ratio

Numerous methods have been used to investigate the mechanisms of thermoacoustic instabilities over the last two decades [38]. This review section makes no attempt to have a complete list of approaches that have been adopted and mechanisms that have been investigated. For lean premixed combustors, the operating conditions, especially the flow rate and the equivalence ratio, have significant influence on the combustion stability behavior subjected to disturbances in the flow. An explanation of the influence is critical for understanding the increased susceptibility to thermoacoustic instabilities observed in lean premixed combustors. Therefore, this dissertation performs the CSEM to study the thermoacoustic responses to the velocity and equivalence ratio boundary changes in a self-excited Rijke tube. Prior investigations of the effects of operating conditions on thermoacoustic instabilities are reviewed, with a focus on the influence of the velocity and equivalence ratio. With excellent literature review work done by other researches before [21, 23, 25], only representative references within last two decades are selected for this review section.

2.3.1 Experimental investigations

Broda *et al*. [39] carried out a comprehensive and systematic experimental investigation of the dependence of combustion instabilities in a premixed gas turbine swirl injector on the equivalence ratio and inlet flow conditions. The ranges of operating conditions under which combustion instabilities occur were determined by a stability map. However, under certain conditions, the transition from an unstable mode to a stable state was not established until the inlet air temperature or equivalence ratio was adjusted significantly below the threshold value for an initially excited unstable state, known as hysteresis effects. It was also found that although the inlet air temperature influenced the onset of combustion instabilities, it did not seem to change the amplitude of induced pressure oscillations, whereas the equivalence ratio had significant effects on the strength of combustion instabilities, with the highest oscillation amplitude identified for equivalence ratio around 0.6. Two Plots showing the two-dimensional Rayleigh index distribution and axial distribution of the integrated Rayleigh index over the cross section were created respectively, confirming a region with strong interactions between acoustic pressure and heat release rate oscillations.

Richards and Janus [40] conducted experimental tests for thermoacoustic instabilities in an experimental combustor representative of lean premixed gas turbines. As suggested by a simple time delay model, the nozzle velocity was found to be the most important determinant under a series of operating conditions tested. Distinguished from other investigations of operating condition effects focusing on the independent impact of each parameter, the authors provided plots of the root-mean-square pressure as a function of nozzle velocity and equivalence ratio. These plots exhibited similar trends with increasing pressure oscillations as the equivalence ratio increased and strongest oscillations occurring at the highest equivalence ratio tested (remained less than 1). It was noteworthy that a few distinct points did not follow the general trend, showing high pressure amplitudes at low equivalence ratios. According to the authors, these exceptions existed near the unstable-combustion-condition boundary where the oscillation amplitude depended on the history of the combustor operation, thus the effects of small disturbances were hard to predict, either stabilizing or destabilizing the combustion processes. The oscillating effect near the transition boundary was also captured by Moeck *et al*. [41] when experimentally exploring the operating range for a turbulent swirl-stabilized premixed flame. A boundary line between the equivalence ratios of 0.55 and 0.60 was determined to represent the

transition phenomenon between an M-type flame structure and a V-type flame structure. A periodic transition between these two types of the flame structure occurred under the operating conditions corresponding to the boundary line.

Through an experimentally parametric study on combustion instabilities in a lean premixed dump combustor, Venkataraman *et al*. [22] found that all the parameters they tested had some influence on combustion instabilities. Among all the tested parameters, the equivalence ratio was varied from the lean limit to stoichiometry under a baseline operating condition. At the velocity of 6 m/s, the combustion became unstable when the equivalence ratio reached approximately 0.55, turned stable again around an equivalence ratio of 0.8, and a stable combustion was reestablished as the equivalence ratio approached stoichiometry. It was stated that the stability of a combustion system could be changed with a small variation in the equivalence ratio by influencing the flame speed and subsequent flame-vortex interactions. The experimental results also showed an increasing susceptibility to combustion instabilities as the inlet velocity increased.

The experimental investigation by Lieuwen [42] was focused on the dependence of the limit cycle characteristics on operating conditions. Over the entire parameter space tested, the maximum pressure amplitude increased monotonically with the increase of the mean inlet velocity, indicating that the inlet velocity plays a significant role in determining the pressure amplitude during the limit cycle. This conclusion supplemented the understanding that the inlet velocity was critical to both the onset and thermoacoustic instabilities and the limit cycle.

An experimental comparison of the sensitivities of combustion instabilities to operating conditions has been made by Bernier *et al*. [43] for both corotative (COS) and counter-rotative (CNS) flow cases in a premixed prevaporized combustor. Different stable combustion domains and transition characteristic between stable and unstable regimes were observed for these two cases. The COS system exhibited instabilities when the velocity was lower than a critical velocity, which increased with the equivalence ratio, while the CNS system became unstable when the velocity was higher than a critical value, which decreased with the equivalence ratio. The transition between stable and unstable regimes occurred in the COS system with an equivalence ratio variation as small as 4%, indicating a higher sensitivity than that in the CNS system.

Yoon *et al*. [44] have conducted experiments to explore the effects of the inlet mixture velocity on combustion instabilities in a model gas turbine combustor. Instabilities were discover not only at high velocity conditions due to the in-phase interactions between pressure and heat release rate fluctuations, but also at low velocity conditions resulting from the vortex structures.

Experimental investigations give some insights into the mechanisms of thermoacoustic instabilities, and provide a reference for the identification of influential factors and the qualitative evaluation of the effects of operating conditions on thermoacoustic instabilities. However, the information obtained from experiments is limited due to the difficulties in measurements and the considerably large labor required. The dependence of acoustics on the geometry of the system makes it apparent that the thermoacoustic instability phenomenon may vary from one system to another. The onset of thermoacoustic instabilities is not predictable for a particular system without actually running it. Thus, theoretical and numerical investigations play an important role in the prediction of the thermoacoustic instabilities and the design of systems to reduce or eliminate the destruction caused by thermoacoustic instabilities.

2.3.2 Theoretical and numerical investigations

This section discusses the theoretical and numerical approaches commonly used in investigations of the thermoacoustic instability phenomenon. This discussion is mainly for the purposes of selecting an appropriate computational frame for the continuous sensitivity analysis and evaluating the proposed sensitivity analysis method.

The fundamental physics of thermoacoustic instability phenomenon are represented by Navier-Stokes (NS) equations. There are primarily three approaches to implement the NS equations [45].

1. The linearized Rankine-Hugoniot equations, obtained from the conservation equations of mass, momentum and energy by considering a compact heat source, are expanded around a small Mach number to relate the heat release perturbations to fluctuations of the pressure and velocity upstream and downstream of the heat source. The use of network models with a describing function for the influence of acoustic waves on heat release fluctuations produces a dispersion equation to be solved for the eigenfrequencies [46, 47].
2. An inhomogeneous wave equation is derived by simplifying the linearized N-S equations and solved by the Galerkin method [48-50].

3. CFD simulations are widely employed, and particularly the DNS and the Large Eddy Simulation (LES) are applied to most thermoacoustic instability problems. The CFD simulation is directly related to the computational work in this dissertation and will be discussed in the following sections.

Both the linearized Rankine-Hugoniot equations and the inhomogeneous PDEs require a closure formulation for the heat release term to be solved. The time-delay model, also referred as the n-τ model, provides such a closure formulation and has been used in theoretical investigations of the mechanisms of thermoacoustic instabilities [35, 47]. In a time-delay model, the interaction index n describes the sensitivity of heat release rate to pressure oscillations, and the time delay τ represents the time interval between the instances when the pressure fluctuations occur at the heat source and when heat release fluctuations take place. In premixed combustion models, the time interval for reactants to convect from the injection point to the flame region is essential for the occurrence of thermoacoustic instabilities. A mean convection time was proposed by Putnam [51] to estimate the time lag, the expression of which is given as:

$$\tau = \frac{\delta}{V_p} \ , \tag{2.3}$$

where δ is the distance between the fuel injector to the flame front and V_p is the mean fuel velocity. Evidently, this τ represents a mean convection time between the fuel injector and the flame front.

The significance of reviewing the time-delay model for the present research lies in the dependence of the time lag, a characteristic parameter for thermoacoustic instabilities, on operating conditions, such as the inlet velocity impacting the convection velocity for the convection time, and the equivalence ratio associated with the chemical time.

Recall the experimental investigations conducted by Bernier *et al*. [43], they also performed a simple time-delay analysis accounting for both the convection time and the chemical time which was essentially a function of the equivalence ratio and injection temperature, with a purpose of proposing a consistent framework for the experimental observations in the two swirl configurations.

Lieuwen *et al*. [33] developed an unsteady well stirred reactor (WSR) model to study the premixed combustion responses to the temperature, flow rate and equivalence ratio fluctuations.

This theoretical model showed that as the mean equivalence ratio decreased, the flow rate and temperature fluctuations exert little impact on heat release oscillations, whereas the equivalence ratio fluctuations caused a tremendous increase in heat release oscillations. The increased heat release rate oscillations were attributed to the facts that large variations in the chemical time were produced by the equivalence ratio perturbations at lean operating conditions and that the magnitude of the reaction rate was inversely proportional to the chemical time.

2.3.3 CFD investigations

CFD modeling is a powerful tool for studying the complicated fluid problems. It is particularly attractive for investigating thermoacoustic instabilities because of the capability of capturing all relevant processes involved in the complex phenomenon. By the same token, the drawback of the requirement of extensive time and computational sources for this approach is also obvious, especially for a parametric study on the effects of boundary conditions and modeling factors on simulations of thermoacoustic instabilities. The complex flow field with the transport of multiple species and rapid combustion makes the CFD simulation for thermoacoustic problems extremely challenging.

2.3.3.1 Simulation methods

LES and DNS are two commonly adopted simulation approaches for thermoacoustic instability problems. LES has been used successfully in the prediction of thermoacoustic instabilities in various combustion systems [52-55]. List here are only a few selected references on the LES investigation for thermoacoustic instabilities. Since the flow present in the self-excited Rijke tube studied is laminar, and the sensitivity analysis based on CFD simulation results requires a time-accurate representation of all physical details, DNS is chosen for simulations of the thermoacoustic instability in this dissertation. The previous experiences [56-59] in applying DNS to the investigation of thermoacoustic instabilities have provided strategies and conclusions for reference in the present research. Laverdant and Thevenin [57] studied the interaction between a turbulent premixed flame and a Gaussian acoustic wave using the DNS, the results of which identified the location where the wave amplification occurred and agreed with the implication of Rayleigh criterion. The same research group [58] performed DNS for a syngas flame interacting with a realistic acoustic wave. They found that species CO_2, H and H_2O

were mainly responsible for the wave amplification, while species O, OH and CO dominated damping. A parametric study using DNS was conducted by Talei *et al*. [59] for sound generation by premixed laminar flame annihilation. Simulation results showed that the sound generation was significantly influenced by Lewis number, laminar flame speed, temperature ratio and Zel'dovich number.

To overcome the drawback of the huge demand in computational time and memory and make use of the advantage of resolving detailed physics, the CFD simulations are often incorporated with other methods with a main responsibility of determining the flame transfer function or a describing function for nonlinear interactions [47, 60-62]. Several examples of the hybrid method have been provided in Section 1.1.2.

2.3.3.2 Boundary conditions

Boundary conditions are critical for CFD simulations. Misrepresentation of boundary conditions leads to inaccurate or unrealistic solutions, even no solutions at all. In addition, the physical boundary conditions in CFD simulations of thermoacoustic problems correspond to the in-service operating conditions in thermoacoustic systems. Small disturbances may excite large acoustic pressure simulations, so it is of crucial importance to understand how sensitive the response of thermoacoustic instabilities is to variations in boundary conditions, so that guidance can be provided on the control of operating conditions to suppress thermoacoustic instabilities.

1. Implementation of boundary conditions

The technical difficulty in imposing boundary conditions for thermoacoustic instability problems lies in the enforcement of appropriate acoustic boundary conditions in addition to the typical flow boundary conditions. The commonly used boundary conditions can produce spurious numerical instabilities in addition to physical instabilities. It is critical to suppress the unrealistic reflections of pressure waves at the boundaries, particularly when deriving the FTF for combustion instabilities with the emphasis on the effects of acoustic waves passing through the heat source. The implementation of non-reflecting boundary conditions allows the acoustic waves to leave the domain, diminishing the coupling effects for determination of the transfer functions. Poinsot and Lele [63] developed the Navier-Stokes Characteristic Boundary Conditions (NSCBC) method to implement of both the physical and numerical boundary

conditions for compressible viscous flows. This approach has been frequently adopted, and extended and modified later by other researchers [64-66]. Baum *et al*. [64] incorporated the realistic thermodynamic properties that depend on the temperature and mixture composition. Realizing that the treatment of non-reflecting boundary conditions suggested by Rudy and Strikwerda [67] and employed by Poinsot and Lele [63] actually yielded partially reflecting boundary conditions, Selle *et al*. [65] proposed a scaling technique to adjust the relaxation coefficient used in the original treatment. Polifke *et al*. [66] modified the NSCBC method with "wave masking" to produce fully non-reflecting boundary conditions at low frequencies. Martin *et al*. [68] investigated the effects of outlet boundary conditions by changing the outlet impedance from the non-reflecting condition with a stable flame to a reflecting boundary, and switching back to a non-reflecting condition at a later time. During these operations, the flame became unstable with a reflecting boundary and was stabilized again due to the change to a non-reflecting boundary condition.

Accurate boundary conditions can also significantly reduce the computational efforts, by making it possible to model only part of the full geometry. The considerable cost of computing sources and computational time has restricted the use of CFD simulations for fully parametric exploration of thermoacoustic instabilities in gas turbine engines [69-71]. With representative boundary conditions, the computational domain could be reduced accordingly, instead of modeling the entire gas turbine system. Since the boundary conditions for acoustic variables are generally defined by impedance in the frequency-dependent complex form, while CFD methods are applied in the time domain, the time-domain acoustic boundary conditions need to be properly imposed for CFD simulations. Schuermans *et al*. [69] developed state-space representations for the impedance boundary conditions that were well-suited in the CFD computation, the results of which showed good agreement with experimental measurements for the thermoacoustic behavior in a gas turbine combustion system. Huber *et al*. [70] accurately represented the acoustic boundary conditions by a discrete filter model that was transferred to the time-domain formulation using the z-transformation. Although the present research investigates only the effects of inlet boundary conditions on the CFD simulations of thermoacoustic instabilities, the representations of the outlet impedance boundary condition proposed by other researchers provide good reference for future work on the outlet boundary condition effects and

the possibility of thorough parametric studies on thermoacoustic instability problems by reducing the computational domain.

2. Boundary condition effects

Both the physical and numerical boundary conditions impact the simulation results significantly. As the objective of the present research is to investigate the effects of boundary conditions, representative of in-service operating conditions for realistic gas turbine engines, on thermoacoustic instability phenomena, computational investigations of the thermoacoustic responses to perturbations in physical boundary conditions are reviewed. Kaufmann *et al*. [72] tested two forcing techniques for combustion instability simulations, i.e. inlet velocity modulation (IVM) and inlet wave modulation (IWM). Results from both analytical and numerical test cases have shown that IVM led to resonance phenomena preventing the prediction of FTF, while using IWM, for which only the incoming acoustic wave was perturbed, resulted in accurate prediction of FTF. The effects of different forcing techniques further confirmed that boundary conditions play a critical role in thermoacoustic instability simulations. Duchaine *et al*. [73] studied the effects of five parameters on determination of the FTF for laminar premixed flames. The flame speed and the inlet duct temperature were identified to have influence on the flame delay, subsequently impacting the computation of transfer functions. In order to investigate the effects of equivalence ratio fluctuations on flame dynamics, Hermeth *et al*. [74] performed LES for a burner under "technically" premixed mode and fully premixed mode, respectively. They have shown that the mixing fluctuations induced in the "technically" premixed case affected the FTF delay, which was 1.5 times larger than the fully premixed case, and the interactive index was slightly smaller.

2.4 Sensitivity analysis

Sensitivity analysis is a tool to evaluate how the inputs affect the outputs in a system, the details of which may include how the input uncertainty propagates, how the addition of a new input affects the output, and how the output variation is apportioned among the inputs [75]. For the present research, the objective of sensitivity analysis is to evaluate the thermoacoustic response to boundary condition changes in CFD simulations. There are a variety of sensitivity

analysis methods which are potential candidates to be used for exploring thermoacoustic instability problems. Generally, these sensitivity methods can be classified as local sensitivity and global sensitivity techniques. Although the local sensitivity approach appeared earlier than the development of the global sensitivity approach, it is discussed in this section following the brief introduction of global sensitivity analysis due to its importance to the present research.

2.4.1 Global sensitivity analysis

Global sensitivity analysis provides insights into the model outputs subject to a full range of variations in the inputs, and does not distinguish the initial state of inputs. The features of global sensitivity analysis determine its advantages of taking into account the interactions among variables so as to find combinations that can result in specified values for the model output, in addition to the abilities of identifying uninfluential variables for model reduction purposes and influential variables for calibration or optimization tasks.

One example of global sensitivity analysis is the variance-based method, which allows the computation of variances, referred to as the sensitivity indices, for estimating the effects of inputs on the outcomes. Variance-based methods undoubtedly have the advantages described above, but as a class of probabilistic approaches, they obviously necessitate a considerable number of simulation runs, from hundreds to thousands. For complicated problems like thermoacoustic instabilities, the model requires simplification in dimension, computational domain or physical processes so that the number of simulations performed becomes sufficient for global sensitivity analysis. However, the current investigations of thermoacoustic instability problems aim to understand the sophisticated mechanisms involved in the physical processes, and thus require resolutions for the disparate length and time scales, consequently making the problems demanding in computational sources and time. Therefore, it is not feasible to apply global sensitivity analysis for thermoacoustic problems.

2.4.2 Local sensitivity analysis

In contrast to the global sensitivity which measures the output responses to the entire domain of input variables, local sensitivity analysis concerns the degree of change of the output as the

input varies in the neighborhood of a reference value. The measure for local sensitivities is the derivative. Two derivative-based methods are introduced in this section.

1. Finite difference approximation

The derivative can be expressed numerically by the rate of change of the output variable under two conditions with closely defined values of an input variable. One-at-a-time technique can be used to perturb the inputs. Although the number of runs for modeling is reduced largely compared to global sensitivity methods, the finite difference approximation, as a traditional local sensitivity method, still requires at least N+1 simulation runs, where N is the number of potentially influential parameters to be tested and 1 stands for the set of reference values, not to mention additional solutions needed for a complex nonlinear problem like thermoacoustic instability.

2. Sensitivity Equation Method

A promising alternative procedure to evaluate the derive-based sensitivities is the application of Sensitivity Equation Method (SEM). In this method the sensitivities are extracted by solving sensitivity equations, which are obtained by differentiating the original PDEs and boundary conditions with respect to specified parameters, namely the CSEM employed in this dissertation, or by differentiating the discrete governing equations, belonging to the discrete SEM.

2.4.3 Applications

2.4.3.1 Sensitivity analysis of relevant problems

The systematic application of sensitivity analysis is more active in the area of solid mechanics than in fluid dynamics. Although it is known that sensitivity analysis is an effective tool in terms of assisting in modeling to gain insights into a variety of practical problems, the complexity in thermoacoustic problems has limited the use of many sensitivity analysis approaches. This section attempts to review research work on sensitivity analysis of thermoacoustic and related problems employing different sensitivity methods, excluding most references performing sensitivity analysis by running cases and comparing results under different conditions without sensitivity calculations.

Rabitz *et al*. [76] gave a thorough review on the status of sensitivity analysis in chemical kinetics in early 1980s. The applications of some local sensitivity techniques including finite differences, direct differential methods and adjoint methods, and global sensitivity methods were discussed. An important perspective of this review was the fact that the sensitivity tools used for chemical kinetics are generally applicable to a wide range of problems that can be described by mathematical models.

Giovangigli and Smooke [77] employed continuation methods to study the effects of the equivalence ratio on the peak temperature and the adiabatic flame speed for premixed laminar flames. The resultant response curves contained the lean and rich flammability limits which were shown to be influenced by the size of computational domain.

As mentioned in the section of CFD simulations, Duchaine *et al*. [73] performed DNS to investigate the sensitivity of the FTF to five parameters in a one-at-a-time fashion. Their analysis results revealed that the FTF delay was mainly controlled by the flame speed and the inlet duct temperature.

Recent work done by Magri and Juniper [78, 79] innovatively applied the adjoint-based sensitivity method to two thermoacoustic systems: a Rijke tube with a hot wire [78] and a thermoacoustic system containing a diffusion flame coupled with duct acoustics [79]. Both the structural and the base-state sensitivities were computed for the thermoacoustic systems, which were tested against finite difference calculations and showed perfect agreement when using the discrete adjoint method. The adjoint-based methods exhibited the capability of computing the sensitivity of a response function with respect to a large number of input parameters with a single calculation. In terms of the efficiency in computations of sensitivities, the adjoint-based method is comparable with the CSEM employed in this dissertation, with each having its advantage over the other for different problems. As put by the authors, the novelty of this work lies in the sensitivity analysis techniques it presented, and there remain technical challenges. A few more facts about their work were that the heat release term was modeled by the time-delay approach instead of an accurate model, and the sensitivity was computed for the linear growth phase.

2.4.3.2 Applications of SEM

To the best of the author's knowledge, the present research is the first to apply the CSEM to thermoacoustic problems. Prior applications of SEM to various problems are reviewed to demonstrate the applicability of this method to thermoacoustic systems.

Lutz *et al*. [80] performed sensitivity analysis for a homogeneous reacting gas mixture to predict the kinetic responses with respect to the individual reaction rate. They employed the same software to solve both the nonlinear ordinary differential equations representing the temperature and species mass fractions and the corresponding linear sensitivity equations. Aung *et al*. [80] adopted the same method and identified the reaction that exhibited the largest sensitivities, indicating the significant role the identified reaction played in determining the flame speed.

Borggaard *et al*. [81-86] at Virginia Tech are pioneers in the application of the SEM to optimal aerodynamic design and prediction and uncertainty analysis of flow simulations. Efficient schemes and solvers were developed, and the advantages of CSEM were manifested in their research. With most of the prior work using steady-state flow problems for demonstration of the CSEM, Hristova *et al*. [84] performed continuous sensitivity analysis for transient incompressible laminar flows. The pulsed flow around a square cylinder leading to the famous Karman vortex street was simulated and further studied by uncertainty analysis and fast evaluation of nearby flows via CSEM. The powerful function of CSEM was proven by the sensitivity results that successfully predicted the flow transition from the symmetric vortex pattern to the vortex street. Turgeon *et al*. [85] studied the effects of modeling parameters in the k-e model on the simulation of turbulent flows, through which a variety of applications of the sensitivity analysis were shown. Godfrey *et al*. [82] contributed in the use of sensitivity equations for Chemically Reacting Flows. Sensitivities to the equivalence ratio and the injectant velocity were calculated by solving the linear sensitivity equations, the computational cost of which was generally less than 10% of the full nonlinear solver for governing equations of fluid dynamics.

The ability of CSEM to predict the occurrence of flow instabilities was also demonstrated by computing the sensitivities with respect to flow parameters for thermally induced instability problems by Giguère *et al*. [87]. The computed sensitivities not only successfully captured the transition between stable and unstable flow regimes, but also provided correct guidance on the control of flow instabilities.

Although there has been no attempt to apply the SEM to thermoacoustic instability problems, all the prior studies on sensitivity analysis and optimal design using the SEM suggest the promising application of the SEM to thermoacoustic instability problems. The advantages of the SEM presented previously still hold for the thermoacoustic instability problems. Particularly, the considerably computational saving of SEM makes the parametric investigation of thermoacoustic responses using detailed nonlinear model feasible. As an efficient solution to the CSEs, the automatic differentiation [83] is recommended for complex problems due to the tedious process of constructing all the required derivatives of sensitivity equations by hand. However, for the present research, the source code utilized by the automatic differentiation software is not available from ANSYS Fluent 14.0. A solver for the CSEs of thermoacoustic instability problems must be developed.

Chapter 3

Methodology

3.1 CFD simulation

CFD simulation is conducted to obtain a reference solution to the thermoacoustic problem. The solution is then incorporated into the CSEs. The standard procedure to perform CFD simulation consists of geometric modeling, mesh modeling, physical modeling including governing equations and boundary conditions, discretization and solution, and verification and validation. In this research, two thermoacoustic problems are addressed following the procedure. This chapter describes a systematic way of investigating the sensitivity of thermoacoustic responses to boundary condition variations with general expressions of both governing equations and sensitivity equations. The details of execution specific to the studied problems are presented in the subsequent chapters.

3.1.1 Fundamental physics

Although different fluid problems involve different physical processes, the fundamental principle is readily established. Using the notation in ANSYS Fluent Documentation as reference, this dissertation adopts the conservative form of governing equations:

1. Conservation of mass:

$$\frac{\partial \rho}{\partial t} + \nabla \cdot (\rho \vec{u}) = 0 \ , \tag{3.1}$$

where ρ is the density of flow, and $\vec{u}$ is the flow velocity.

2. Species transport equation:

$$\frac{\partial}{\partial t}\left(\rho Y_k\right) + \nabla \cdot \left(\rho \vec{u} Y_k\right) = -\nabla \cdot \vec{J}_k + \dot{w}_k + S_k \ , \tag{3.2}$$

where Y_k is the mass fraction of species k in the mixture, $\dot{w}_k$ is the net rate of production of species k by chemical reaction, and S_i is the rate of creation of species k by addition of sources. $\vec{J}_k$ stands for the diffusion flux which results from the concentration and temperature gradients. For laminar flows, $\vec{J}_k$ has the following form by neglecting the Soret effect which accounts for the mass diffusion due to temperature gradients:

$$\vec{J}_k = -\rho D_{k,m} \nabla Y_k \tag{3.3}$$

where $D_{k,m}$ is the equivalent mass diffusion coefficient of species k into the mixture. For multispecies diffusion, $D_{k,m}$ can be detrmined by specifying the binary mass diffusion coefficient $\mathcal{D}_{jk}$ which can be either defined as a constant or represented as a temperature-dependent function. Let N denote the total number of species involved in the transport and combustion processes. Because the mass fractions for all the N species should add up to unity, the numerical error can be reduced by employing N-1 species transport equations and one equation using the unity property for the species that accounts for the most mass of the mixture. This method is often adopted for the dilute mixture. Lean premixed methane and air mixture presented in this research satisfies the dilute approximation and N_2 is the species with the largest mass fraction.

3. Conservation of momentum:

$$\frac{\partial}{\partial t}\left(\rho \vec{u}\right) + \nabla \cdot \left(\rho \vec{u}\vec{u}\right) = -\nabla p + \nabla \cdot \bar{\bar{\tau}} + \rho \vec{g} + \vec{F} \ , \tag{3.4}$$

where $\bar{\bar{\tau}}$ is the stress tensor defined as follows:

$$\bar{\bar{\tau}} = \mu \left[\left(\nabla \vec{u} + \nabla \vec{u}^T \right) - \frac{2}{3} \nabla \cdot \vec{u} I \right] . \tag{3.5}$$

The last two terms on the right side of Equation 3.4 denote the gravitational body force and external body forces, respectively. μ in Equation 3.5 is the viscosity of the fluid, which can be

assumed to be a constant as in Chapter 4 for the one-dimensional thermally induced acoustic problem or expressed as a composition-dependent function as in Chapter 5 for the self-excited Rijke tube problem.

4. Conservation of energy:

The following form is used to represent the energy equation:

$$\frac{\partial}{\partial t}\left(\rho E\right)+\nabla\cdot\left(\vec{u}\left(\rho E+p\right)\right)=\nabla\cdot\left(\lambda_{eff}\nabla T-\sum_{i}h_{s,k}\vec{J}_{k}+\left(\overline{\overline{\tau}}_{eff}\cdot\vec{u}\right)\right)+\dot{w}_{T}+S_{h}+S_{\vec{F}}\ , \tag{3.6}$$

where the total non-chemical energy E is the sum of sensible and kinetic energies:

$$E=h_{s}-\frac{p}{\rho}+\frac{u^{2}}{2}\ . \tag{3.7}$$

The sensible enthalpy h_s is calculated as $h_s=\sum_k Y_k h_{s,k}$ for ideal gases, and $h_{s,k}=\int_{T_{ref}}^{T}c_{p,k}dT$ represents the sensible enthalpy of species k. $c_{p,k}$ is the specific heat at constant pressure for species k and the reference temperature T_{ref} is 298.15K. λ_{eff} and $\overline{\overline{\tau}}_{eff}$ denote effective conductivity and stress tensor, respectively, and the corresponding terms stand for energy transfer due to conduction and viscous dissipation. The heat released by chemical reaction is denoted by $\dot{w}_T$ and computed as

$$\dot{w}_{T}=-\sum_{k}h_{f,k}^{o}\dot{w}_{k}\ , \tag{3.8}$$

where $h_{f,k}^{o}$ is the mass enthalpy of formation of species k, and $\dot{w}_k$ is the volumetric rate of reaction shown in Equation 3.2. The source term S_h includes volumetric heat sources except heat of reaction, such as heat due to radiation. The last term in the energy equation, $S_{\vec{F}}$, is the power produced by the volume forces, and neglected in this research.

For the present studies of low-Mach number flows, the energy equation is converted into an equation for temperature:

$$c_{p}\frac{\partial}{\partial t}\left(\rho T\right)+c_{p}\nabla\cdot\left(\rho\vec{u}T\right)=\frac{Dp}{Dt}+\nabla\cdot\left(\lambda_{eff}\nabla T\right)-\left(\sum_{k}c_{p,k}\vec{J}_{k}\right)\cdot\nabla T+\overline{\overline{\tau}}_{eff}:\nabla\vec{u}+\dot{w}_{T,c_{p}}+S_{h}+S_{\vec{F}}\ . \tag{3.9}$$

The total derivative of pressure appeared on the right hand side is defined as

$$\frac{Dp}{Dt} = \frac{\partial p}{\partial t} + \vec{u} \cdot \nabla p \quad . \tag{3.10}$$

It should be noted that the heat source by chemical reaction $\dot{w}_{T,c_p}$ is different from $\dot{w}_T$ shown in Equation 3.6 by a small amount associated with the sensible enthalpy change:

$$\dot{w}_{T,c_p} = -\sum_k h_k \dot{w}_k = -\sum_k h_{s,k} \dot{w}_k - \sum_k h_{f,k}^o \dot{w}_k \quad , \tag{3.11}$$

where h_k is the absolute enthalpy of species k.

The equation for temperature can also be expressed in terms of the specific heat at constant volume, c_V :

$$\begin{aligned} c_V \frac{\partial}{\partial t}(\rho T) + c_V \nabla \cdot (\rho \vec{u} T) &= \nabla \cdot (\lambda_{eff} \nabla T) - RT \nabla \cdot \left(\sum_k \vec{J}_k / W_k \right) - \left(\sum_k c_{p,k} \vec{J}_k \right) \cdot \nabla T \\ &+ \overline{\overline{\sigma}}_{eff} : \nabla \vec{u} + \dot{w}_{T,c_V} + S_h + S_{\vec{F}} \end{aligned} \quad , \tag{3.12}$$

where the specific gas constant R is given by $R = Ru / W$. $Ru \approx 8.31 J / (mol \cdot K)$ is the universal gas constant. The molecular weight of the mixture W is computed using the molecular weight and mass fraction of species k as

$$W = \frac{1}{\sum_k \frac{Y_k}{W_k}} \quad . \tag{3.13}$$

The heat release by chemical reaction in Equation 3.12 differs from those in Equation 3.6 and 3.9, and is denoted by $\dot{w}_{T,c_V}$ and determined by

$$\dot{w}_{T,c_V} = -\sum_k e_k \dot{w}_k \quad , \tag{3.14}$$

where e_k is the sensible and chemical energy of species k.

5. Equation of state:

For compressible flow, the ideal gas law is often used, which relates the pressure p with density ρ and temperature T:

$$p = \rho R T \quad . \tag{3.15}$$

3.1.2 Boundary conditions

The Dirichlet and Neumann types of boundary conditions are used in both physical boundaries and numerical boundaries.

For a variable Q, the Dirichlet boundary condition is defined as

$$Q(\vec{x},t) = f(\vec{x},t) \qquad \text{on } \Gamma_D \ , \tag{3.16a}$$

and the Neumann boundary condition is defined as

$$\frac{\partial Q}{\partial \vec{n}}(\vec{x},t) = g(\vec{x},t) \qquad \text{on } \Gamma_N \ . \tag{3.16b}$$

where Γ_D and Γ_N denote the corresponding boundaries and $\vec{n}$ is the normal to boundary Γ_N.

3.1.3 Discretization

Finite Difference Method (FDM), Finite Element Method (FEM) and Finite Volume Method (FVM) are the common discretization methods, and all of them have been employed for thermoacoustic problems. For the study presented in this dissertation, the FDM and FVM are chosen to discretize the continuous governing equations. The FDM has been an important numerical method to approximate the differential equations by difference equations. The governing equations for thermally induced acoustics presented in Chapter 4 are discretized by the FDM. The self-excited thermoacoustic instability problem in Chapter 5 employs the FVM, which has been widely used in CFD, with the feature that the governing equations are approximated over control volumes, consequently the fluxes are conserved through control volumes.

3.1.4 Key issues

The introduction and background of thermoacoustic instability have shown the complexity of this phenomenon and the difficulties encountered in the investigation processes associated with it. In CFD investigations, the following key issues need to be taken care of and addressed properly:

1. Boundary conditions

As a key element of this research, the significance of boundary conditions in the context of thermoacoustic instabilities has been discussed comprehensively in Section 2.3.3.2.

2. Nonlinear effects

In a real thermoacoustic system, the amplitude of pressure oscillations does not grow infinitely. Under the non-linear effects, the amplitude eventually saturates and remains constant, reaching the limit cycle. The CFD simulation in this dissertation is responsible for capturing the dominant processes occurring in thermoacoustic systems, accounting for the nonlinear effects associated with the loss of acoustic energy. The computational cost increases considerably with the addition of these mechanisms to model, but reliable CFD solutions constitute the basis for a meaningful sensitivity analysis.

6. Length and time scales

The phenomenon of thermoacoustic instability involves a number of fluid, combustion and acoustic related physical processes, each with disparate length and time scales. The length scales pertain to both the physics and geometry. For example, the Rijke tube widely used in laboratories typically has a large length to diameter ratio (aspect ratio), the heat source region is compact compared to the volume of tube, and the acoustic wave length is much larger than the present fluid dynamic length scales. Thickness of boundary layers and eddy sizes also need to be taken into account. Besides the diverse length scales, different time scales exist in different processes of this phenomenon. Three characteristic time scales are often used to describe and analyze the coupling between acoustics and chemical reaction, acoustic time scale, diffusion time scale, and chemical time scale. The characteristic physical time scales (diffusion scale, turbulence scale, etc.) are relatively large, ranging from 10^{-3} to 1s. The finite rate chemical time scales are close to the acoustic time scales in the range from 10^{-4} to 10^{-1}s, while the fast chemical reactions have characteristic time scales from 10^{-9} to 10^{-5}s. The wide range of length and time scales requires special care and treatment to the mesh and the time step size.

7. Numerical noise

In general, the acoustic energy takes up only a very small part of the total energy in the flow field. Depending on the representation of boundary conditions and the implementation of specific numerical schemes, the numerical noise could be significantly larger than the acoustic fluctuations. Well-established numerical techniques are desirable to minimize the numerical

noise. Sufficient computational time is necessary to separate the signal from the initial numerical disturbances.

8. Post-processing

The direct results of CFD simulations of thermoacoustic instabilities are data showing the fluctuations of field variables and the amplification of acoustic pressure oscillations. To gain some insight into the mechanisms of thermoacoustic instabilities, post-processing is needed to interpret the results. The present study performs sensitivity analysis of the Rayleigh index to investigate the influence of boundary condition variations on the instability of thermoacoustic systems.

3.2 Sensitivity analysis

CFD problems in low dimensions with simple geometry and physics usually require relatively low computational effort. For these problems, it is feasible to obtain sufficient simulation data in a short time period to verify and validate problem representation and the numerical approach used, and study the problem by comparing different cases. In these cases, sensitivity analysis can be performed in a simple procedure: perturb the interested parameters, run corresponding simulation cases, and apply the finite difference method or variance-based sensitivity methods that require tens to hundreds, even thousands of simulation runs. Thermoacoustic instability problems usually involve reacting flow and have disparate length and time scales. Thus, the CFD simulation of thermoacoustic problems consumes considerable computational time and resources. The finite difference method and variance-based sensitivity methods are not practical anymore. In these problems, the CSEM makes it possible to investigate the effects of boundary condition changes on stability of a Rijke tube and other combustion systems with a single simulation.

The CSEM uses CFD simulation results from a single run to compute the sensitivities to boundary-condition parameters of interest, which not only reduces the computational time significantly compared to other sensitivity analysis methods, but also extracts sensitivities of all field variables to some parameter at one time. Manipulating these sensitivities of field variables

yields sensitivities of other dependent variables, such as the indicator of thermoacoustic instabilities, the Rayleigh index.

3.2.1 Derivation of CSEs

The CSEs are derived by implicitly differentiating the flow governing equations. Suppose a field variable Q, such as the pressure p, velocity u and temperature T in the thermoacoustic instability problems, could be modified by the parameter a, such as the inlet velocity u_{in} or equivalence ratio ϕ, the sensitivity of the field variable Q, with respect to the parameter a is defined as the partial derivative of the field variable with respect to the parameter a, denoted by s_Q^a. For instance, the sensitivity of pressure to the equivalence ratio is denoted by s_p^ϕ, where the influential parameter $a = \phi$. The parameter a can be any factor that may have influence on the flow fields, ranging from flow properties, to modeling and shape (geometric) parameters. The focus of this research is on the wall temperature effect for a thermally induced acoustic problem and effects of the inlet mass flow rate and the equivalence ratio for a self-excited thermoacoustic instability problem, while the modeling and shape sensitivities are not considered here.

Taking the partial derivatives of the governing equations (Equations 3.1-3.2, 3.4, 3.6 or 3.9 or 3.12, and 3.15) with respect to the parameter a yields:

$$\frac{\partial}{\partial a}\frac{\partial \rho}{\partial t} + \frac{\partial}{\partial a}\nabla\cdot(\rho\vec{u}) = 0 \tag{3.17}$$

$$\frac{\partial}{\partial a}\frac{\partial}{\partial t}\left(\rho Y_k\right) + \frac{\partial}{\partial a}\nabla\cdot\left(\rho\vec{u}Y_k\right) = -\frac{\partial}{\partial a}\nabla\cdot\vec{J}_k + \frac{\partial \dot{w}_k}{\partial a} + \frac{\partial S_k}{\partial a} \tag{3.18}$$

$$\frac{\partial}{\partial a}\frac{\partial}{\partial t}\left(\rho\vec{u}\right) + \frac{\partial}{\partial a}\nabla\cdot\left(\rho\vec{u}\vec{u}\right) = -\frac{\partial}{\partial a}\nabla p + \frac{\partial}{\partial a}\nabla\cdot\bar{\bar{\tau}} + \frac{\partial \rho\vec{g}}{\partial a} + \frac{\partial \vec{F}}{\partial a} \tag{3.19}$$

$$\begin{aligned}\frac{\partial}{\partial a}\frac{\partial}{\partial t}\left(\rho E\right) + \frac{\partial}{\partial a}\nabla\cdot\left(\vec{u}\left(\rho E + p\right)\right) &= \frac{\partial}{\partial a}\nabla\cdot\left(\lambda_{eff}\nabla T - \sum_k h_k\vec{J}_k + \left(\bar{\bar{\tau}}_{eff}\cdot\vec{u}\right)\right) \\ &\quad + s_{\dot{w}_T} + \frac{\partial S_h}{\partial a} + \frac{\partial S_{\vec{F}}}{\partial a}\end{aligned} \tag{3.20}$$

$$\frac{\partial p}{\partial a} = \frac{\partial}{\partial a}\left(\rho RT\right) \ . \tag{3.21}$$

Since shape sensitivity is not considered in the scope of this research, the coordinates and time are not functions of the parameter. Consequently the partial derivatives shown in the above

equations can be interchanged. Using the sensitivity notation introduced previously and neglecting the superscript for simplicity, the sensitivity equations are rewritten as

$$\frac{\partial s_\rho}{\partial t} + \nabla \cdot (s_{\rho\vec{u}}) = 0 \tag{3.22}$$

$$\frac{\partial}{\partial t}\left(s_{\rho Y_k}\right) + \nabla \cdot \left(s_{\rho\vec{u}Y_k}\right) = -\nabla \cdot s_{\vec{J}_k} + s_{\dot{w}_k} + s_{S_k} \tag{3.23}$$

$$\frac{\partial}{\partial t}\left(s_{\rho\vec{u}}\right) + \nabla \cdot \left(s_{\rho\vec{u}\vec{u}}\right) = -\nabla s_p + \nabla \cdot s_{\overline{\overline{\tau}}} + s_{\rho\vec{g}} + s_{\vec{F}} \tag{3.24}$$

$$\frac{\partial}{\partial t}\left(s_{\rho E}\right) + \nabla \cdot s_{\left(\vec{u}(\rho E + p)\right)} = \nabla \cdot s_{\left(\lambda_{eff}\nabla T - \sum_k h_k \vec{J}_k + \left(\overline{\overline{\tau}}_{eff} \cdot \vec{u}\right)\right)} + s_{\dot{w}_T} + s_{S_h} + s_{S_{\vec{F}}} \tag{3.25}$$

$$s_p = s_{\rho RT} \ , \tag{3.26}$$

with boundary conditions

$$s_{Q(\vec{x},t)} = s_{f(\vec{x},t)} \qquad \text{on } \Gamma_D \ , \tag{3.27a}$$

and

$$\frac{\partial s_Q}{\partial \vec{n}}\left(\vec{x},t\right) = s_{g(\vec{x},t)} \qquad \text{on } \Gamma_N \ . \tag{3.27b}$$

Note that all the complicated sensitivity terms can be expanded by the chain rule and broken into the sensitivities of primary variables. For example, $s_{\rho\vec{u}} \equiv \frac{\partial}{\partial a}\left(\rho\vec{u}\right) = \frac{\partial \rho}{\partial a}\vec{u} + \rho\frac{\partial \vec{u}}{\partial a} \equiv s_\rho \vec{u} + \rho s_{\vec{u}}$. The sensitivities of property variables shown in Section 3.1.1 can also be expressed as the combination of primary variables and their sensitivities. It is evident that the unknowns of CSEs are sensitivities of primary variables and the primary variables obtained from the governing equations become known coefficients for sensitivity terms.

Quantitative analysis of the stability of a thermoacoustic system is performed by evaluating the Rayleigh index Ω. Recall that

$$\Omega = \int_0^\tau \int_0^V p'\left(\vec{x},t\right)\dot{Q}'\left(\vec{x},t\right) dVdt \ . \tag{3.28}$$

The sensitivity of Rayleigh index s_Ω is computed as follows to explore the effects of different boundary conditions on the stability of system:

$$s_\Omega = \int_0^\tau \int_0^V s_{\left(p'(\vec{x},t)\dot{Q}'(\vec{x},t)\right)} dVdt = \int_0^\tau \int_0^V \left(s_{p'(\vec{x},t)}\dot{Q}'\left(\vec{x},t\right) + p'\left(\vec{x},t\right) s_{\dot{Q}'(\vec{x},t)}\right) dVdt \ , \tag{3.29}$$

where $p' = p - p_0$ and $\dot{Q}' = \dot{Q} - \dot{Q}_0$ represent the fluctuations of pressure and heat release rate, respectively. p_0 and $\dot{Q}_0$ are the mean values of pressure and heat release rate. $s_{p'} = s_p - s_{p_0}$ and $s_{\dot{Q}'} = s_{\dot{Q}} - s_{\dot{Q}_0}$ correspondingly represent sensitivities of the fluctuations of pressure and heat release rate, respectively. The sensitivity of mean pressure is denoted by s_{p_0} and estimated by the mean value of pressure sensitivity, $\overline{s}_p$. Similarly, the sensitivity of mean heat release rate is denoted by $s_{\dot{Q}_0}$ and approximated by the mean value of sensitivity of heat release rate, $\overline{s}_{\dot{Q}}$.

3.2.2 Features of CSEM

Observation of the derivation of CSEs leads to the following findings:

1. Even if the original problem is nonlinear, the sensitivity equations are linear. The sensitivity of nonlinear terms is broken down into sensitivities of individual primary variables with known coefficients. This feature makes the solving process of the system of CSEs faster by taking the advantage of linear algebra. However, the present study utilizes an explicit solver for one-dimensional thermoacoustic convection problem and an iterative solver for the self-excited Rijke tube problem. Because the CSEs are derived from the governing equations by direct differentiation, these two sets of equations share the same structure. Thus, the developed solvers are applicable to both nonlinear governing equations and linear sensitivity equations. Using the same solver for both sets of equations keeps the consistency of computing process and provides a means of validating the solver by comparing the CFD results from the developed solver and other commercial software.
2. Only one nonlinear solution of the original problem is required. This feature is apparent by noting that the reference CFD solution at a specific time is incorporated into the CSEs and the values of primary variables appear as coefficients for sensitivity terms. Sensitivities to different parameters can be obtained by changing the boundary conditions and computing the CSEs with new boundary conditions.
3. Due to the above two characteristics, evaluation of the sensitivities using CSEM is potentially faster than using finite difference approximations. For a CFD problem

requiring considerable computational source and time, the saving by applying the CSEM is enormous.

Chapter 4

One-dimensional Thermally Induced Acoustics

Before performing the sensitivity analysis for the self-excited Rijke tube with reacting flow, a one-dimensional thermally induced acoustics problem has been chosen as the test bench for assessing the sensitivity method proposed to solve the complex thermoacoustic instability problem. This selected problem about thermoacoustic convection under a low-gravity environment has been studied back in 1970s [12], motivated by the significant thermoacoustic motions occurred in space manufacturing processes involving heated fluids. The explicit finite difference method employed in the prior research is also applied to the sensitivity calculations in the present study to reduce the error due to the usage of different schemes.

4.1 Problem statement

As shown in Figure 4.1, this one-dimensional model consists of two infinite parallel plates bounding a compressible fluid, which is Helium in this case. A sharp rise in temperature is imposed along one plate, consequently inducing pressure waves to propagate through the fluid. Several assumptions are made for this one-dimensional model according to the simplified model proposed by Spradley *et al*. [12]:

1. Newtonian fluid that obeys the Stokes viscosity hypothesis.
2. Constant thermal properties for heat conductivity λ , specific heat at constant volume c_V , viscosity μ and specific heat ratio $\gamma = c_p / c_V$.
3. Negligible body forces for low-gravity environment.
4. No heat sources, namely S_h in Equation 3.6 vanishes.
5. No viscous dissipation of energy, namely $\bar{\bar{\tau}}_{eff}$ term in Equation 3.6 is neglected.
6. Ideal gas, so that Equation 3.15 is applied.

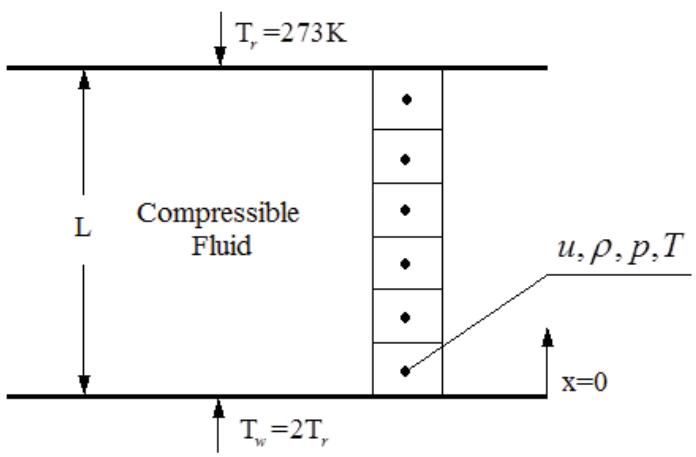

Figure 4.1: Computational model of the thermoacoustic convection problem.

4.2 Mathematical model

Based on the assumptions proposed in Section 4.1, the following system of one-dimensional governing equations is obtained from the general form of governing equations in Section 3.1.1:

1. Conservation of mass:

$$\frac{\partial \rho}{\partial t} + \frac{\partial}{\partial x}(\rho u) = 0 \ . \tag{4.1}$$

2. Conservation of momentum:

$$\frac{\partial}{\partial t}(\rho u) + \frac{\partial}{\partial x}(\rho u u) = -\frac{\partial p}{\partial x} + \frac{4}{3}\mu \frac{\partial^2 u}{\partial x^2} \ . \tag{4.2}$$

3. Conservation of energy:

$$c_V \frac{\partial}{\partial t}(\rho T) + c_V \frac{\partial}{\partial x}(\rho u T) = -p\frac{\partial u}{\partial x} + \lambda \frac{\partial^2 T}{\partial x^2} \quad . \tag{4.3}$$

4. Equation of state:

$$p = \rho R T \quad . \tag{4.4}$$

In fluid dynamics, the nondimensional form of Navier-Stokes equations is often used to reveal the intrinsic characteristics of the flow system. Indicated by asterisks, the nondimensional variables for the above governing equations are defined as follows:

$$x^* = \frac{x}{L}, \quad p^* = \frac{p}{p_r}, \quad \rho^* = \frac{\rho}{\rho_r}, \quad T^* = \frac{T}{T_r}, \quad u^* = \frac{u}{\sqrt{RT_r}}, \quad t^* = \frac{t}{L/\sqrt{RT_r}} \quad . \tag{4.5}$$

The nondimensional numbers that characterize the thermoacoustic problem studied are also introduced as below:

$$Re = \frac{\rho_r \sqrt{RT_r}\, L}{\mu}, \quad Pr = \frac{\mu c_p}{\lambda} \quad . \tag{4.6}$$

Since the reference values for nondimensional variables and thermal properties with prescribed assumptions are all constants, the Reynolds number Re and the Prandtl number Pr both remain constant. Reference values and thermal properties for Helium are given in Table 4.1 [12].

Table 4.1: Reference values and thermal properties for Helium.

Reference	Value	Property	Value
L	0.153 m	μ	1.875×10^{-5} kg/(m·s)
p_r	1.01×10^{5} Pa	Λ	0.144 J/(m·s·K)
ρ_r	0.19 kg/m^3	c_V	3.278×10^{3} J/(kg·K)
T_r	273K	γ	1.66
$u_r = \sqrt{RT_r}$	768m/s	$T_w = 2T_r$	

Substituting the nondimensional variables in Equation 4.5 and nondimensional numbers in Equation 4.6 into Equations 4.1-4.4 yields the following governing equations in nondimensional form:

1. Conservation of mass:

$$\frac{\partial \rho^*}{\partial t^*} + \frac{\partial}{\partial x^*}\left(\rho^* u^*\right) = 0 \ . \tag{4.7}$$

2. Conservation of momentum:

$$\frac{\partial}{\partial t^*}\left(\rho^* u^*\right) + \frac{\partial}{\partial x^*}\left(\rho^* u^* u^*\right) = -\frac{\partial p^*}{\partial x^*} + \frac{4}{3Re}\frac{\partial^2 u^*}{\partial x^{*2}} \ . \tag{4.8}$$

3. Conservation of energy:

$$\frac{\partial}{\partial t^*}\left(\rho^* T^*\right) + \frac{\partial}{\partial x^*}\left(\rho^* u^* T^*\right) = -(\gamma - 1)\, p^* \frac{\partial u^*}{\partial x^*} + \frac{\gamma}{RePr}\frac{\partial^2 T^*}{\partial x^{*2}} \ . \tag{4.9}$$

4. Equation of state:

$$p^* = \rho^* T^* \ . \tag{4.10}$$

The implicit differentiation of Equations 4.7-4.10 yields the corresponding sensitivity equations in nondimensional form:

$$\frac{\partial s_{\rho^*}}{\partial t^*} + \frac{\partial}{\partial x^*} s_{\rho^* u^*} = 0 \tag{4.11}$$

$$\frac{\partial}{\partial t^*} s_{\rho^* u^*} + \frac{\partial}{\partial x^*} s_{\rho^* u^* u^*} = -\frac{\partial s_{p^*}}{\partial x^*} + \frac{4}{3Re}\frac{\partial^2 s_{u^*}}{\partial x^{*2}} \tag{4.12}$$

$$\frac{\partial}{\partial t^*} s_{\rho^* T^*} + \frac{\partial}{\partial x^*} s_{\rho^* u^* T^*} = -(\gamma - 1)\left(s_{p^*}\frac{\partial u^*}{\partial x^*} + p^* \frac{\partial s_{u^*}}{\partial x^*}\right) + \frac{\gamma}{RePr}\frac{\partial^2 s_{T^*}}{\partial x^{*2}} \tag{4.13}$$

$$s_{p^*} = s_{\rho^*} T^* + \rho^* s_{T^*} \ . \tag{4.14}$$

As a test bench problem of the application of CSEM to the prediction of thermoacoustic instabilities, the heated wall temperature T_w is selected as the boundary condition to be investigated. The governing equations with initial and boundary conditions are differentiated with respect to T_w, constituting a well-posed problem for continuous sensitivity analysis.

The fluid is at rest initially with ambient conditions. A temperature rise T_w is imposed at $t = 0\text{s}$ and maintained at the bottom wall. Boundary conditions for both governing equations and sensitivity equations are summarized in Table 4.2, employing the values of nondimensional variables.

Table 4.2: Boundary condition summary for one-dimensional thermoacoustic problem.

Boundary Conditions		Governing Equations	CSEs
Bottom wall	Velocity	$u^* = 0$	$s_{u^*} = 0$
	Temperature	$T_w^* = 2$	$s_{T_w^*} = 1$
Top wall	Velocity	$u^* = 0$	$s_{u^*} = 0$
	Temperature	$T_0^* = 1$	$s_{T_0^*} = 0$
Pressure		Neumann-type numerical boundary condition	
Density		Ideal gas law	

4.3 Numerical method

As previously mentioned in Section 3.2.2, the same explicit finite difference scheme is used to solve both governing and sensitivity equations for the thermoacoustic convection problem. The discretized governing equations were already derived by Spradley *et al*. [12], thus this section is devoted to the discretization and solving processes of CSEs.

4.3.1 Discretization

The present algorithm uses forward difference in time and central difference in space except the convection terms for which the upwind differencing scheme is employed. The accuracy of this first-order scheme was assessed by Spradley *et al*. [12], who compared the results of this problem using the upwind scheme with those using a second order scheme and verified that this scheme exhibited sufficient accuracy.

Figure 4.1 shows the arrangement of field variables and their sensitivities in a cell volume. All these variables are located in the cell center. Values on the cell faces are determined by interpolation of two adjacent cell-centered values. Boundary conditions are imposed with the aid of fictitious points outside the boundary. Let n denote the nth time step, i be the ith computational cell, and Δt^*, Δx^* be the time step size and spatial increment, respectively. Using the spatial difference operators, δ_x and δ_x^2 for the first-order derivative and second-order derivative, respectively, the following discretized sensitivity equations are obtained from Equations 4.11-4.13:

$$\frac{\left(s_{\rho^*}\right)_i^{n+1}-\left(s_{\rho^*}\right)_i^n}{\Delta t^*}+\delta_x\left(s_{\rho^* u^*}\right)_i^n=0 \tag{4.15}$$

$$\frac{\left(s_{\rho^* u^*}\right)_i^{n+1}-\left(s_{\rho^* u^*}\right)_i^n}{\Delta t^*}+\delta_x\left(s_{\rho^* u^* u^*}\right)_i^n=-\delta_x\left(s_{p^*}\right)_i^n+\frac{4}{3Re}\delta_x^2\left(s_{u^*}\right)_i^n \tag{4.16}$$

$$\frac{\left(s_{\rho^* T^*}\right)_i^{n+1}-\left(s_{\rho^* T^*}\right)_i^n}{\Delta t^*}+\delta_x\left(s_{\rho^* u^* T^*}\right)_i^n=-(\gamma-1)\left[s_{p^*}\delta_x\left(u^*\right)+p^*\delta_x\left(s_{u^*}\right)\right]_i^n+\frac{\gamma}{RePr}\delta_x^2\left(s_{T^*}\right)_i^n, \tag{4.17}$$

where the use of central difference operator δ_x can be illustrated by

$$\delta_x\left(s_{\rho^* u^*}\right)_i^n=\frac{\left(s_{\rho^* u^*}\right)_{i+1}^n-\left(s_{\rho^* u^*}\right)_{i-1}^n}{2\Delta x^*} \ . \tag{4.18}$$

One example for the use of δ_x^2 for the second-order derivative is

$$\delta_x^2\left(s_{u^*}\right)_i^n=\frac{\left(s_{u^*}\right)_{i-1}^n-2\left(s_{u^*}\right)_i^n+\left(s_{u^*}\right)_{i+1}^n}{\Delta x^{*2}} \ . \tag{4.19}$$

4.3.2 Explicit finite difference scheme

4.3.2.1 Solution procedure

As shown in Equations 4.15-4.17, sensitivity equations for mass, momentum and temperature are presented in the divergence form, instead of being expanded completely by the chain rule. Solving the set of sensitivity equations with explicit finite difference scheme consists of the following steps:

1. Initialize the sensitivity variables.

Since the flow is at rest initially, the sensitivity variables are zeros in the interior:

$$\left(s_{u^*}\right)_i^0=0,\quad \left(s_{p^*}\right)_i^0=0,\quad \left(s_{\rho^*}\right)_i^0=0,\quad \left(s_{T^*}\right)_i^0=0 \ . \tag{4.20}$$

Starting from the initial conditions, the values of sensitivity variables at a new time level are directly updated using the values at the current time level based on the fully explicit scheme. The following steps are repeated for each new time step until the designated end time is reached.

2. Advance the sensitivity of mass flux.

An important variable for the present research is defined as $g = \rho u$, which is the mass flux or momentum per unit volume that is related to the mass flow rate by $\dot{m} = \rho u A = gA$, where A is the cross section area of flow. Base on the nondimensional variables given in Equation 4.5, the nondimensional mass flux is computed as $g^* = \rho^* u^*$. Solving the sensitivity equation for momentum, Equation 4.16, for the sensitivity of mass flux yields:

$$\left(s_{g^*}\right)_i^{n+1} = \left(s_{g^*}\right)_i^n - \Delta t^* \left[\delta_x \left(s_{g^* u^*}\right)_i^n + \delta_x \left(s_{p^*}\right)_i^n - \frac{4}{3Re} \delta_x^2 \left(s_{u^*}\right)_i^n \right] . \tag{4.21}$$

The convection term, $s_{g^* u^*}$, is computed as $s_{g^* u^*} = s_{g^*} u^* + g^* s_{u^*}$ and u^* and g^* are obtained from the CFD simulation results.

3. Advance the sensitivity of density.

The sensitivity equation for mass, Equation 4.15, is solved to obtain the sensitivity of density at a new time step:

$$\left(s_{\rho^*}\right)_i^{n+1} = \left(s_{\rho^*}\right)_i^n - \Delta t^* \delta_x \left(s_{\rho^* u^*}\right)_i^n . \tag{4.22}$$

4. Calculate the sensitivity of velocity.

With the advanced sensitivities of mass flux and density acquired from Equations 4.21 and 4.22, respectively, the sensitivity of velocity at the new time level can obviously be computed as

$$s_{u^*}^{n+1} = \left(s_{g^*}^{n+1} - u^{*n+1} s_{\rho^*}^{n+1} \right) / \rho^{*n+1} . \tag{4.23}$$

5. Advance the sensitivity of temperature.

Equation 4.17 is solved to evolve the sensitivity of temperature:

$$\left(s_{\rho^* T^*}\right)_i^{n+1} = \left(s_{\rho^* T^*}\right)_i^n - \Delta t^* \left\{ \delta_x \left(s_{\rho^* u^* T^*}\right)_i^n + (\gamma - 1) \left[s_{p^*} \delta_x \left(u^*\right) + p^* \delta_x \left(s_{u^*}\right) \right]_i^n - \frac{\gamma}{RePr} \delta_x^2 \left(s_{T^*}\right)_i^n \right\} . \tag{4.24}$$

9. Evaluate equation of state.

Equation 4.14 is used to compute the sensitivity of pressure at the new time step with known primary variables from CFD simulation results and sensitivity variables from preceding steps.

10. Compute the sensitivity of Rayleigh index.

Equation 3.29 is applied to compute the sensitivity of Rayleigh index with dimensional variables. The field variables and sensitivity variables are obtained from CFD simulations and sensitivity computation, respectively. The heated wall plays the role of heat addition, resulting in heat release fluctuations due to the variation of temperature gradients. Distinguished from the variable $\dot{Q}$ in Equation 3.29 which represents the heat release rate per unit volume, the total heat release rate through a surface in the fluid is used for this problem. For the heated wall, the heat releaser rate is denoted by $\dot{Q}_w$ and computed as

$$\dot{Q}_w = \lambda \frac{T_w - T_1}{\frac{1}{2}\Delta x} A \ . \tag{4.25}$$

It is noted that the area of contact surface is designated to be 1 for the one-dimensional problem. Similarly, the sensitivity of heat release rate is presented as

$$s_{\dot{Q}_w} = \lambda \frac{s_{T_w} - s_{T_1}}{\frac{1}{2}\Delta x} A \ . \tag{4.26}$$

Sensitivity of the Rayleigh index can be calculated as

$$s_\Omega = \int_0^\tau s_{\left(p'(t)\dot{Q}_w'(t)\right)} dt = \int_0^\tau \left(s_{p'(t)} \dot{Q}_t'(t) + p'(t) s_{\dot{Q}_w'(t)} \right) dt \ . \tag{4.27}$$

where p' and Q_w' are the fluctuating components of pressure and hear release rate, respectively. $s_{p'}$ and $s_{Q_w'}$ are the sensitivities of pressure and heat release rate fluctuations, respectively.

4.3.2.2 Numerical stability

The present numerical method is evaluated from two aspects, i.e. stability and accuracy. The latter is discussed in Section 4.4.2.

The explicit finite difference method is easy to implement, but conditionally stable. The time step size Δt is restricted by the Courant–Friedrichs–Lewy (CFL) condition:

$$\Delta t < \left[\frac{\Delta x}{|u| + c} \right]_{\min} , \tag{4.28}$$

where c is the speed of sound and computed as $c = \sqrt{\gamma RT}$. This condition ensures the propagation of acoustic waves over one-cell distance Δx within one time step Δt . It is evident that the maximum time step size allowed corresponds to the use of the smallest cell size and

maximum speed of sound present in the model. With the data shown in Table 4.1, a time step size of 5.4×10^{-6} s or less is required for 20 uniform cells based on the CFL condition. In the nondimensional formulation, the time step size is in the order of 0.01.

4.4 Results

4.4.1 CFD simulation

Temporal evolution of pressure is shown in Figure 4.2. Nondimensional pressure is employed to make comparison with the data provided in the reference [12]. The three plots display the pressure time history from initial state to 1000 units of nondimensional time which correspond to 0.2s in real time. The vertical axis denotes the normalized pressure. Figure 4.2(a) exhibits pressure oscillations at the middle point of the distance between two plates. It is noted that the pressure oscillations tend to quasi-steady status with nondimensional mean pressure at about 1.3 as the growth rate of pressure decreases. The amplitude of oscillations is also reduced as the increase rate of mean pressure approaches zero. Figures 4.2 (b) and (c) compare the spatially averaged pressure obtained from the present study and the reference, respectively. The agreement of the mean pressure time history provides a solid basis for sensitivity analysis.

The pressure distribution is depicted in Figure 4.3 at four different time points. It can be seen that the pressure profile represents the first harmonic, which is supported by Figure 4.5.

The acoustic nature of the observed traveling waves is verified by estimating their frequency and comparing with the natural frequencies of the present system. Figure 4.4 shows the first 500 time steps of evolution of velocity at the center between two plates. The velocity oscillates around the mean of zero, instead of an increasing mean value as the pressure time history displays. The FFT plot in Figure 4.5 gives the dominant frequency of velocity oscillations, which turns out to be 3297Hz, so the period $\tau = 303\mu s$ is used to compute the Rayleigh integral. The fundamental frequency of this system can be determined by f = c/2L= $c = \sqrt{\gamma RT}$. With the parameters given in Table 4.1, the fundamental frequency is calculated to be 3233Hz, which is close to the FFT result with a slightly shift, confirming that the first acoustic mode has been

excited. Figure 4.5 also shows that more than one resonance frequencies exist, resulting in the sub-peaks seen in Figure 4.4.

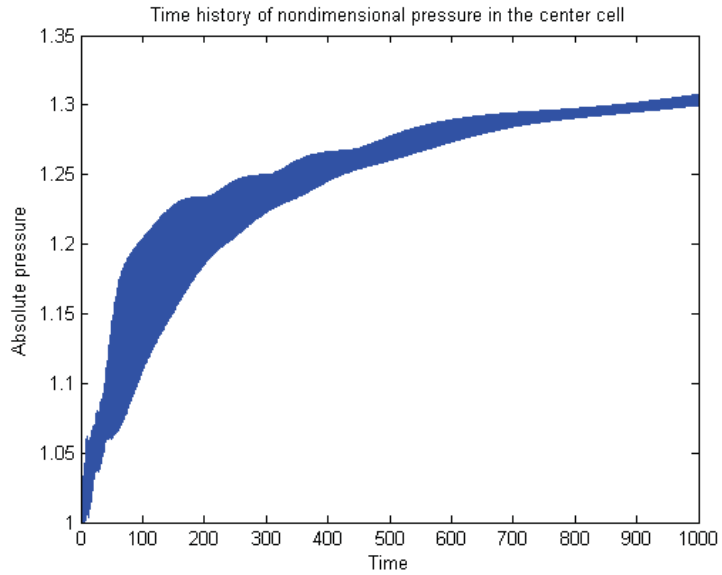

(a)

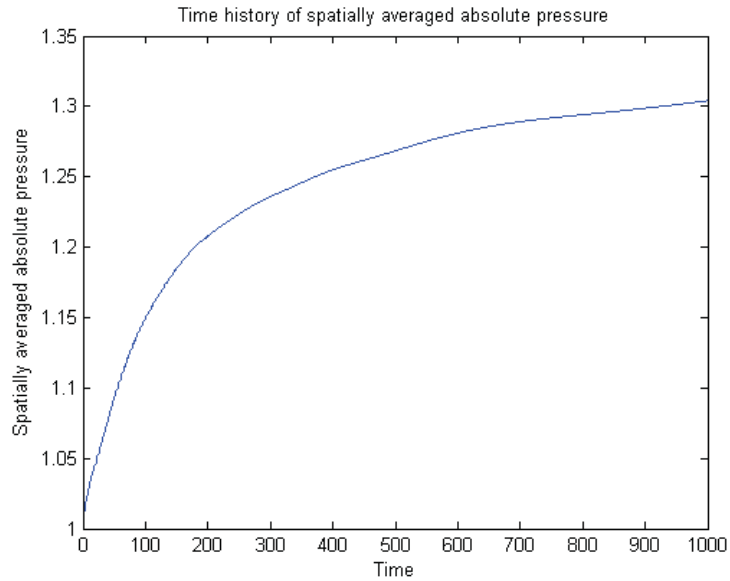

(b)

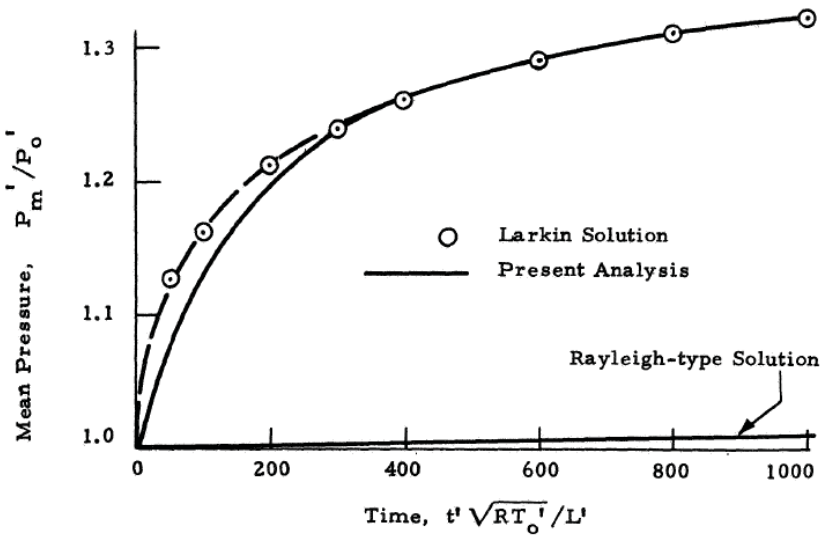

(c)

Figure 4.2: Pressure time history of one-dimensional thermally induced acoustics (a) at the center, (b) spatially averaged, (c) Spradley [12].

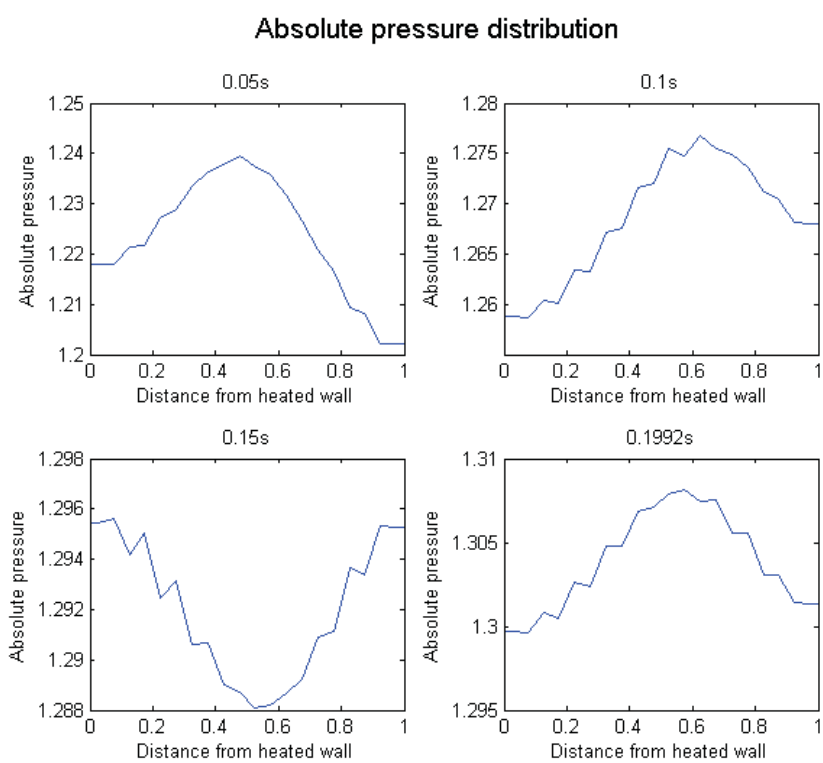

Figure 4.3: Pressure distribution at four different time points.

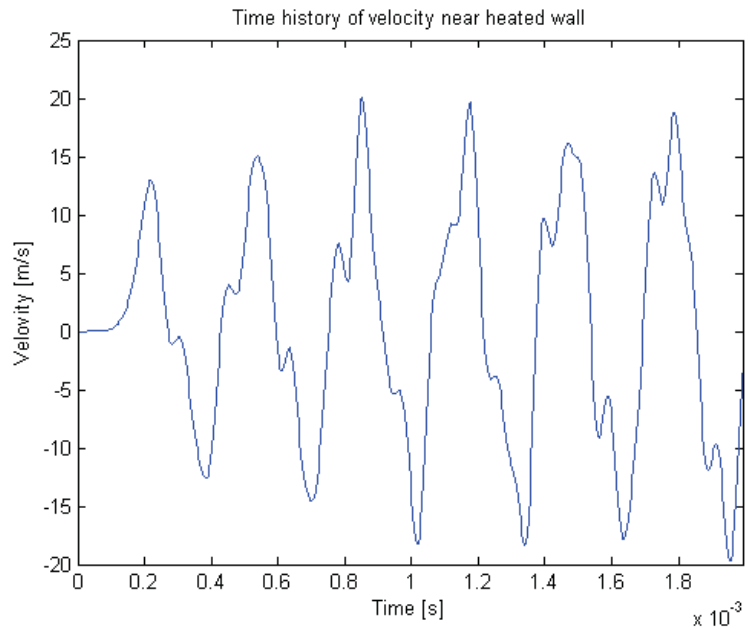

Figure 4.4: Evolution of velocity at the center between two plates [m/s].

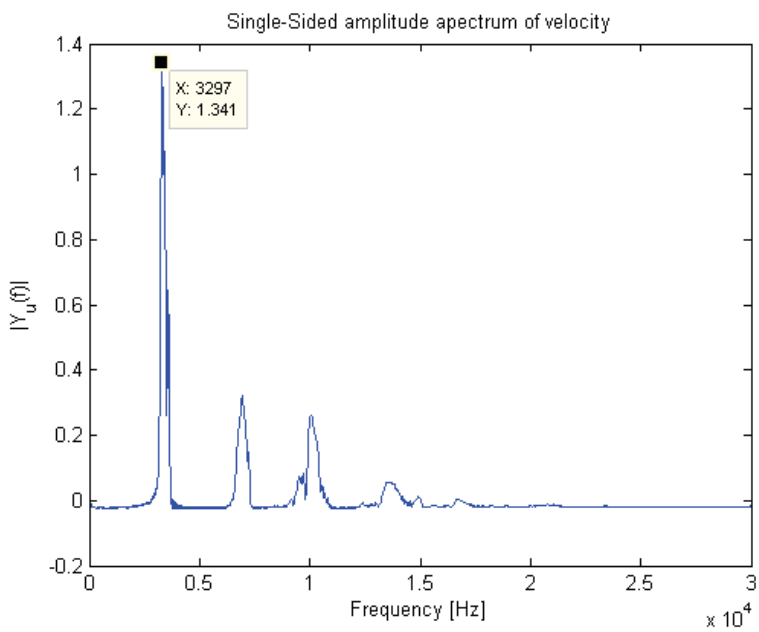

Figure 4.5: Frequency components of velocity oscillations.

In order to demonstrate the thermoacoustic effects in this problem, the Rayleigh criterion is described graphically and evaluated numerically. Figures 4.6 (a) and (b) display the coupling between pressure and heat release rate fluctuations at around 0.02s for a cell adjacent to the heated wall and at the center, respectively. It is noted that the pressure and heat release rate

fluctuations are out of phase for the cell near the heated wall and in phase for the cell at the center. Since the mean values are obtained by taking the average of data at all the time points, the fluctuating components show negative values during this time interval. Figures 4.7 (a) and (b) illustrate the trend of Rayleigh indices integrated over each period at two locations corresponding to Figures 4.6 (a) and (b), respectively. The Rayleigh indices at both locations reach zero at 0.06s approximately and remain at zero. The negative Rayleigh index at around 0.02s for the cell near the heated wall is consistent with the out-of-phase relationship between pressure and heat release rate fluctuations indicated in Figure 4.6(a). The positive Rayleigh index at around 0.02s for the cell at the center has agreement with the in-phase relationship between pressure and heat release rate fluctuations shown in Figure 4.6(b). The opposite signs of Rayleigh indices at different locations for a given period suggest that the thermoacoustic instability is an overall effect explained by the Rayleigh criterion.

Figure 4.8 shows the integrated Rayleigh index over the entire computational domain for each period. The oscillatory Rayleigh index presents large amplitudes between 0.01s and 0.03s. With the larger positive Rayleigh index, pressure oscillations continue to grow. The amplitude of the integrated Rayleigh index deceases in time and approaches zero at 0.14s, corresponding to the time when pressure oscillations approach the nondimensional value of 1.3 asymptotically as shown in Figure 4.2.

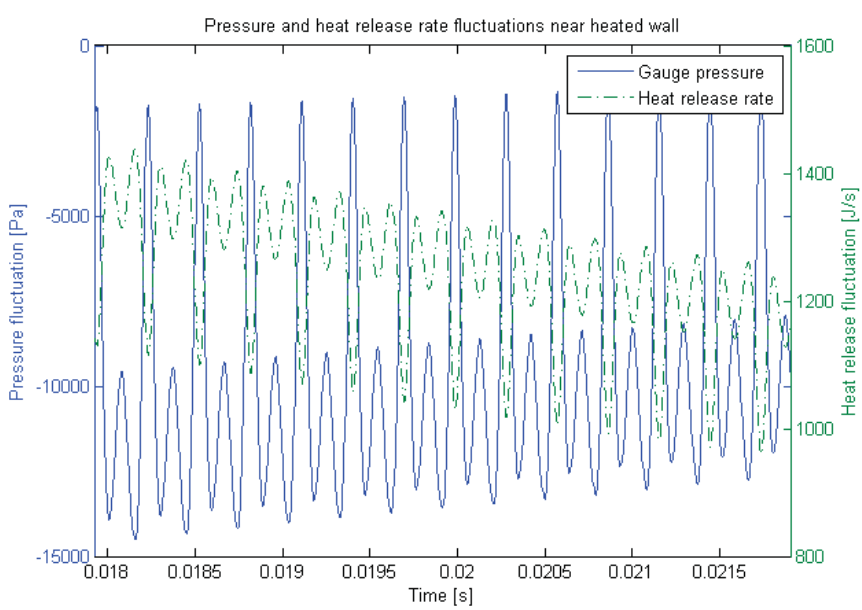

(a)

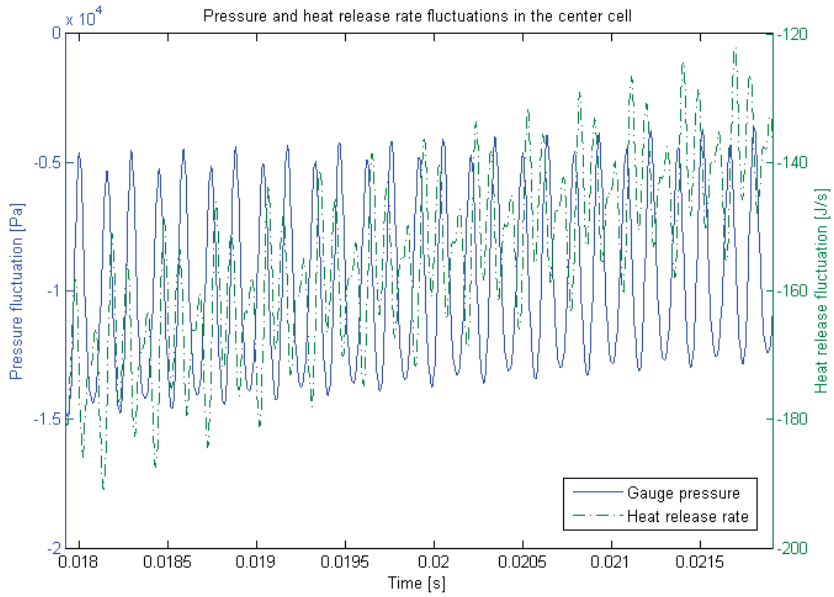

(b)

Figure 4.6: Pressure and heat release rate fluctuations from 0.018s to 0.0215s (a) near heated wall, (b) at the center.

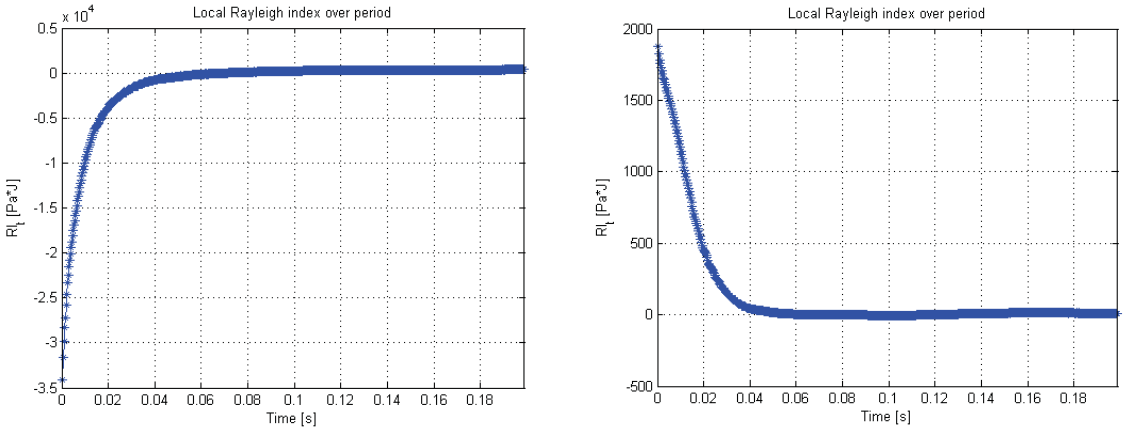

(a) (b)

Figure 4.7: Time evolution of the Rayleigh index (a) near heated wall, (b) at the center [Pa·J].

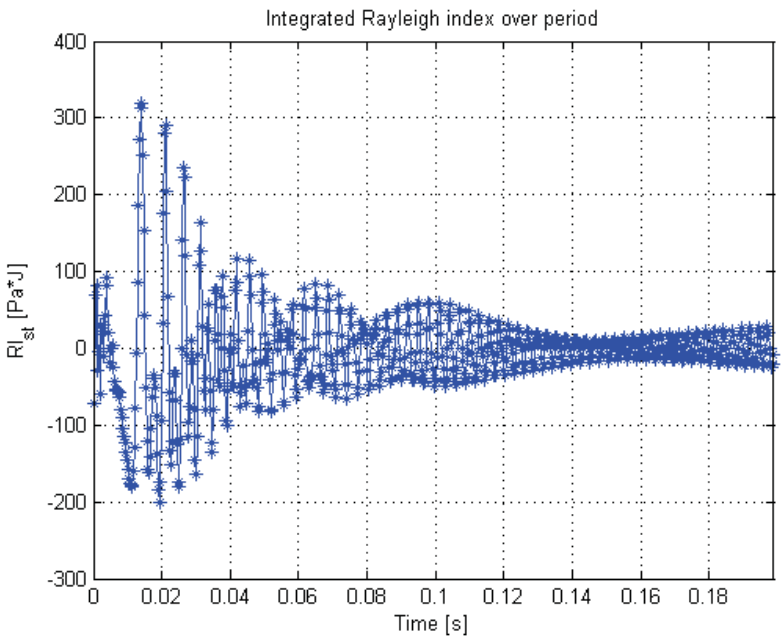

Figure 4.8: Time evolution of the integrated Rayleigh index over entire domain and oscillation period [Pa·J].

4.4.2 Sensitivity analysis

The sensitivity of the oscillating pressure due to the change in the heated-wall temperature can be predicted from Figure 4.9. It is evident from Figure 4.9, which shows the magnitudes of sensitivity values both near the heated wall and at the center between two plates, that the sensitivity magnitudes grow exponentially in time and reach 10^{30} Pa/K at 0.02s. The large sensitivity values indicate that pressure becomes extremely sensitive to the temperature variations even in the early stage. The temporal evolution of pressure sensitivities in the early stage is depicted in Figure 4.10. The sensitivity of pressure oscillates around zero, which implies that the increase in heated-wall temperature may lead to opposite effects on pressure changes in one oscillation cycle. It is intuitive that if the increased wall temperature causes an increase of pressure at the maximum point or a decrease at the minimum point in one cycle, pressure oscillations will be amplified.

The sensitivity of pressure not only varies in time, but also differs in space. Figure 4.11 demonstrates the development of pressure sensitivities over the entire computational domain for selected time points. The rapid change of sensitivity includes the increase of magnitude and localization.

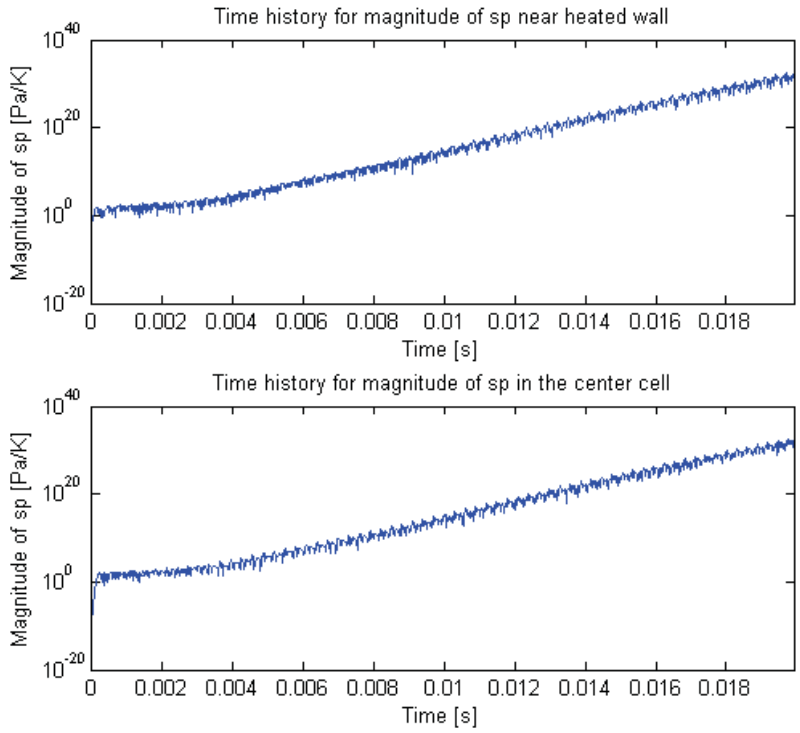

Figure 4.9: Time evolution of the magnitudes of pressure sensitivity [Pa/K].

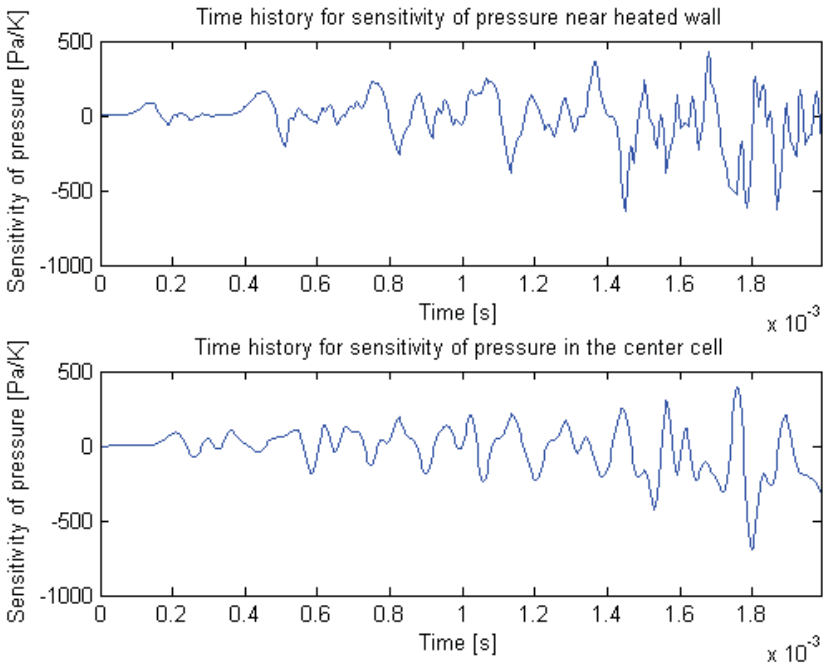

Figure 4.10: Time evolution of the sensitivity of pressure in the early stage (top) near heated wall, (bottom) at the center [Pa/K].

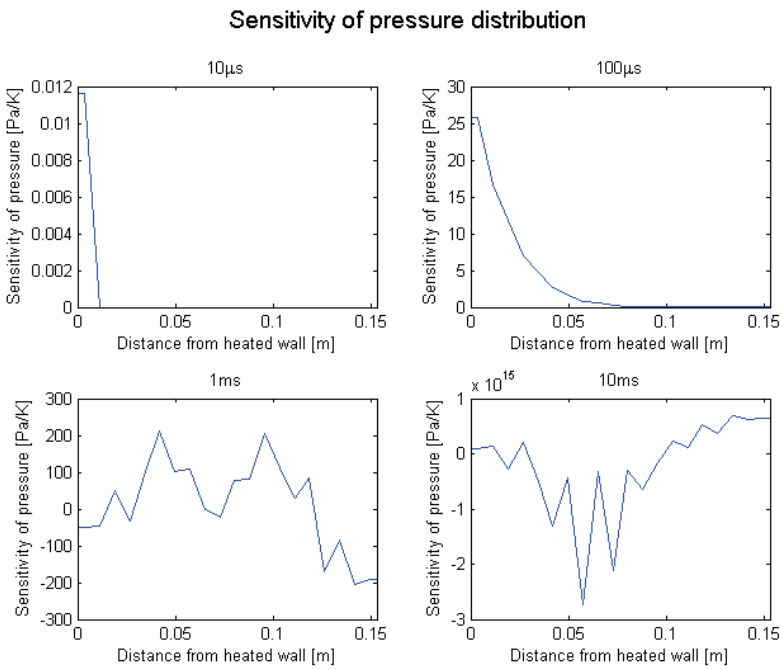

Figure 4.11: Distributions of the sensitivity of pressure at four different time points [Pa/K].

As the critical element in the computation of sensitivities of the Rayleigh index, sensitivities of pressure obtained from the CSEM analysis are validated against those from finite difference approximations. Nondimensional variables are used for Figures 4.12-4.14. Figure 4.12 compares the distribution of pressure sensitivities at a time point in the early stage of development, using the forward, backward and central differences and the CSEM, respectively. Good agreement has been achieved between the backward finite difference approximation and the CSEM results, except that the backward finite difference method leads to a high sensitivity value for the boundary that remains at the ambient temperature. Results using the forward difference approximation deviate from those using the other methods. The CSEM is further evaluated by comparing the nondimensional pressure predicted by the obtained sensitivity values and that directly calculated by the CFD simulation. Figure 4.13 shows the pressure distribution with 1% increase of the heated-wall temperature at the same time point as in Figure 4.12. Figure 4.14 describes the temporal evolution of pressure subject to the increased heated-wall temperature for a location at the center between two plates. In both plots, the CSEM results show great consistency with the CFD results. The relative errors for predicted pressure in Figure 4.13 and Figure 4.14 are 4.7×10^{-4} and 3.3×10^{-3} , respectively, indicating that the CSEM results are

accurate to 3 decimal digits. It is noted that the temporal prediction becomes less accurate as time marches on. The problem of accumulated error could be improved by refining the grid and time step size.

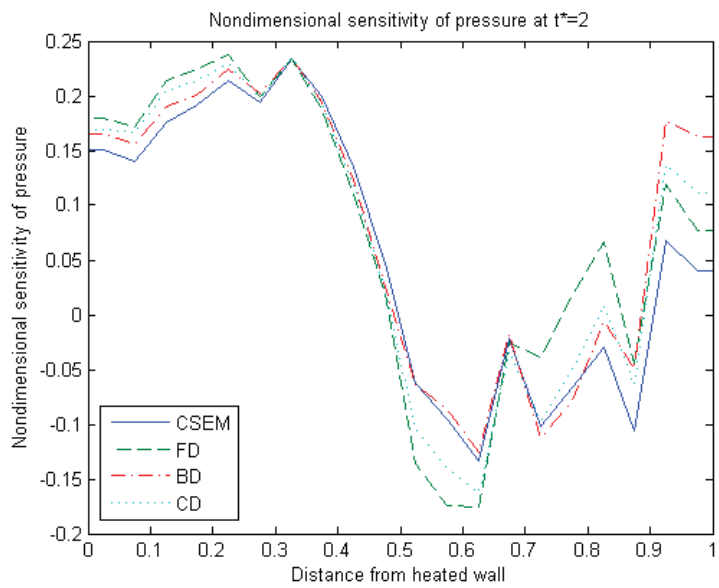

Figure 4.12: Comparison of nondimensional sensitivities of pressure computed by different methods.

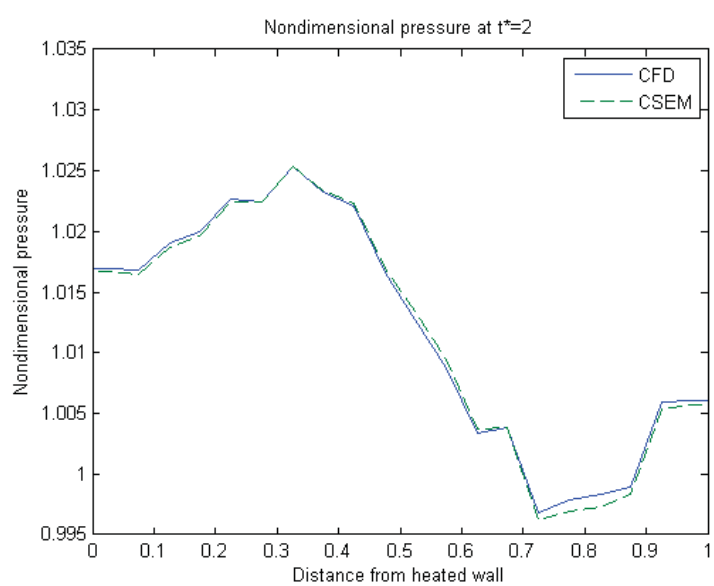

Figure 4.13: Comparison of the predicted pressure distribution by CFD computation and CSEM.

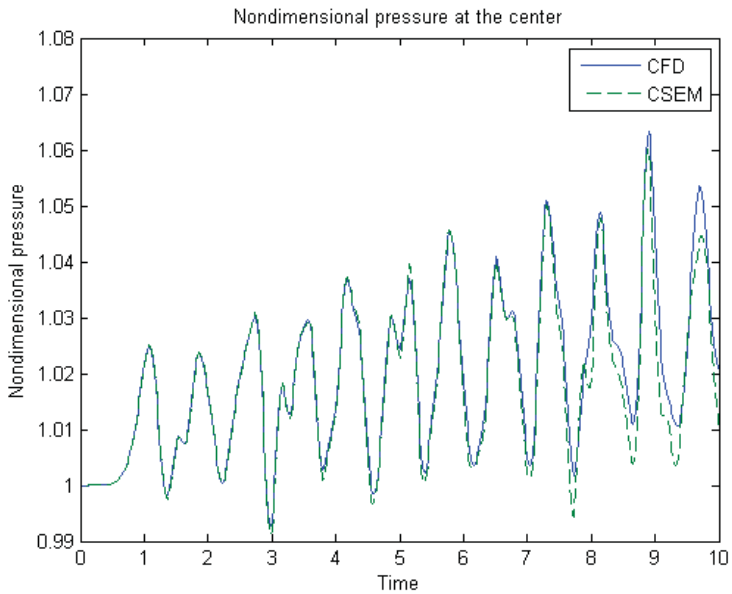

Figure 4.14: Comparison of the evolution of pressure predicted by CFD computation and CSEM.

With reliable sensitivity values of primary variables, the sensitivity of Rayleigh index is computed according to Equation 4.27. Figure 4.15 and 16 illustrates the development of Rayleigh index responses to variations in the heated-wall temperature for the points adjacent to the heated wall (P1) and at the center (P2), respectively. Similar to the evolution of the Rayleigh index, the trend of the Rayleigh index sensitivity for P1 is opposite to that of P2. The sensitivity of the Rayleigh index for P1 is positive at the beginning due to the increased heat flux, but monotonically deceasing with the decreased temperature gradient as heat transfers to the plate at the ambient temperature. At around 2.5ms, the sensitivity of the Rayleigh index becomes zero, and keeps decreasing to negative values. Different from P1, the responses of the Rayleigh index at P2 exhibit a monotonically increasing trend with a transition point at around 3.1ms. The delay of the transition point results from the propagation of acoustic waves and the heat transfer process. It is also noted that P1 possesses larger magnitude of sensitivities than P2, suggesting that P1 is more susceptible to the temperature variations. The difference in the strength of sensitivities at different locations leads to the use of the spatially averaged Rayleigh index sensitivity which reflects the overall effects of increased temperature at the boundary on thermoacoustic responses. As shown in Figure 4.17, the integrated sensitivity of the Rayleigh index is slightly above zero before 2.5ms, and a steep decreasing rate of the sensitivity is present

at round 3ms. The behavior of the Rayleigh index sensitivity demonstrates that the increase of the heated-wall temperature destabilizes the thermoacoustic convection process or mitigates the out-of-phase coupling effects at first, depending on the stability status of the system at a specific time point. The increased temperature boundary stabilizes the thermoacoustic convection process or reduces the in-phase coupling effects at a later time. The large sensitivity values after 3.5ms indicates that even a small variation in the boundary temperature is capable of changing the stability status of the system. Since the magnitude of the sensitivity value increases to an unrealistically large number, only a small portion of the sensitivity development is presented in Figure 4.17. Effective control on thermoacoustic convection can be performed in the early stage of the coupling process by varying the heating temperature at the boundary.

The one-dimensional thermoacoustic problem serves as a test bench for the application of CSEM. With the validation of the CSEM analysis conducted previously, the performance of CSEM can be extended to a two-dimensional geometry to explore the effects of misrepresentation of boundary conditions, not only in terms of the magnitude as one-dimensional problems, but also involving the distribution of influential boundary quantities. The mechanism can also be extended to include the reacting flow, increasing the complexity of formulation and difficulty in algorithm.

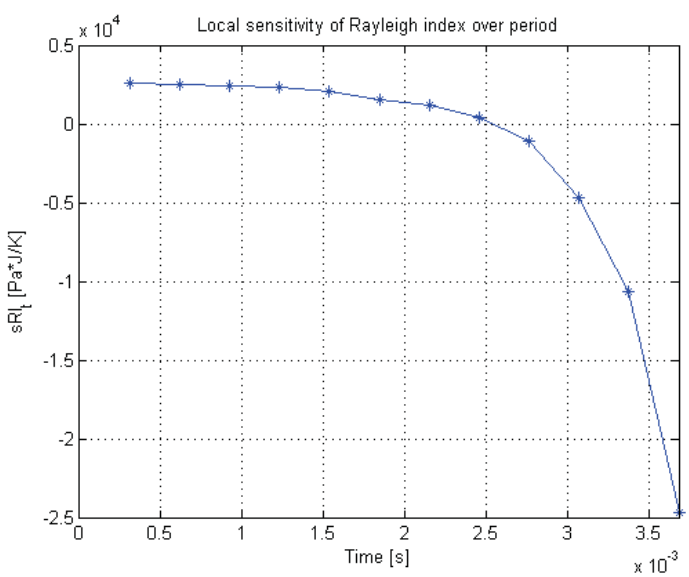

Figure 4.15: Time evolution of the sensitivity of the Rayleigh index near the heated wall [Pa · J/K].

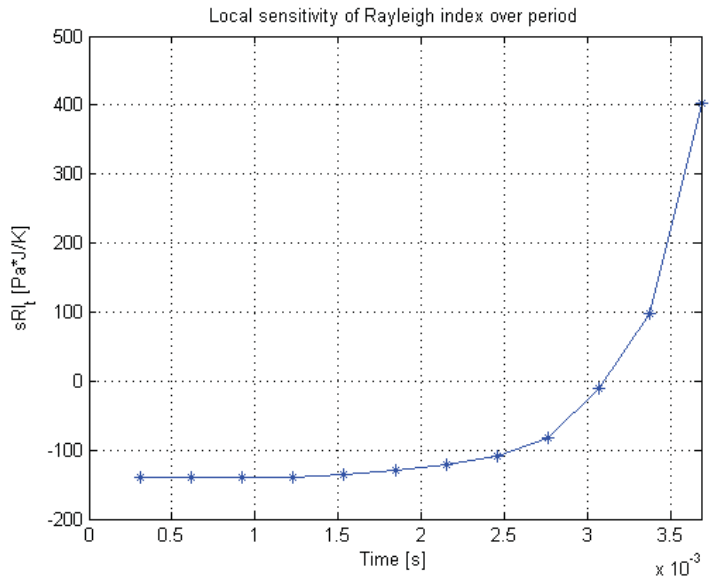

Figure 4.16: Time evolution of the sensitivity of the Rayleigh index at the center [Pa · J/K].

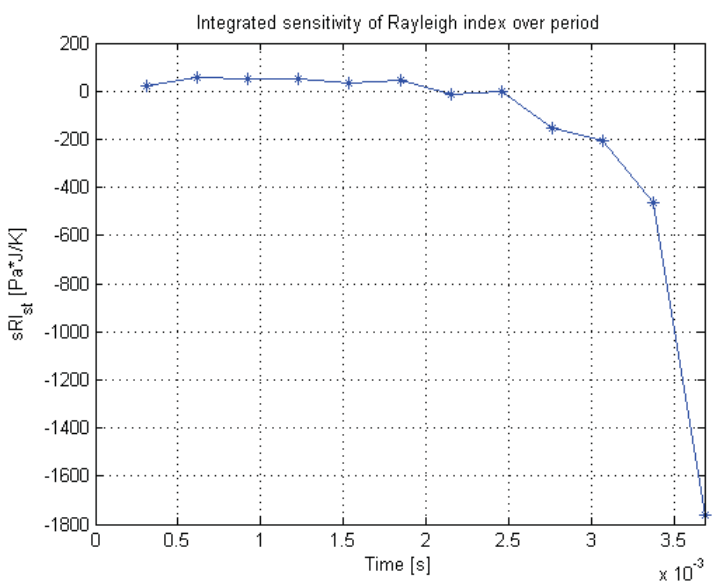

Figure 4.17: Time evolution of the integrated sensitivity of the Rayleigh index [Pa · J/K].

Chapter 5

Self-excited Thermoacoustic Instability in Rijke Tube

As a representative thermoacoustic device, the Rijke tube has been studied intensively to gain fundamental insights in to the mechanisms of thermoacoustic instabilities [15-17]. The remarkable CFD investigations of thermoacoustic instability in the two-dimensional Rijke tube using Fluent were conducted by Hantschk and Vortmeyer [6]. The number of concentric heating bands was reduced to save computational effort but thermal conductivity was enhanced to generate sufficient heat addition. Hantschk and Vortmeyer simulated the growth of pressure oscillations until reaching the limit cycle for two types of Rijke tubes. The open-open type of Rijke tube encloses heating elements positioned one quarter of the tube length away from the flow inlet. An imposed pressure disturbance excited oscillations at the fundamental frequency. The closed-open tube places the heating elements in the middle of the total length of tube, exciting pressure oscillations at the second acoustic mode. Both models were functional in capturing nonlinear effects that are responsible for the limit cycle. The behaviors of field variables satisfied the Rayleigh criterion. The results of the latter model agreed well with an experiment. However, the comparison was made for only one system condition, providing no information on the influence of different values of boundary parameters.

Chatterjee *et al*. [7] also utilized the commercial CFD software Fluent to simulate a two-dimensional Rijke tube with focus on capturing the detailed physics of reacting flows, results of which were supported by experiments. This self-excited Rijke tube is of the closed-open type, a

modified version of the original Rijke tube by replacing the hot gauges with flame. Second acoustic mode was excited by interactions between the oscillations of combustion-released heat and acoustic pressure. This model included a multi-channel honeycomb in the center of the tube to simulate the flame anchoring process so that flame-honeycomb coupling could be captured. The flame-sheet oscillated near the honeycomb leading to alteration of the amplitude of pressure oscillations in the limit cycle and variation in the heat addition to the acoustic field. The resulting "pulsating instability" [88] accounted for the sub-harmonic pressure oscillations observed in both experiments and CFD simulations.

The present research has adopted the advantages of previous work and conducted a comprehensive simulation of the Rijke tube which takes into account the effects of reaction mechanism, vorticity and radiation present in the physical processes. The goal of this detailed CFD simulation is to provide a solid reference state for continuous sensitivity analysis. Investigations of thermoacoustic instability responses to the change of boundary parameters set this research apart from others that aim only at reproducing and explaining a single or a few thermoacoustic problems in the Rijke tube combustor.

5.1 Problem statement

A conceptual model of the computational domains of the modified Rijke tube is shown in Figure 5.1. Premixed methane-air mixture flows into the tube combustor through the bottom, forming an acoustically closed inlet boundary. The mass flow rate and equivalence ratio could be adjusted to represent variations in the operating conditions. The top of the Rijke tube is open to the laboratory environment. A ceramic honeycomb flame holder is mounted in the center of the tube where the fuel-air mixture is ignited and the flame is anchored and stabilized.

The Rijke tube is representative of other combustion systems in that it experiences similar coupling processes from the onset of thermoacoustic instability phenomenon to the state of limit cycle. It also has some characteristics that simplify the study of simulation results. The large length-to-diameter ratio makes the acoustics primarily one-dimensional, and the vortex shedding is limited compared to a full-scale combustor.

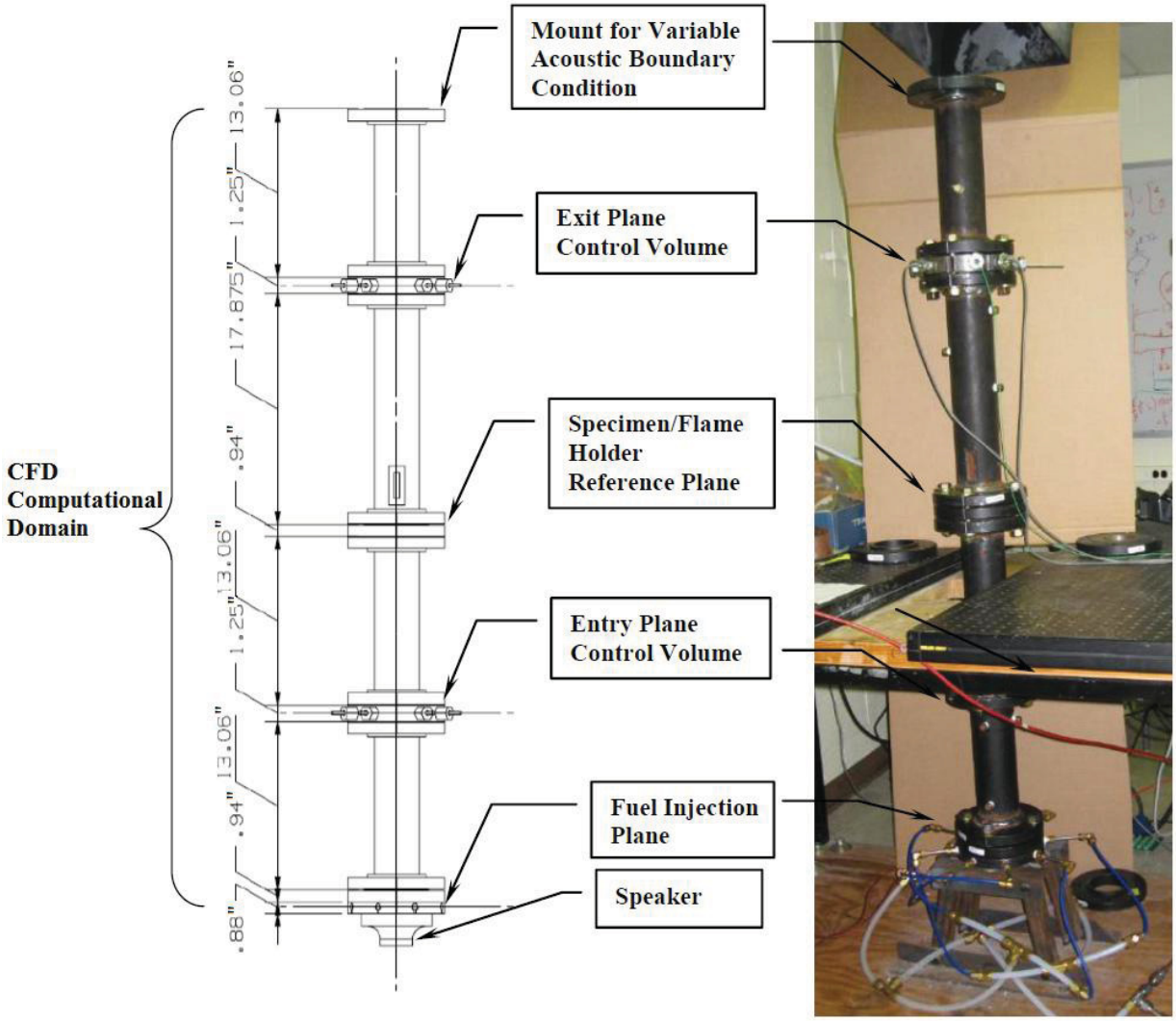

Figure 5.1: Rijke tube combustor experimental and computational domains.

In this research, the self-excited Rijke tube is modeled and simulated using the DNS to resolve physical process details involved in thermoacoustic instability phenomena. Despite the expensive computational cost, DNS is the most capable formulation for capturing all interactions between field variables that are associated with the driving mechanisms of thermoacoustic instabilities. More importantly, this "brute force" method exactly embodies the advantages of the application of CSEM to thermoacoustic problems, which will be studied in depth in the following sections. Prediction of the thermoacoustic instability behavior in a combustion system, in this case the Rijke tube, is realized by computing the sensitivities of Rayleigh index to different parameters using the sensitivities of field variables obtained by solving the CSEs. The

effects of two parameters on thermoacoustic instabilities are investigated in this research. These two selected parameters are the inlet momentum per unit volume, which is proportional to the mass flow rate, and the equivalence ratio.

5.2 CFD simulation

The commercial CFD software ANSYS Fluent 14.0 has been chosen to simulate the thermoacoustic instability phenomenon in the laboratory-scale Rijke tube described in Figure 5.1. The simulation takes into account the reacting flow, flame dynamics and radiation model to investigate the important physical processes in detail. The governing equations shown in Section 3.1.1 are employed except the gravity effects, and converted into a cylindrical coordinate system, which simplifies the computation greatly by treating the flow properties as axisymmetric.

5.2.1 Geometric model

Figure 5.2 displays the computational domain of the Rijke tube model, which is 61.875in (1.572m) in length, 2.9in (0.0737m) in the inner diameter, and 0.3in (0.00762m) thick for the steel tube wall. The corresponding laboratory-scale Rijke tube is vertically installed, while the

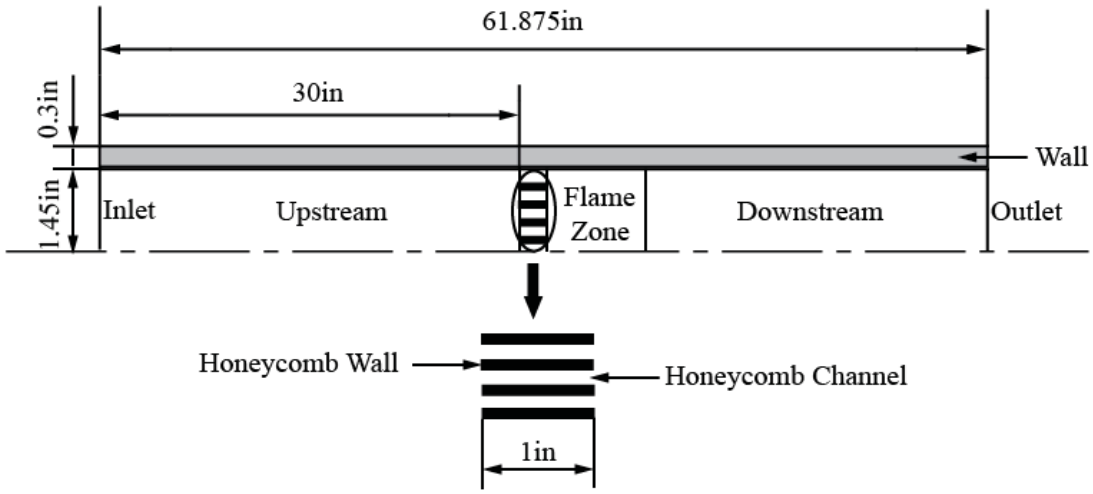

Figure 5.2: Configuration of the Axisymmetric Rijke tube model (not to scale).

geometric model is a horizontal one with the purpose of simplifying the computational model by defining a constant heat transfer coefficient between the outside tube wall and ambient air.

Because an axisymmetric configuration is adopted to represent the flow and heat fields, the total volume of the annular honeycomb channels is modeled to be equivalent to that of the actual square channels, which accounts for approximately half of the volume of the entire honeycomb.

The large aspect ratio of the Rijke tube model and the narrow channels existing in the honeycomb lead to a special treatment of meshing introduced in Section 5.2.2.

5.2.2 Mesh model

The disparate length scale subtlety increases the difficulty and complexity in mesh modeling. The large length-to-radius ratio of the tube requires a great number of grid points used to capture the flow field features. The presence of the honeycomb flame holder requires an extremely fine grid in the honeycomb zone and the areas adjacent to it. On the other hand, to accurately simulate the flame, the region downstream of the honeycomb should also possess a fine grid.

In order to achieve the requirement of a fine grid in some particular regions while keeping the rest of the fluid domain a reasonably smaller number of grid points, the interior of the tube is partitioned into four zones (defined in Figure 5.2) based on the positions of the honeycomb and flame: (1) upstream from the inlet to the bottom of honeycomb (including a small region for grid transition), (2) the honeycomb, (3) the flame zone downstream of the honeycomb which does not reflect the real flame thickness but large enough to house the flame, and (4) downstream from the end of flame zone to the outlet. A triangular grid was employed for the flame zone, region (3), and a small region upstream the honeycomb with a growth rate of 1.20. By using an unstructured grid, the size of quadrilateral cell transitions from the upstream to the honeycomb, then to the downstream, with a fine grid for the honeycomb as shown in Figure 5.3. This meshing method results in 33890 cells for the axisymmetric model, which approaches the minimum number of cells generated that is required to ensure the ability of the model to capture the fluid dynamics and flame dynamics naturally without incorporating analytical or empirical results.

By using an axisymmetric representation, the honeycomb channels are treated annular in the model rather than square in the real honeycomb. To minimize the impact of this modification in

geometry, the effective volume of honeycomb channels in the model is equivalent to the actual honeycomb flame holder.

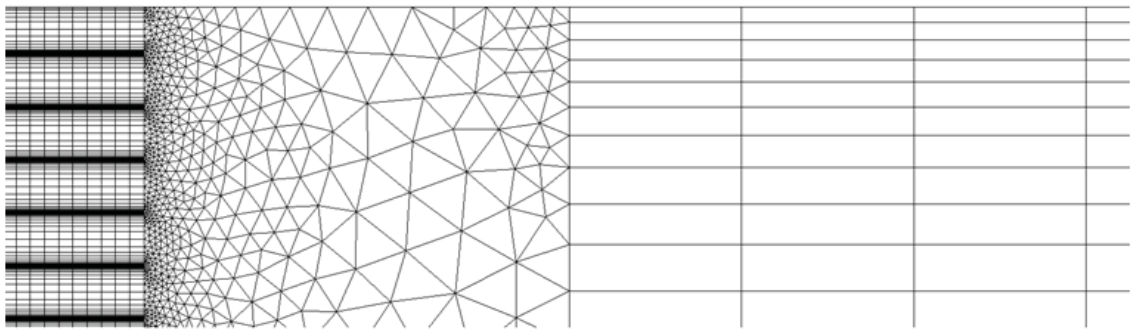

Figure 5.3: Mesh model for honeycomb, flame and downstream zones.

5.2.3 Problem setup

The flow condition of incoming methane-air mixture used for the simulation is the flow rate at 110cc/s and equivalence ratio of 0.75. The Reynolds number is calculated to be 122, indicating that the flow is laminar with very low Mach number. In order to perform a thorough and detailed simulation of the reacting flow problem, appropriate material properties, boundary conditions, chemical modeling and radiation modeling are defined and described.

1. Material properties

The properties of methane-air mixture are listed in Table 5.1 for equivalence ration of 0.75. The steel tube wall is not shown in the geometric model, but properties of steel are needed to simulate the heat transfer process. The honeycomb walls present in the model are made of ceramic, the properties of which are also provided in the table below.

Table 5.1: Material property summary for axisymmetric Rijke tube model.

Material		Fluid	Solid	
		Fuel-air mixture	Tube wall	Honeycomb
		methane and air	steel	ceramic
Density	kg/m^3	ideal gas	8030	2300
Specific Heat (c_p)	J/(kg·K)	mixing law	502.48	850.63
Thermal Conductivity	W/(m·K)	ideal gas mixing law	16.27	2.28
Viscosity	kg/(m·s)	ideal gas mixing law		
Mass Diffusivity	m^2/s	kinetic theory		
Thermal Diffusion Coeff.	kg/(m·s)	kinetic theory		

The methane-air mixture is treated as an ideal gas, and the calculation of properties are based on the ideal gas law. The density is computed as

$$\rho = \frac{p_{op} + p}{R_u T \sum_k \frac{Y_k}{W_k}} \quad , \tag{5.1}$$

where p_{op} denotes the operating pressure, ambient pressure in this case, and p the local gauge pressure predicted by ANSYS Fluent 14.0. R_u is the universal gas constant. Y_k and W_k are the mass fraction and the molecular weight of species k, respectively.

The specific heat is obtained using the general mixing law as

$$c_p = \sum_k Y_k c_{p,k} \tag{5.2}$$

with each individual specific heat for species k, $c_{p,k}$, defined by piecewise polynomials dependent on temperatures. The thermal conductivity and viscosity of the mixture are modeled in a similar manner by the ideal gas mixing law as

$$\lambda = \sum_k \frac{X_k \lambda_k}{\sum_j X_j \phi_{kj}} \quad , \tag{5.3}$$

$$\mu = \sum_k \frac{X_k \mu_k}{\sum_j X_j \phi_{kj}} \quad . \tag{5.4}$$

X_k denotes the mole fraction of species k , and

$$\phi_{kj} = \frac{\left[1 + \left(\frac{\mu_k}{\mu_j}\right)^{1/2} \left(\frac{W_j}{W_k}\right)^{1/4}\right]^2}{\left[8\left(1 + \frac{W_k}{W_j}\right)\right]^{1/2}} \quad . \tag{5.5}$$

The equivalent mass diffusion coefficient of species k into the mixture, $D_{k,m}$, is detrmined by the binary mass diffusion coefficient $\mathcal{D}_{kj}$, which is defined as

$$D_{kj} = 0.00188 \frac{\left[T^3 \left(\frac{1}{W_k} + \frac{1}{W_j}\right)\right]^{1/2}}{p_{abs} \sigma_{kj}^2 \Omega_D} \quad . \tag{5.6}$$

where p_{abs} stands for the absolute pressure, Ω_D denotes the diffusion collision integral measuring the interaction of the molecules, and σ_{kj} represents the arithmetic average of the individual Lennard-Jones parameters, σ_k and σ_j .

2. Boundary conditions

Table 5.2 shows the boundary conditions that have been used for this simulation. A uniform and steady fuel-air mixture flow is imposed on the inlet, performing as an acoustically closed boundary due to the fact that there are no velocity fluctuations. The mass flow rate of 1.27×10^{-4} kg/s is used, corresponding to the flow rate of 110 cc/s. At the outlet, it is assumed that the fuel is completely consumed, which is reasonable under the lean condition of equivalence ratio being 0.75. The convective heat transfer coefficient for the outside tube wall is estimated to be 20 W/(m^2·K), within the range of natural convection coefficient for air, i.e. 5-25 W/(m^2·K) [89].

Table 5.2: Boundary condition summary for axisymmetric Rijke tube model.

Inlet	Mass-flow-rate inlet	uniform and steady flow: 1.27×10^{-4} kg/s (Φ=0.75)
	Species Mass Fractions	CH_4: 0.04197; O_2:0.22323
	Total Temperature	ambient temperature: 293K
Outlet	Pressure Outlet	ambient pressure: 0Pa (gauge pressure)
	Species Mass Fractions	O2: 0.23292
Wall	Inside Tube Wall	coupled between the fluid flow and the inside steel wall
	Outside Tube Wall	convection coefficient: 20W/(m^2·K)
	Honeycomb Wall	coupled between the fluid flow and the solid honeycomb wall
Centerline	Axisymmetric Boundary	

3. Chemistry modeling

Both the global and two-step reaction mechanisms have been used to simulate this reacting flow problem. The results obtained by employing the two-step reaction mechanism show a better representation of this problem in terms of the temperature and heat of reaction distributions. However, the present work is focused on the sensitivity analysis of the poorly characterized boundary conditions. To maintain a reasonable complexity of the computation, only the global reaction mechanism is used for the sensitivity analysis.

The global reaction mechanism for methane and air is expressed as

$$CH_4 + 2\,(O_2 + 3.76N_2) \xrightarrow{K_G} CO_2 + 2H_2O + 7.52N_2 \ . \tag{5.7}$$

The rate of reaction of methane is modeled by the Arrhenius expression shown below:

$$\frac{d[CH_4]}{dt} = -A\exp\left(\frac{-E_a}{R_u T}\right)[CH_4]^m[O_2]^n \ , \tag{5.8}$$

where $[X_k]$ denotes the molar concentration of species k. The computation of the reaction rate for methane is critical to obtain the heat of reaction accurately. The values of parameters shown in Equation 5.8 are given in Table 5.3 [90].

Table 5.3: Parameters of Arrhenius expression for methane and air reaction.

Pre-exponential factor A $[(kmol/m^3)^{(1-m-n)}/s]$	Activation Temperature Ea/Ru [K]	m	n
2.119×10^{11}	24,379	0.2	1.3

4. Radiation modeling

A radiation model has been incorporated into the CFD simulations for the reacting flow to capture the heat field accurately. The discrete ordinates (DO) radiation model [91] has been chosen for the combustion-involved problem. The DO model solves the Radiative Transfer Equation (RTE) for a finite number of discrete angles, the number of which is controllable. Each angle is associated with a vector direction identified by the spatial coordinates. Spanning the entire range of optical thicknesses, the DO model becomes the best tool for representing radiation in combustion problems. Without knowing the optical thickness for this problem, it is appropriate to utilize the DO model to mitigate the errors for high and low optical thickness cases.

5.2.4 Solution technique

The difficulties in simulation of reacting flow primarily lie in two aspects. The first issue concerns the strong coupling effects in a flow system involving combustion. The species concentration affects the chemical reaction, which consequently influences the basic flow pattern significantly, leading to the interactions between the mass and momentum equations and the species transport equations. The second issue pertains to the disparate time scales discussed

previously. Especially for the combustion system with rapid reaction rates present, the disparate time scales make the computation of species transport equations numerically difficult and the system becomes "stiff".

A two-step solution technique has been used to overcome the convergence difficulties due to the strong effects that the combustion process has on the basic flow pattern. A cold flow is established by solving the flow, species and energy equations only. Then the volumetric reaction model is turned on and a temperature patch of 3000K is attached to the top of the honeycomb with a thickness of 2mm, which is of the same order of magnitude as the estimated flat flame thickness. A first-order implicit formulation in time is used and the time step size is set to $1\,\mu s$. The pressure-based Pressure-Implicit with Splitting of Operators (PISO) scheme, which improves the efficiency of the SIMPLE scheme by performing neighbor correction and skewness correction, together with stiff chemistry model has been applied to capture the flow and heat fields. Second order accurate schemes are used for the pressure, density, species and energy. The under-relaxation factor for density is reduced to 0.5. The under-relaxation factors for energy and discrete ordinates are initially set to 0.05 and 0.1, respectively, and are both increased gradually to 0.95.

5.3 Sensitivity formulation

CFD simulation results obtained from ANSYS Fluent 14.0 are imported into a sensitivity solver written in MATLAB. This sensitivity solver solves CSEs derived from a set of governing equations that represent the thermoacoustic problem in a Rijke tube.

5.3.1 Nondimensional sensitivity equations

5.3.1.1 Continuous Sensitivity Equations

The nondimensional forms of the governing equations in Section 3.1.1 are used to partially overcome the computational difficulty due to the disparate length and time scales. The reference values are defined by ambient conditions, initial flow conditions and characteristic dimensions of the problem studied. Let p_r ,T_r and ρ_r denote the reference pressure, temperature and density,

respectively. Let u_r, Y_r, W_r, $c_{p,r}$ and μ_r be the reference flow velocity, mass fraction, molecular weight, specific heat and dynamic viscosity, respectively. The radius of Rijke tube is chosen to be the characteristic length L. The reference Mach number is denoted by M_r. Consistent with the notation for the one-dimensional thermoacoustic problem in Chapter 4, the nondimensional variables are denoted by asterisks and defined as follows:

$$\begin{aligned}
&\vec{u}^* = \frac{\vec{u}}{u_r}, \quad t^* = \frac{u_r t}{L}, \quad \rho^* = \frac{\rho}{\rho_r}, \quad T^* = \frac{T}{T_r}, \quad W^* = \frac{W}{W_r} \\
&R_r = \frac{R_u}{W_r}, \quad p_r = \rho_r R_r T_r, \quad p^* = \frac{p - p_r}{\rho_r u_r^2}, \quad M_r = \frac{u_r}{\sqrt{\gamma R_r T_r}} \quad . \\
&\mu^* = \frac{\mu}{\mu_r}, \quad c_p^* = \frac{c_p}{c_{p,r}}, \quad Y^* = \frac{Y}{Y_r}, \quad \dot{w}_k^* = \frac{L\dot{w}_k}{u_r \rho_r Y_r}, \quad h_{s,k}^* = \frac{Y_r h_{s,k}}{c_{p,r} T_r}
\end{aligned} \tag{5.9}$$

The following nondimensional numbers are also used in the development of nondimensional equations. The Reynolds number appearing in the equations is based on reference values, and remains constant for the entire computational process. Estimates for the Prandtl number and Lewis numbers refer to constant values used by Pantano [92] for a direct simulation of a methane-air jet, as shown in Table 5.4. The Schmidt number for species k is computed as the product of Prandtl and Lewis numbers for species k.

$$Re = \frac{\rho_r u_r L}{\mu_r}, \quad Pr = \frac{\mu c_p}{\lambda}, \quad Sc_k = PrLe_k \ . \tag{5.10}$$

Table 5.4: Estimates of nondimensional numbers for methane and air reaction [92].

Pr	Le				
	CH_4	O_2	CO_2	H_2O	N_2
0.70	0.97	1.11	1.39	0.83	1.00

An additional assumption is that the specific heat ratio is a constant throughout the domain, i.e. $\gamma = c_p / c_v = 1.4$. Some useful relations are also derived as follows:

$$c_p^* = \frac{1}{W^*} \ , \tag{5.11}$$

$$\rho_r u_r^2 = \gamma p_r M_r^2 \ . \tag{5.12}$$

Equation 5.11 is employed for deriving the nondimensional form of the heat diffusion term in the energy equation. Equation 5.12 is used for the pressure work term in the energy equation. Derivatives of the set of nondimensional sensitivity equations are taken with respect to nondimensional parameters. In the present work, the influential factors are the equivalence ratio, ϕ, at the Rijke tube inlet, and the nondimensional mass flux, g^*_{inlet}, which is related to the inlet mass flow rate $\dot{m}_{inlet}$ by

$$g^*_{inlet} = \left(\rho^* u^*\right)_{inlet} = \frac{\left(\dfrac{\dot{m}_{inlet}}{A_{inlet}}\right)}{\rho_r u_r} \quad . \tag{5.13}$$

The mass flow rate at the inlet, $\dot{m}_{inlet}$, is assumed to be uniform for the apparatus studied. A_{inlet} is the cross-section area which is constant throughout the tube length.

Differentiating the governing equations with respect to a selected influential parameter, and rearranging terms yield the following set of CSEs:

$$\frac{\partial s_{\rho^*}}{\partial t^*} + \nabla \cdot (s_{\rho^* \vec{u}^*}) = 0 \tag{5.14}$$

$$\frac{\partial}{\partial t^*}\left(s_{\rho^* Y_k^*}\right) + \nabla \cdot \left(s_{\rho^* \vec{u}^* Y_k^*}\right) = \frac{1}{Re}\nabla \cdot \left(\frac{1}{Sc_k} s_{\mu^* \nabla Y_k^*}\right) + s_{\dot{w}_k^*} \tag{5.15}$$

$$\frac{\partial}{\partial t^*}\left(s_{\rho^* \vec{u}^*}\right) + \nabla \cdot \left(s_{\rho^* \vec{u}^* \vec{u}^*}\right) = -\nabla s_{p^*} + \frac{1}{Re}\nabla \cdot s_{\tau^*} \tag{5.16}$$

$$\begin{aligned} & s_{c_p^*}\left[\frac{\partial}{\partial t^*}\left(\rho^* T^*\right) + \nabla \cdot \left(\rho^* T^* \vec{u}^*\right)\right] + c_p^*\left[\frac{\partial}{\partial t^*}\left(s_{\rho^* T^*}\right) + \nabla \cdot \left(s_{\rho^* T^* \vec{u}^*}\right)\right] \\ & = s_{\dot{w}^*_{T,c_p}} + \left(\gamma - 1\right) M_r^2 \frac{Ds_{p^*}}{Dt^*} + \frac{1}{RePr}\nabla \cdot \left(s_{\frac{\mu^*}{W^*}\nabla T^*}\right) + \frac{1}{Re} s_{\left(\sum_{i=1}^{N} c_{p,k}^* \frac{\mu^*}{Sc_k}\nabla Y_k^*\right)\cdot \nabla T^*} + \frac{\gamma - 1}{Re} M_r^2 s_{\tau^* : \nabla \vec{u}^*} \end{aligned} \tag{5.17}$$

$$\gamma M_r^2 s_{p^*} = s_{\frac{\rho^* T^*}{W^*}} \tag{5.18}$$

It is noted that the equation for temperature in terms of c_p is adopted. The term $s_{\dot{w}^*_{T,c_p}}$ in Equation 5.17 denotes the sensitivity of the heat release rate due to reactions. It is calculated by the enthalpy of species h_k^* and the reaction rate $\dot{w}_k^*$ as:

$$s_{\dot{w}^*_{T,c_p}} = -\sum_{k=1}^{N} s_{h_k \cdot \dot{w}_k} \quad . \tag{5.19}$$

The reaction rate $\dot{w}_k^*$ is obtained from Equation 5.8.

The present scaling of pressure distinguishes this nondimensionalization approach from others. Instead of using the absolute value of pressure, the pressure difference is nondimensionalized, which is the driving force of the flow and usually adopted for incompressible flow. The merits of this approach are demonstrated by Hou and Mahesh [93]. They showed that the NS equations in this nondimensional form converge to incompressible equations as the Mach number approaches zero, therefore this nondimensionalization is suitable for both high Mach number problems to capture shock waves and low Mach number problems to resolve variations occurring on a time scale appropriate for acoustics. This is crucial to sensitivity calculations. Suppose we use the traditional nondimensional method for pressure, $p^* = \frac{p}{p_r} = \frac{p}{\rho_r R_r T_r}$, it is easy to show that there will be a coefficient in the order of $1/M_r^2$ for the pressure gradient term in the momentum equation and other terms in the energy equation. This coefficient suggests that for very low Mach number problems, small numerical errors could be enlarged by a big factor of $1/M_r^2$, leading to numerical instabilities that are mistaken for system instabilities. Accordingly, computed sensitivities will also convey undesirable information of numerical noise. Following Hou and Mahesh's work, Doom [94] extended this nondimensional form for reacting flow simulations, which provided good results for validation purposes.

5.3.1.2 Boundary conditions

As the most important element for the present work, derivatives of boundary conditions are also taken with respect to the same selected nondimensional parameters, i.e. the magnitude of inlet mass flux g_{inlet}^* and the equivalence ratio ϕ.

1. Sensitivity boundary condition with respect to g_{inlet}^*

The inlet mass flow rate is considered to be uniform and in the axial direction of the tube. Thus, the sensitivity of the axial mass flux boundary with respect to g_{inlet}^* is

$$s_{g_{x,bc}^*} = \frac{\partial g_{x,bc}^*}{\partial g_{inlet}^*} = 1 \ . \tag{5.20}$$

The inlet temperature boundary is computed from the total temperature T_{tot} by the following equations under the assumption of a constant specific heat ratio γ. Equations 5.21 and 5.22 in dimensional form are used to compute the sensitivity boundary condition for temperature which is nondimensionalized when applied in the solver.

$$\frac{T_{tot}}{T} = 1 + \frac{\gamma - 1}{2} M^2 \tag{5.21}$$

$$M \equiv \frac{u}{c} = \frac{u}{\sqrt{\gamma R T}} \tag{5.22}$$

M is Mach number, and c is the speed of sound. The total temperature T_{tot} is set at the ambient temperature of 293K, and T is the static temperature to be determined. Together with the equation of state, solving Equations 5.21 and 5.22 for T in dimensional form gives

$$T_{tot} = T + \frac{\gamma - 1}{2\gamma} g^2 R \frac{T^2}{p^2} \quad . \tag{5.23}$$

Taking the derivative for both sides of Equation 5.23 with respect to g_{inlet} yields

$$0 = s_T + \frac{\gamma - 1}{\gamma} R \left(\frac{g^2 T}{p^2} s_T + \frac{g T^2}{p^2} s_g - \frac{g^2 T^2}{p^3} s_p \right) . \tag{5.24}$$

Solving Equation 5.24 and evaluating variables at the inlet yields the boundary condition for sensitivity of temperature s_T:

$$s_T \Big|_{inlet} = \left. \frac{-\frac{\gamma - 1}{\gamma} R \left(\frac{g T^2}{p^2} s_g - \frac{g^2 T^2}{p^3} s_p \right)}{1 + \frac{\gamma - 1}{\gamma} R \frac{g^2 T}{p^2}} \right|_{inlet} , \tag{5.25}$$

where s_g is 1 at the inlet boundary based on Equation 5.20. The obtained s_T is then nondimensionalized using the following relationship:

$$s_{T^*} = \frac{\partial T^*}{\partial g^*} = \frac{\rho_r u_r}{T_r} \frac{\partial T}{\partial g} = \frac{\rho_r u_r}{T_r} s_T \quad . \tag{5.26}$$

2. Sensitivity boundary condition with respect to ϕ

The inlet boundary values for mass fractions of species (reactants), gas constant, molecular weight and temperature all depend on the equivalence ratio ϕ.

First define two constants used in the formulation, the ratio of molecular weights of CH_4 and air C_1 and the mass fraction of O_2 in air C_2. At the inlet, the methane-air mixture enters the computational domain. Assuming the air only consists of O_2 and N_2, the mass fractions of reactants CO_2 and H_2O are zeros all the time resulting zero sensitivities to the equivalence ratio ϕ. The sensitivities of the mass fractions for the main species involved can be obtained by the following equations:

$$s_{Y_{\mathrm{CH_4}}^*} = \frac{1}{Y_r} \frac{1}{\left(1+\frac{9.52}{C_1\phi}\right)^2} \frac{9.52}{C_1\phi^2} \ , \tag{5.27}$$

$$s_{Y_{\mathrm{O_2}}^*} = -\frac{9.52 C_1 C_2}{Y_r} \frac{1}{\left(C_1\phi+9.52\right)^2} \ , \tag{5.28}$$

$$s_{Y_{N_2}^*} = -s_{Y_{\mathrm{CH_4}}^*} - s_{Y_{\mathrm{O_2}}^*} \tag{5.29}$$

The sensitivity of temperature with respect to ϕ also utilizes the dimensional form of Equation 5.23 first and is nondimensionalized before it is incorporated in the computation. The final expression for s_{T^*} is

$$s_{T^*} = \frac{1}{T_r} \frac{-\frac{\gamma-1}{2\gamma} g_{inlet}{}^2 \left(\frac{T^2}{p^2} s_R - 2R\frac{T^2}{p^3} s_p\right)}{1+\frac{\gamma-1}{\gamma} g_{inlet}{}^2 \frac{R}{p^2} T} \ , \tag{5.30}$$

where $s_R = -\frac{R_u}{W^2} s_W$ and $s_W = -W^2 \left(\sum_{k=1}^{N} \frac{s_{Y_k}}{W_k}\right)$ are both dimensional.

Sensitivity boundary conditions of density with respect to both parameters are acquired from the equation of state with computed sensitivities of pressure and temperature at the inlet. The remaining physical sensitivity boundary conditions are listed in Table 5.5.

It should be mentioned that the impedance boundary condition is a better choice for the outlet, but this information is not available for the Rijke tube studied. In addition to physical boundary conditions, the numerical boundary conditions are also defined as the Neumann-boundary-condition type for all variables, resulting in a well-defined problem to be solved.

Table 5.5: Sensitivity boundary condition summary for axisymmetric Rijke tube model.

Zone	Type	Sensitivity to g	Sensitivity to Φ
Inlet	Mass-flow-rate Inlet (g)	1	0 [kg/(m^{2}s)]
	Species Mass Fractions	0 [m^{2}s/kg]	Eqs.(5.27-5.29)
	Static Temperature	Eq.(5.25) [K·m^{2}s/kg]	Eq.(5.30) [K]
Outlet	Pressure Outlet	0 [Pa·m^{2}s/kg]	0 [Pa]
Wall	Non-slip Wall	0 [m^3/kg]	0[m/s]
Centerline	Axisymmetric Boundary		

5.3.2 Numerical method

The CSEs are linear at any specific time. A solver for linear equations given in matrix form could be used for solving the system of CSEs. The present research employs an iterative scheme instead. Since the CSEs are derived directly from the governing equations for the CFD problems, these two sets of systems of equations share the same structure which implies that the same solver can be used for both. This feature enables the synchronous computation of two sets of equations at one time step. Although the CFD results are imported from ANSYS Fluent 14.0 for this study, the iterative solver developed and described in Section 5.3.2.2 can be used to solve the system of governing equations for thermoacoustic problems and validate the results against those from the commercial software, proving the fidelity of the proposed numerical method. In addition, separate calculation of each equation in the iterative solver is more flexible if a more complex mechanism is used or modification of equations is needed.

Since complete CFD simulation results are obtained first in the present study, information about the acoustic signal can be extracted and utilized to simplify the sensitivity calculation. The frequency of the primary acoustic mode that has been excited turns out to be 168.8Hz (will be shown in Section 5.4.1). The time step size used for CFD simulation is 1 μs , and data are saved every 500 time steps. This sampling frequency of 2000Hz is greater than the minimum determined by the sampling theory, leading to a representative data set for sensitivity analysis.

The discretization and numerical method discussed in the following sections are based on a uniform gird. The proposed scheme can be extended to a non-uniform grid, which is beyond the

scope of this study. The CFD data obtained from the non-uniform grid shown in Section 5.2.2 are mapped onto a uniform grid for the sensitivity calculation. Both CFD data and sensitivity data are located at the cell center. To facilitate the mapping process, the computational domain is partitioned into several bins according to the arrangement of four CFD zones described previously and the size of sensitivity cells. Each bin contains a number of uniform sensitivity cells, and each sensitivity cell encloses a finite number of CFD data for each primary variable. CFD data are distributed into each bin, and finally into a particular sensitivity cell based on the global coordinates. The values of variables at the center of a sensitivity cell are interpolated using the inverse distance weighting method:

$$\bar{Q} = \begin{cases} \dfrac{\sum_{i=1}^{N} \dfrac{1}{d_i^2} Q_i}{\sum_{i=1}^{N} \dfrac{1}{d_i^2}}, & d_i \neq 0 \text{ for all } i \\ Q_i, & d_i = 0 \text{ for some } i \end{cases}, \tag{5.31}$$

where $\bar{Q}$ denotes the interpolated value in a sensitivity cell, and Q_i represents the CFD data inside the specified sensitivity cell. d_i is the distance between the center of the targeted sensitivity cell and the center of a CFD cell where Q_i is located. N is the total number of data points in the sensitivity cell.

5.3.2.1 Discretization

The discretization approach is illustrated in Figure 5.4. The positions of variables show that the vector variables, i.e. u and v (correspondingly g_x and g_y), are directly evaluated on the surfaces of cell volumes, and staggered spatially by one half of a grid point relative to the scalar variables, i.e. ρ, p and T, that are located at the cell centers. The superscripts indicate the time level for variables. It is noted that the scalar variables lead the vector variables by one half of a time step size. At each time step denoted by n, the vector variables at t^n are updated to t^{n+1}, and the scalar variables at $t^{n+\frac{1}{2}}$ are advanced to $t^{n+\frac{3}{2}}$. As a result, the scheme is staggered not only in space, but also in time. Pierce [95] has applied this staggered grid scheme to simulations of transient reacting flows, which improved the accuracy and stability of the discretized continuity equation. Wall *et al*. [96] adopted the formulation by Pierce, but modified the pressure terms in

the momentum and energy equations by interpolating the pressure twice in time, instead of using the pressure at the current time level, $t^{n+\frac{1}{2}}$, directly. Therefore, the pressure is weighted by the values at consecutive times:

$$\overline{p}^{t} = \frac{1}{4}\left(p^{n-\frac{1}{2}} + 2p^{n+\frac{1}{2}} + p^{n+\frac{3}{2}} \right) . \tag{5.32}$$

The bar over the variable p denotes the interpolation operator, and t besides the bar indicates that interpolation is taken in time. This implicit representation of pressure terms intends to eliminate the acoustic CFL requirement [97]. However, the thermoacoustic phenomenon in reacting flows involves chemical reactions that usually have smaller time scales than acoustic CFL requirement. Capturing the reacting process requires smaller time step sizes which impact the computational time.

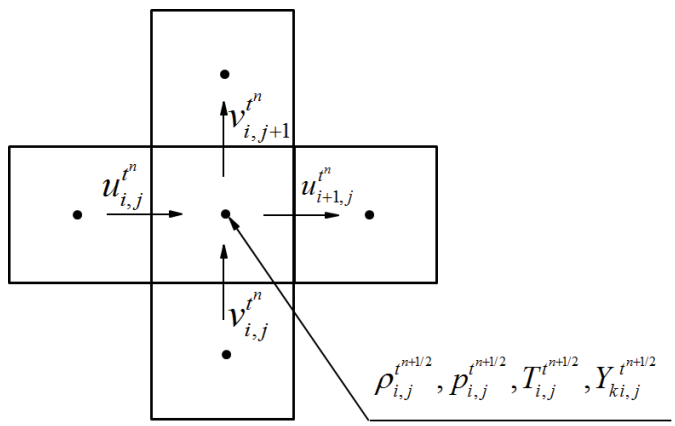

Figure 5.4: Five-point stencil for two-dimensional numerical simulation.

Since the grid is staggered in space, spatial interpolation is required to locate all the terms in a specific sensitivity equation at the same point. The notation for the spatial interpolation is an overbar with the specified interpolation direction. It should be noted that the indices for interpolation operators do not obey the Einstein summation convention. Following the difference operators in Section 4.3.1 and the notation for the mass flux, i.e. g, in Section 4.3.2, discretizing Equations 5.14-5.17 yields the following equations:

$$\frac{\left(s_{\rho^*}\right)^{n+\frac{3}{2}} - \left(s_{\rho^*}\right)^{n+\frac{1}{2}}}{\Delta t^*} + \delta_{x_i}\left(s_{g_i^*}\right)^{n+1} = 0 \ , \tag{5.33}$$

$$\frac{\left(s_{\rho^* Y_k^*}\right)^{n+\frac{3}{2}} - \left(s_{\rho^* Y_k^*}\right)^{n+\frac{1}{2}}}{\Delta t^*} + \delta_{x_i}\left(s_{\overline{\rho^* Y_k^*}^{x_i} u_i^*}\right)^{n+1} = \frac{1}{Re}\delta_{x_i}\left(\frac{1}{Sc_k} s_{\overline{\mu^*}^{x_i}\delta_{x_i}\left(Y_k^*\right)}\right)^{n+1} + s_{\dot{w}_k^*}{}^{n+1}, \tag{5.34}$$

$$\frac{\left(s_{g_j^*}\right)^{n+1} - \left(s_{g_j^*}\right)^{n}}{\Delta t^*} + \delta_{x_i}\left(s_{\overline{g_j^*}^{x_i}\overline{u_i^*}^{x_j}}\right)^{n+\frac{1}{2}} = -\delta_{x_j}\left(s_{\overline{p^*}^{t}}\right)^{n+\frac{1}{2}} + \frac{1}{Re}\delta_{x_i}\left(s_{\tau_{ij}^*}\right)^{n+\frac{1}{2}}, \tag{5.35}$$

$$s_{c_p^*}{}^{n+1}\left[\frac{\left(\rho^* T^*\right)^{n+\frac{3}{2}} - \left(\rho^* T^*\right)^{n+\frac{1}{2}}}{\Delta t^*} + \delta_{x_i}\left(\rho^* T^* u_i^*\right)^{n+1}\right] + c_p^{*n+1}\left[\frac{\left(s_{\rho^* T^*}\right)^{n+\frac{3}{2}} - \left(s_{\rho^* T^*}\right)^{n+\frac{1}{2}}}{\Delta t^*} + \delta_{x_i}\left(s_{\overline{\rho^* T^*}^{x_i} u_i^*}\right)^{n+1}\right]$$

$$= s_{\dot{w}_{T,x_p}^*}{}^{n+1} + \left(\gamma - 1\right) M_r^{\,2}\left[\frac{\left(s_{p^*}\right)^{n+\frac{3}{2}} - \left(s_{p^*}\right)^{n+\frac{1}{2}}}{\Delta t^*} + \overline{u_i^*}^{x_i\,n+1}\delta_{x_i}\left(s_{\overline{p^*}^{x_i}}^{t}\right)^{n+1}\right]$$

$$+ \frac{1}{RePr}\delta_{x_i}\left[s_{\overline{\left(\frac{\mu^*}{W^*}\right)}^{x_i}\delta_{x_i}\left(T^*\right)}\right]^{n+1} + \frac{1}{Re} s_{\left[\sum_{k=1}^{N} c_{p,k}{}^* \frac{\mu^*}{Sc_k}\delta_{x_i}\left(\overline{Y_k^*}^{x_i}\right)\right]\cdot\delta_{x_i}\left(\overline{T^*}^{x_i}\right)}{}^{n+1} + \frac{\gamma - 1}{Re} M_r^{\,2} s_{\tau_{ij}^*\delta_{x_j}\left(u_i^*\right)}{}^{n+1} \tag{5.36}$$

The viscous tensor shown in the sensitivity equation for momentum differs from that in the sensitivity equation for temperature in the form of interpolation. For Equation 5.35,

$$\tau_{ij}^* = \begin{cases} \overline{\overline{\mu^*}^{x_i}}^{x_j}\left[\delta_{x_j}\left(u_i^*\right) + \delta_{x_i}\left(u_j^*\right)\right]^{n+\frac{1}{2}}, & i \neq j \\ \mu^*\left[\delta_{x_j}\left(u_i^*\right) + \delta_{x_i}\left(u_j^*\right) - \frac{2}{3}\delta_{x_k}\left(u_k^*\right)\right]^{n+\frac{1}{2}}, & i = j \end{cases}. \tag{5.37}$$

For the viscous heating term in Equation 5.36,

$$\tau_{ij}^*\delta_{x_j}\left(u_i^*\right) = \begin{cases} \mu^*\left[\delta_{x_j}\left(\overline{\overline{u_i^*}^{x_i}}^{x_j}\right) + \delta_{x_i}\left(\overline{\overline{u_j^*}^{x_i}}^{x_j}\right)\right]^{n+1}\delta_{x_j}\left(\overline{\overline{u_i^*}^{x_i}}^{x_j}\right)^{n+1}, & i \neq j \\ \mu^*\left[\delta_{x_j}\left(u_i^*\right) + \delta_{x_i}\left(u_j^*\right) - \frac{2}{3}\delta_{x_k}\left(u_k^*\right)\right]^{n+1}\delta_{x_j}\left(u_i^*\right)^{n+1}, & i = j \end{cases}. \tag{5.38}$$

An important feature of the centered discretization for the continuity equation and the pressure gradient term in the momentum equation is zero dissipation of acoustic waves, which is desirable for thermoacoustic problems. Wall *et al*. [96] demonstrated this feature by applying the proposed discretization method to a linear acoustics problem.

5.3.2.2 Pressure-correction method

Similar to the pressure-correction method for incompressible flows, an iterative algorithm for compressible flows was proposed by Wall *et al*. [96] using the idea of classic pressure-correction methods. They applied this algorithm to a series of problems from linear acoustics to the LES of channel flows. A one-dimensional combustor was also simulated to assess this algorithm for low-frequency acoustics occurred in gas turbine combustors, but the combustion process was replaced by steady heat input. The results of these tested problems showed excellent stability properties of the proposed algorithm. The present research extends this algorithm to include the species transport equation and heat of reaction in the energy equation, actually modeling the combustion process and the interaction of flame with the flow. The extended algorithm is capable of solving both the system of governing equations and the system of CSEs. Since CFD simulations are conducted using ANSYS Fluent 14.0, only the execution of this algorithm for CSEs is described below. Within each time step, equilibrium iterations are performed to advance the sensitivity variables from the current time level to the next. The superscripts of variables, n and m, denote the time step and the iteration number, respectively. The standard steps for executing the extended algorithm are:

Within each time step:

1. Initialize the sensitivity variables.

The values of sensitivity variables at the current time step are taken as initial guesses for the values at the next time step:

$$u_j^{*n+1,0} = u_j^{*n}, \quad p^{*n+\frac{3}{2},0} = p^{*n+\frac{1}{2}}, \quad \rho^{*n+\frac{3}{2},0} = \rho^{*n+\frac{1}{2}}, \quad T^{*n+\frac{3}{2},0} = T^{*n+\frac{1}{2}}. \tag{5.39}$$

The values of primary variables shown in the discretized sensitivity equations at the next time step are obtained from CFD simulations. As the coefficients of sensitivity variables, the primary variables and the terms expressed by primary variables are known prior to the update of sensitivity variables and remain constant during the equilibrium iterations within one time step.

2. Advance the sensitivity of temperature.

The equation for sensitivity of temperature is employed. The term representing the sensitivity of heat release rate due to chemical reaction is calculated in the intermediate step, playing a critical role in the sensitivity of the Rayleigh index. Let R denote the generic term by subtracting

the first term of the left-hand side from the right-hand side of Equation 5.36. $s_{\rho^* T^*}$ is first advanced as a whole:

$$\left(s_{\rho^* T^*}\right)^{n+\frac{3}{2},m+1} = \left(s_{\rho^* T^*}\right)^{n+\frac{1}{2}} + \Delta t^* \left[\frac{1}{c_p^{*n+1}} R - \delta_{x_i} \left(s_{\overline{\rho^* T^*}^{x_i} u_i^*} \right)^{n+1} \right], \tag{5.40}$$

where $s_{\overline{\rho^* T^*}^{x_i} u_i^*} = s_{\overline{\rho^* T^*}^{x_i}} u_i^* + \overline{\rho^* T^*}^{x_i} s_{u_i^*}$ by the chain rule, and

$$s_{\overline{\rho^* T^*}^{x_i}}^{n+1} = \frac{1}{2} \left(s_{\overline{\rho^* T^*}^{x_i}}^{n+\frac{1}{2}} + s_{\overline{\rho^* T^*}^{x_i}}^{n+\frac{3}{2},m+1} \right). \tag{5.41}$$

It is noted that the convection term also includes $s_{\rho^* T^*}$ for the new equilibrium iteration, i.e. $s_{\overline{\rho^* T^*}^{x_i}}^{n+\frac{3}{2},m+1}$, which requires spatial interpolations of $\left(s_{\rho^* T^*}\right)^{n+\frac{3}{2},m+1}$. The sensitivity of temperature is then computed by the following relationship associated with $\left(s_{\rho^* T^*}\right)^{n+\frac{3}{2},m+1}$ and the sensitivity of density for the current equilibrium iteration:

$$s_{T^*}^{n+\frac{3}{2},m+1} = \frac{\left(s_{\rho^* T^*}\right)^{n+\frac{3}{2},m+1} - s_{\rho^*}^{n+\frac{3}{2},m} T^{*n+\frac{3}{2}}}{\rho^{*n+\frac{3}{2}}}. \tag{5.42}$$

3. Advance the sensitivity of species mass fraction.

The sensitivity of species mass fraction is advanced by solving Equation 5.34:

$$\left(s_{\rho^* Y_k^*}\right)^{n+\frac{3}{2},m+1} = \left(s_{\rho^* Y_k^*}\right)^{n+\frac{1}{2}} + \Delta t^* \left[\frac{1}{Re} \delta_{x_i} \left(\frac{1}{Sc_k} s_{\overline{\mu^*}^{x_i} \delta_{x_i}\left(Y_k^*\right)} \right)^{n+1} + s_{\dot{w}_k^*}^{n+1} - \delta_{x_i} \left(s_{\overline{\rho^* Y_k^*}^{x_i} u_i^*} \right)^{n+1} \right]. \tag{5.43}$$

In the above expression, not only the convection term is interpolated by the unknown $\left(s_{\rho^* Y_k^*}\right)^{n+\frac{3}{2},m+1}$, the sensitivity of heat release rate is also computed implicitly:

$$s_{\dot{w}_k^*}^{n+1} = \frac{1}{2} \left(s_{\dot{w}_k^*}^{n+\frac{1}{2}} + s_{\dot{w}_k^*}^{n+\frac{3}{2}} \right), \tag{5.44}$$

where $s_{\dot{w}_k^*}^{n+\frac{3}{2}} = s_{W_k^* [X_k]^* / dt^*}^{n+\frac{3}{2}} = \left(s_{W_k^*} \left[X_k \right]^* / dt^* + W_k^* s_{[X_k]^* / dt^*} \right)^{n+\frac{3}{2}}$.

For methane, $\frac{[\mathrm{CH_4}]^*}{dt^*}$ is a function of $[\mathrm{CH_4}]^*$ and $[\mathrm{O_2}]^*$ as shown in Equation 5.10, and $[\mathrm{CH_4}]^* = \frac{\rho Y_{\mathrm{CH_4}}}{W_{\mathrm{CH_4}}}$ and $[\mathrm{O_2}]^* = \frac{\rho Y_{\mathrm{O_2}}}{W_{\mathrm{O_2}}}$. For other species in the reaction, $\frac{[X_k]^*}{dt^*}$ is a multiple of $\frac{[\mathrm{CH_4}]^*}{dt^*}$. Therefore, the sensitivity of heat release rate, i.e. $s_{\dot{w}_k^*}{}^{n+1}$, also involves the unknown $\left(s_{\rho^* Y_k^*}\right)^{n+\frac{3}{2},m+1}$. An inner loop is employed to solve for $\left(s_{\rho^* Y_k^*}\right)^{n+\frac{3}{2},m+1}$ for species $\mathrm{CH_4}$, $\mathrm{O_2}$ and $\mathrm{CO_2}$. $\left(s_{Y_k^*}\right)^{n+\frac{3}{2},m+1}$ is obtained by dividing by the sensitivity of density for the current equilibrium iteration:

$$s_{Y_k^*}{}^{n+\frac{3}{2},m+1} = \frac{\left(s_{\rho^* Y_k^*}\right)^{n+\frac{3}{2},m+1} - s_{\rho^*}{}^{n+\frac{3}{2},m} Y_k^{*n+\frac{3}{2}}}{\rho^{*n+\frac{3}{2}}}. \tag{5.45}$$

The sensitivity of mass faction for $s_{Y_{\mathrm{N_2}}^*}$ is calculated as follows:

$$s_{Y_{\mathrm{N_2}}^*}{}^{n+\frac{3}{2},m+1} = -s_{Y_{\mathrm{CH_4}}^*}{}^{n+\frac{3}{2},+1m} - s_{Y_{\mathrm{O_2}}^*}{}^{n+\frac{3}{2},m+1} - s_{Y_{\mathrm{CO_2}}^*}{}^{n+\frac{3}{2},m+1}. \tag{5.46}$$

4. Predict the sensitivity of density.

With obtained $\left(s_{T^*}\right)^{n+\frac{3}{2},m+1}$ and $\left(s_{Y_k^*}\right)^{n+\frac{3}{2},m+1}$, the sensitivity of density is updated using Equation 5.18:

$$\tilde{s}_{\rho^*}{}^{n+\frac{3}{2},m+1} = \left(\frac{W^*}{T^*}\right)^{n+\frac{3}{2},m+1} \left[\gamma M_r{}^2 s_{p^*}{}^{n+\frac{3}{2},m} - \left(\frac{\rho^*}{W^*} s_{T^*}\right)^{n+\frac{3}{2},m+1} - \left(\rho^* T^* \sum_{k=1}^{N} \frac{s_{Y_k^*}}{W_k^*}\right)^{n+\frac{3}{2},m+1}\right]. \tag{5.47}$$

A tilde over s_{ρ^*} indicates that the sensitivity of density is an intermediate prediction because the sensitivity of pressure used is still within the current equilibrium iteration.

5. Advance the sensitivity of mass flux.

This step predicts the sensitivity of mass flux using the current estimate of sensitivity of pressure $s_{p^*}^{n+\frac{3}{2},m}$. The predicted sensitivity is marked by a tilde and will be corrected by the equation for sensitivity of pressure. Solving Equation 5.35 yields:

$$\begin{aligned}\left(\tilde{s}_{g_j^*}\right)^{n+1,m+1} &= \left(s_{g_j^*}\right)^{n} + \Delta t^* \left[-\delta_{x_j} \left(\frac{1}{4} s_{p^*}^{n-\frac{1}{2}} + \frac{1}{2} s_{p^*}^{n+\frac{1}{2}} + \frac{1}{4} s_{p^*}^{n+\frac{3}{2},m} \right) \right] \\ &\quad + \Delta t^* \left[\frac{1}{Re} \delta_{x_i} \left(s_{\tau_{ij}^*} \right)^{n+\frac{1}{2}} - \delta_{x_i} \left(s_{\overline{g_j^*}^{x_i} \overline{u_i^*}^{x_j}} \right)^{n+\frac{1}{2}} \right]\end{aligned} . \tag{5.48}$$

6. Compute the correction to the sensitivity of pressure.

Adding corrections to $\left(\tilde{s}_{g_j^*}\right)^{n+1,m+1}$ and $s_{p^*}^{n+\frac{3}{2},m}$ leads to the following expressions for the sensitivity of mass flux and the sensitivity of pressure at the equilibrium iteration, respectively:

$$s_{g_j^*}^{n+1,m+1} = s_{\tilde{g}_j^*}^{n+1,m+1} + \Delta s_{g_j^*} , \tag{5.49}$$

$$s_{p^*}^{n+\frac{3}{2},m+1} = s_{p^*}^{n+\frac{3}{2},m} + \Delta s_{p^*} . \tag{5.50}$$

Substituting the above expressions into Equation 5.35 and rearranging terms yield:

$$\begin{aligned}\left(\tilde{s}_{g_j^*}\right)^{n+1,m+1} + \Delta s_{g_j^*} &= \left(s_{g_j^*}\right)^{n} + \Delta t^* \left[-\delta_{x_j} \left(\frac{1}{4} s_{p^*}^{n-\frac{1}{2}} + \frac{1}{2} s_{p^*}^{n+\frac{1}{2}} + \frac{1}{4} s_{p^*}^{n+\frac{3}{2},m} + \frac{1}{4} \Delta s_{p^*} \right) \right] \\ &\quad + \Delta t^* \left[\frac{1}{Re} \delta_{x_i} \left(s_{\tau_{ij}^*} \right)^{n+\frac{1}{2}} - \delta_{x_i} \left(s_{\overline{g_j^*}^{x_i} \overline{u_i^*}^{x_j}} \right)^{n+\frac{1}{2}} \right]\end{aligned} . \tag{5.51}$$

Subtracting Equation 5.48 from Equation 5.51 results in the equation for correctors:

$$\Delta s_{g_j^*} = -\frac{1}{4} \Delta t^* \left[\delta_{x_j} \left(\Delta s_{p^*} \right) \right] . \tag{5.52}$$

A Poisson equation for the sensitivity of pressure is obtained by taking the divergence of Equation 5.52 and using the expression for $\Delta s_{g_j^*}$ in Equation 5.49:

$$\delta_{x_j} \left[\delta_{x_j} \left(\Delta s_{p^*} \right) \right] = -\frac{4}{\Delta t^*} \delta_{x_j} \left(s_{g_j^*}^{n+1,m+1} - \tilde{s}_{g_j^*}^{n+1,m+1} \right) . \tag{5.53}$$

Enforcing Equation 5.33 for the term $\delta_{x_j} \left(s_{g_j^*}^{n+1,m+1} \right)$ in the above equation at t^{n+1} yields:

$$\delta_{x_j}\left[\delta_{x_j}\left(\Delta s_{p^*}\right)\right]=\frac{4}{\Delta t^*}\left[\delta_{x_j}\left(\tilde{s}_{g_j^*}{}^{n+1,m+1}\right)+\frac{\left(s_{\rho^*}\right)^{n+\frac{3}{2}}-\left(s_{\rho^*}\right)^{n+\frac{1}{2}}}{\Delta t^*}\right]. \tag{5.54}$$

The sensitivity of density at the next time step, $\left(s_{\rho^*}\right)^{n+\frac{3}{2}}$, is approximated by the Taylor expansion about $\tilde{s}_{\rho^*}{}^{n+\frac{3}{2},m+1}$, which is known from Step 4:

$$\left(s_{\rho^*}\right)^{n+\frac{3}{2}}\approx\tilde{s}_{\rho^*}{}^{n+\frac{3}{2},m+1}+\left.\frac{\partial s_{\rho^*}}{\partial s_{p^*}}\right|_{s_{T^*},s_{Y_k^*}}\Delta s_{p^*}. \tag{5.55}$$

Since s_{T^*} and $s_{Y_k^*}$ are constant within a specific equilibrium iteration, i.e. $s_{T^*}{}^{n+\frac{3}{2},m+1}$ and $s_{Y_k^*}{}^{n+\frac{3}{2},m+1}$, the derivative of the sensitivity of density with respect to the sensitivity of pressure has the following form:

$$\left.\frac{\partial s_{\rho^*}}{\partial s_{p^*}}\right|_{s_{T^*},s_{Y_k^*}}=\left(\frac{W^*}{T^*}\right)^{n+\frac{3}{2},m+1}\gamma M_r{}^2. \tag{5.56}$$

Thus, the sensitivity of density at the next time level is estimated as:

$$\left(s_{\rho^*}\right)^{n+\frac{3}{2}}\approx\tilde{s}_{\rho^*}{}^{n+\frac{3}{2},m+1}+\left(\frac{W^*}{T^*}\right)^{n+\frac{3}{2},m+1}\gamma M_r{}^2\Delta s_{p^*}. \tag{5.57}$$

Substituting Equation 5.57 into Equation 5.54 yields the complete equation for the corrector of the sensitivity of pressure:

$$\delta_{x_j}\left[\delta_{x_j}\left(\Delta s_{p^*}\right)\right]-\frac{4}{\Delta t^{*2}}\left(\frac{W^*}{T^*}\right)^{n+\frac{3}{2},m+1}\gamma M_r{}^2\Delta s_{p^*}=\frac{4}{\Delta t^*}\left[\frac{\tilde{s}_{\rho^*}{}^{n+\frac{3}{2},m+1}-\left(s_{\rho^*}\right)^{n+\frac{1}{2}}}{\Delta t^*}+\delta_{x_j}\left(\tilde{s}_{g_j^*}{}^{n+1,m+1}\right)\right]. \tag{5.58}$$

The corrector for the sensitivity of pressure is obtained by solving Equation 5.58, the result of which will be substituted into Equation 5.52 to find the corrector for the sensitivity of mass flux, $\Delta s_{g_j^*}$. With the acquired correctors, the sensitivities of mass flux and pressure are updated using Equation 5.49 and 5.50, respectively.

7. Update the sensitivity of density.

The predicted sensitivity of density in Step 4, which uses the sensitivity of pressure at current equilibrium iteration, is updated by solving Equation 5.18 again with newly obtained sensitivity of pressure at the next equilibrium iteration:

$$s_{\rho^*}^{n+\frac{3}{2},m+1} = \left(\frac{W^*}{T^*}\right)^{n+\frac{3}{2},m+1} \left[\gamma M_r^{\,2} s_{p^*}^{n+\frac{3}{2},m+1} - \left(\frac{\rho^*}{W^*} s_{T^*}\right)^{n+\frac{3}{2},m+1} - \left(\rho^* T^* \sum_{k=1}^{N} \frac{s_{Y_k^*}}{W_k^*}\right)^{n+\frac{3}{2},m+1} \right]. \quad (5.59)$$

11. Calculate the sensitivity of velocity.

With the obtained sensitivity of mass flux from Step 6 and sensitivity of density from Step 7, the sensitivity of velocity is computed as:

$$s_{u_j^*}^{n+\frac{3}{2},m+1} = \frac{\left(s_{g^*}\right)^{n+\frac{3}{2},m+1} - s_{\rho^*}^{n+\frac{3}{2},m+1} u_j^{*n+\frac{3}{2}}}{\rho^{*n+\frac{3}{2}}}. \quad (5.60)$$

12. Determine the end of equilibrium iterations.

The values of sensitivities at the next time step are the final solutions of the repeated equilibrium iterations determined by reaching either a fixed number of iterations or a specified convergence criterion. It is apparent that as the corrector for the sensitivity of pressure converges to zero, Equation 5.58 is reduced to Equation 5.33, satisfying the sensitivity of continuity equation.

13. Evaluate the sensitivity of Rayleigh index.

The goal of the sensitivity calculations is to evaluate the sensitivity of Rayleigh index, which is the indicator of variations of thermoacoustic instabilities. At the end of each time step, the sensitivity of heat release rate due to chemical reaction is updated using the sensitivities of field variables at the new time level from Step 9. The sensitivity of Rayleigh index is then computed using the fluctuations of the sensitivities of pressure and heat release rate in the dimensional form:

$$s_\Omega = \int_0^\tau \int_0^V s_{\left(p'(\vec{x},t)\dot{w}_{T,c_p}'(\vec{x},t)\right)} dVdt = \int_0^\tau \int_0^V \left(s_{p'(\vec{x},t)} \dot{w}_{T,c_p}'\left(\vec{x},t\right) + p'\left(\vec{x},t\right) s_{\dot{w}_{T,c_p}'(\vec{x},t)} \right) dVdt. \quad (5.61)$$

5.4 Results

5.4.1 CFD Simulation

To demonstrate the effects of one of the modeling factors, reaction mechanism, results from both the global and two-step reaction mechanisms are presented. Considering the difficulty induced by the multi-step reaction model and the focus of this work being sensitivity of boundary conditions, only the results from global reaction mechanism are employed for the sensitivity equations, although it turns out that the multi-step reaction mechanism can improve the simulation results for heat release.

Figure 5.5 shows the temperature distribution along the centerline employing two different reaction mechanisms. The peak temperature drops from 1927K using the global mechanism to 1818K using the 2-step mechanism, with close outlet temperatures at 320K and 319K, respectively.

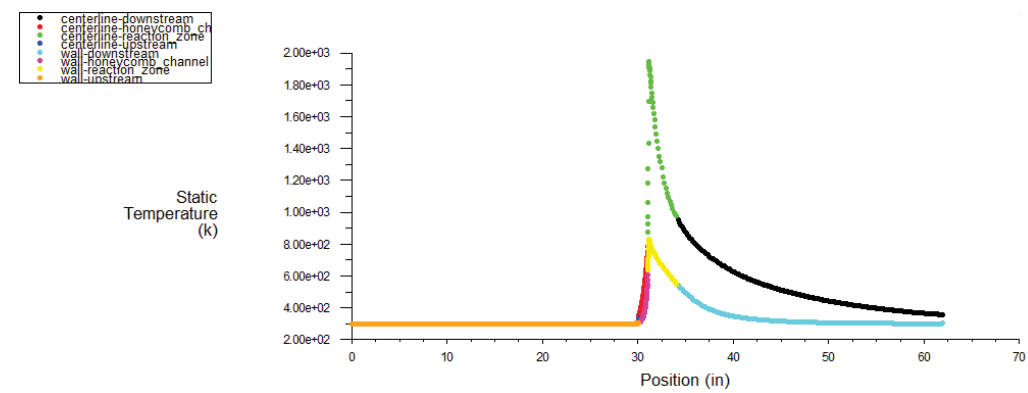

(a)

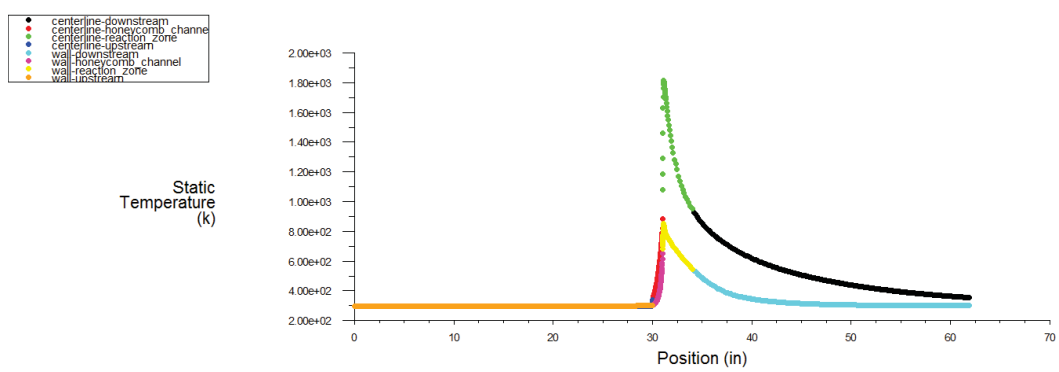

(b)

Figure 5.5: Temperature plots along the centerline and the flow wall at steady-state (a) Global reaction mechanism (b) 2-step reaction mechanism [K].

A closer look at the temperature, reaction rate and heat of reaction distributions in the honeycomb channels and the flame zone, seen in Figures 5.6-5.8, provides a better view of results using these two different reaction mechanisms. The flame heats up the honeycomb primarily by radiation, and produces a series of hot spots in the flat flame region. The flame is continuous, but more flat and closer to the top of honeycomb when using the 2-step reaction mechanism, which is considered as a better approximation and description of the combustion process. The distributions of reaction rate and heat of reaction overlap in contour plots, except that the heat of reaction is a lot weaker near the center of tube. It suggests that at a moment there is a lack of reactants at some locations in the reaction zone. Consequently, the heat of reaction is nearly zero. It is believed that the shortage of reactants is a direct result of the oscillations in flow velocity and mass fractions of reactants. Investigations of effects of different reaction mechanisms and radiation models are significant to the simulations of heat of reaction. The heat of reaction represents the heat release rate in combustion systems, which is a critical variable shown in the Rayleigh index, and necessary for the thermoacoustic instability prediction.

As discussed in Section 1.1, vortex structures influence the flame dynamics. The coupling between vortex and flame is also a driving force for thermoacoustic instabilities. Behavior of vortex structures is examined in Figure 5.9. Vortices are weakened in time with larger variations near the centerline, and disappear after 0.27s. Thus for the self-excited Rijke tube, the vortex-flame interaction is neither the main reason for the continuous growth of fluctuations of pressure and heat release rate, nor for the limit cycle.

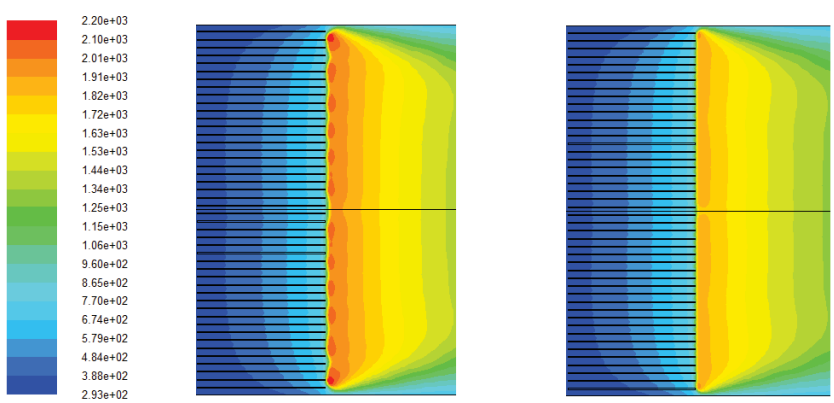

(a) (b)

Figure 5.6: Temperature contour plots for honeycomb channels and flame zone at steady-state (a) Global reaction mechanism (b) 2-step reaction mechanism, [K].

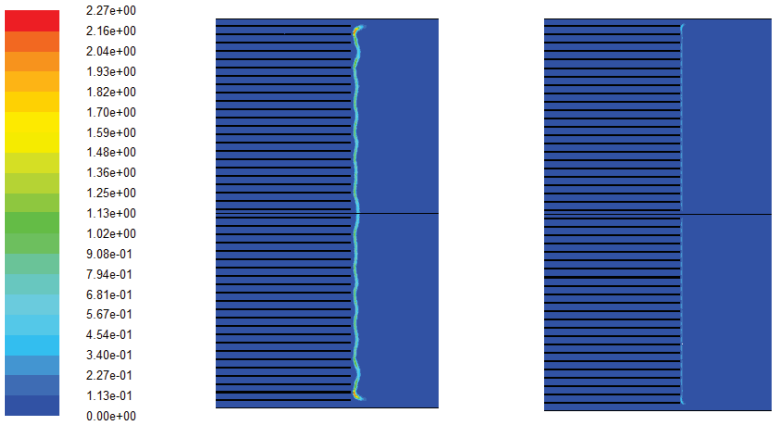

(a) (b)

Figure 5.7: Reaction rate contour plots at steady-state (a) global reaction mechanism (b) 2-step reaction mechanism, [kmol/m^3·s].

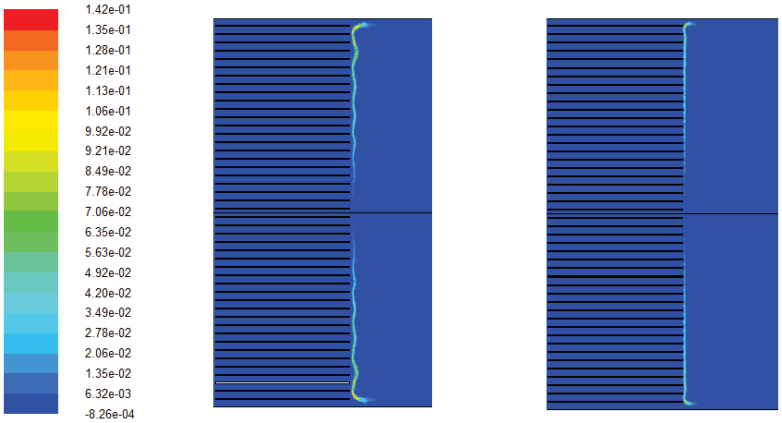

(a) (b)

Figure 5.8: Heat of reaction contour plots at steady-state (a) global reaction mechanism (b) 2-step reaction mechanism, [W].

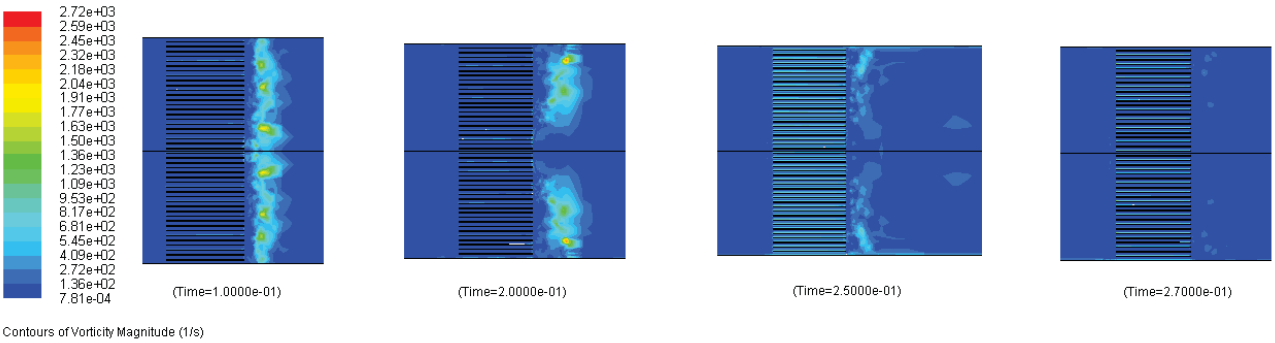

Figure 5.9: Vorticity magnitude contour plots at 0.1s, 0.2s, 0.25s, and 0.27s, respectively [1/s].

Figure 5.10 shows the development of static pressure at a location near the honeycomb in the flame zone where most heat is released. An initial perturbation excited the flow field. Pressure oscillations started to grow due to in-phase heat addition. The amplitude of pressure oscillations did not grow infinitely as in the ideal condition. It reached a "saturated" state, the limit cycle, around 1 second, and maintained pressure oscillations with an amplitude of 400Pa. The saturated state is a result of nonlinear effects. It is also noted that there is an overshooting region during the transition from the nearly linear growth to the limit cycle, which is in agreement with observations in experiments. The increasing pressure manifests the occurrence of thermoacoustic instabilities in Rijke tube, indicating the ability of this CFD model to capture the detailed physics involved in thermoacoustic phenomenon. It is impressive but not surprising that this simulation run for 1.2 second of the physical process took 7 months' computational time on a work station with 52G RAM and 16 processors. This is the price using the DNS to resolve all details that require extensive time and computational resources to model the complex flow field of multi species, dimension, and time represented in evolving the highly nonlinear Navier-Stokes equations.

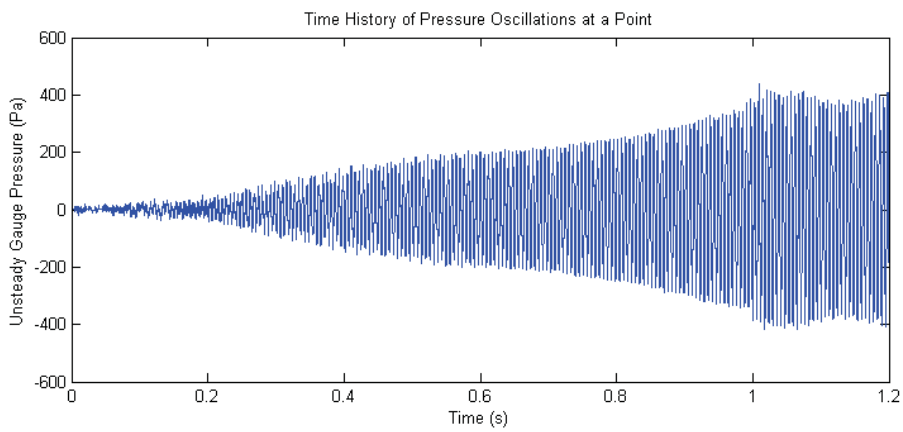

Figure 5.10: Static pressure time history plot at the point x=31.1in and y=0.75in [Pa].

Additional information can be acquired from the frequency component plot for pressure oscillations. Figure 5.11 shows that more than one acoustic mode is excited, while the second acoustic mode at 168.8Hz for the pure flow tube is dominant. The range of the eigen-frequencies, usually less than 1000Hz, is in good agreement with the experimentally observed range for lean premixed laminar combustors.

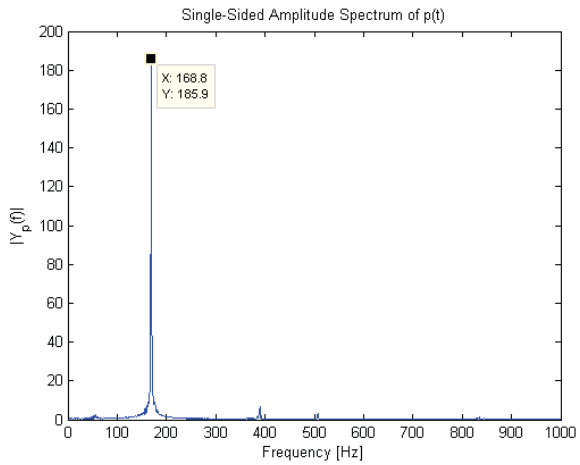

Figure 5.11: FFT plot of gauge pressure at the point x=31.1in and y=0.75in.

The mode shape of a three-quarter wave depicted in Figure 5.12 corresponds to the second acoustic mode. Figure 5.13 gives the velocity mode shape at the same time as pressure mode shape in Figure 5.12. Comparison of the maximum positions of these two plots shows that pressure is lagging velocity by 90˚, which is consistent with the conclusion drawn by Hantschk and Vortmeyer [6]. Negative values of velocity indicate the fluctuations of flow rate occurring in the Rijke tube, while the total mass flow rate is conserved.

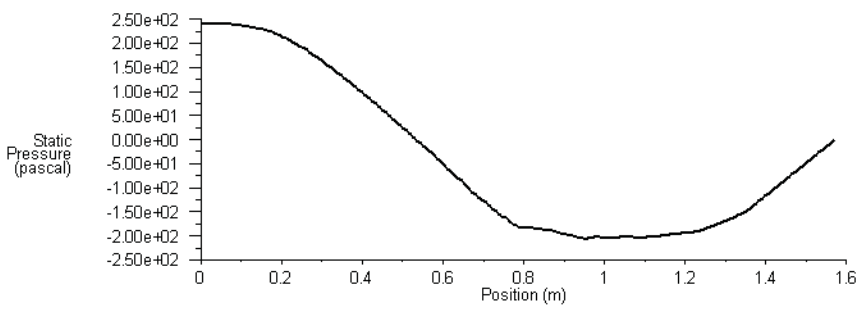

Figure 5.12: Pressure distribution along the centerline at t=1.2s [Pa].

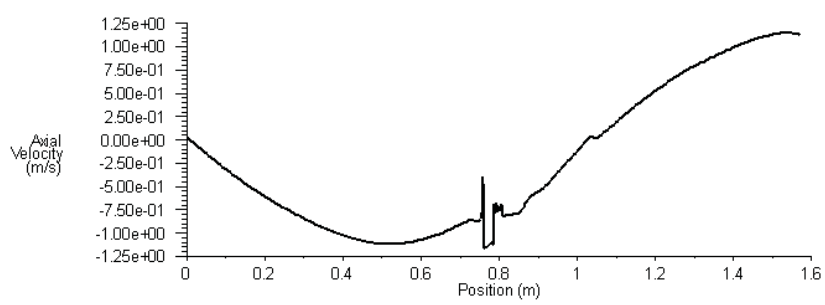

Figure 5.13: Axial velocity distribution along the centerline at t=1 [m/s].

Comparison of the time-evolving behaviors of the primary field variables in Figure 5.14 reveals the coupling nature of different variables and detailed relationship between them. The transition point for pressure oscillations from quasi-linear increase to the limit cycle is also where temperature, heat release and local Rayleigh index have significant changes. The evolution of heat release rate shows a similar overshooting interval around 1s. This behavior is evident to be a response to the fluctuation in pressure or velocity. It should be noted that this statement does not imply the order in which the oscillations of these variables happen. It is difficult to decouple the interaction of these field variables. A slight time lag in the largest amplitude of temperature with respect to heat release rate may result from the interaction between temperature and mass fraction of species, which is explained by Arrhenius formula for the reaction rate. The large amplitude of oscillations in local Rayleigh index reflects the strong nonlinear effects responsible for appearance of the limit cycle.

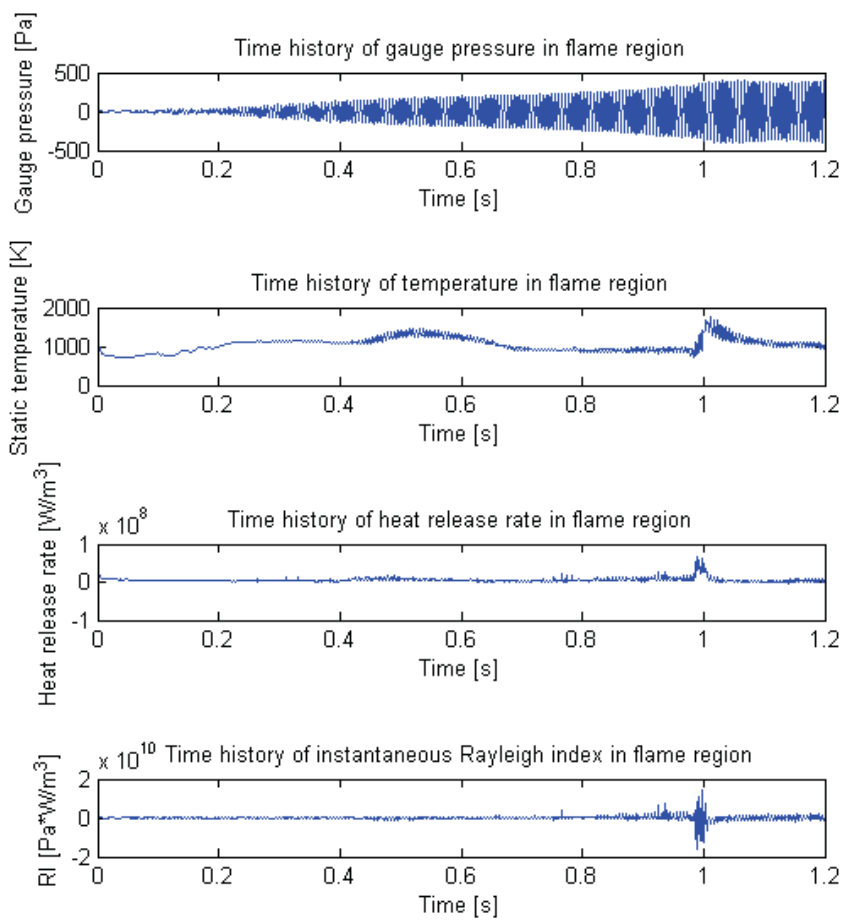

Figure 5.14: Time history plots for pressure, temperature, heat release rate and local Rayleigh index at the point x=31.1in and y=0.75in.

Time series of data for variables provide important information regarding to the transition time point between different scenarios. Frequency component decompositions contain information about which harmonics are excited and whether there exist sub-harmonics or pulsating instabilities. Figure 5.15 shows a dominant frequency 168.8Hz for all pressure, temperature, heat release rate and Rayleigh index oscillations at a specified point in the flame region of the Rijke tube. The second largest spectrum line for the local Rayleigh index corresponds to a frequency of 338.9Hz, which is not a harmonic. This is another consequence of the interaction between variables.

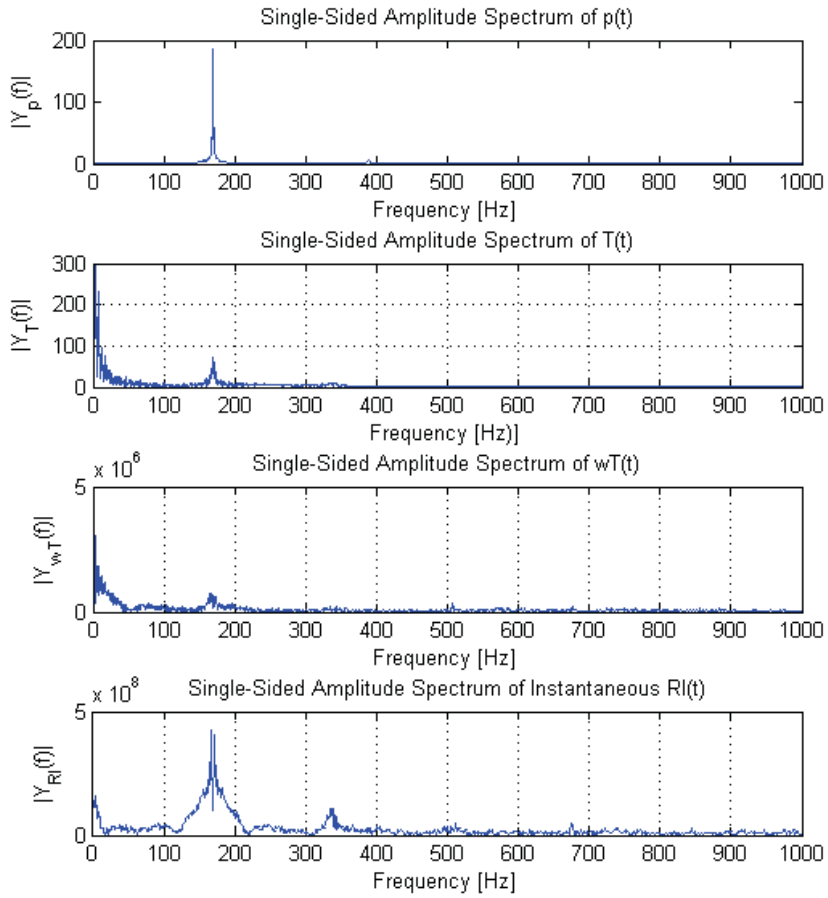

Figure 5.15: FFT plots for pressure, temperature, heat release rate and local Rayleigh index at the point x=31.1in and y=0.75in.

Accurate calculation of field variables forms the basis for evaluation of Rayleigh criterion. The time history of local Rayleigh index in Figure 5.14 shows a similar trend with field

variables, but the large oscillations at the beginning of limit cycle need further examination and explanation by studying the fluctuations of pressure and heat release rate. Figures 5.16-5.17 show relative phases between the normalized pressure and heat release rate. It is noted from the enlarged plots that the relative phase between fluctuations of pressure and heat release rate are not always positive or negative as in the simple heating elements Rijke tube model. The phase changes lead to the oscillation of local Rayleigh index between some positive and negative values. The large oscillations of local Rayleigh index convey little information about the future development of thermoacoustic instabilities. Thus the integrated Rayleigh index comes into play in order to account for the overall effects and predict the developing direction of thermoacoustic instabilities.

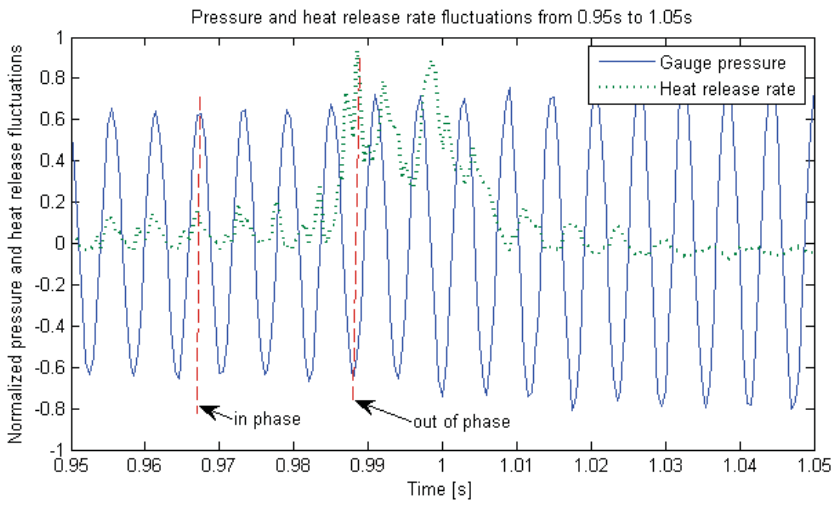

Figure 5.16: Normalized pressure and heat release rate fluctuations from 0.95s to 1.05s.

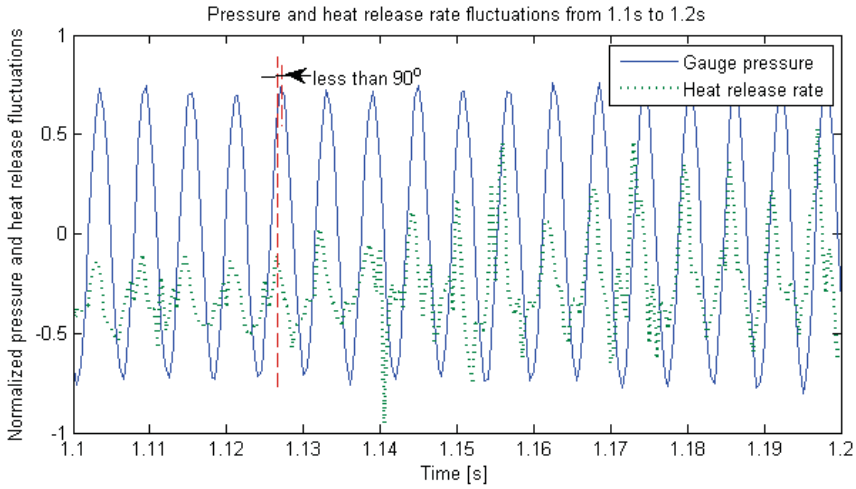

Figure 5.17: Normalized pressure and heat release rate fluctuations from 1.1s to 1.2s.

Thermoacoustic instability is an overall effect of the coupling between the fluctuations of pressure and heat release. As the indicator of thermoacoustic instabilities, the Rayleigh index is an integral over space and time. The integrant of the Rayleigh index is denoted by RI, the integral of which over the space and the time is denoted by the subscripts, *s* and *t*, respectively. Figure 5.18 displays the time evolving of Rayleigh index integrated over the entire tube. The behavior after around 1.04s deviates from the one for a local point in the flame region. This deviation confirms the necessity of performing integration for the instantaneous local Rayleigh index. Since the real signal contains infinite frequency components, it is intuitive to choose the acoustic resonance frequency that has the most influence on the amplitude amplification to determine an effective time interval as a period for oscillations. The Rayleigh index integrated over the period of limit cycle, which is determined by the second resonance frequency, tends to predict the amplifying or damping process of acoustic pressure in the next time period. The marked Rayleigh index for the limit cycle in Figure 5.19 overpredicted the change in thermoacoustic instabilities. As in the limit cycle, the amplitude is "saturated", neither increases nor decreases, indicating a zero net heat addition to the acoustic field. Recall that there is limited damping in a confined combustion system, then a zero net heat addition means a Rayleigh index close to zero. Since the Rayleigh index computation is based on the CFD data mapped onto a coarser uniform grid used for sensitivity calculation, the over prediction is very likely a result of the coarse grid used to interpolate CFD data, which is restricted by the enormous computational time of this problem. As a result, a single cell in the computational domain may influence the integrated Rayleigh index.

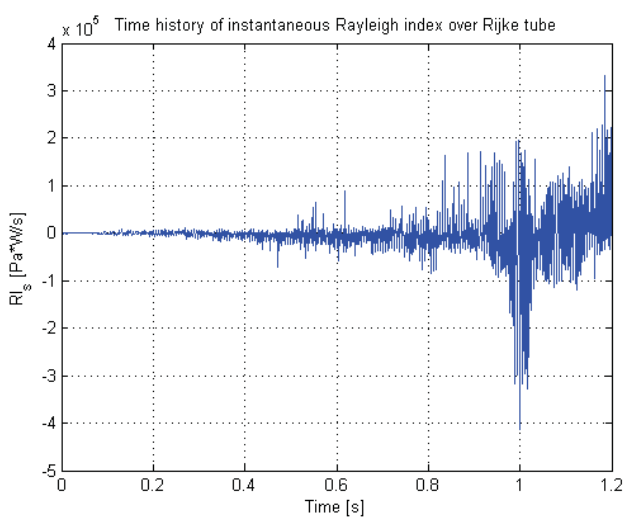

Figure 5.18: Time history plot of Rayleigh index over the Rijke tube [Pa·W/s].

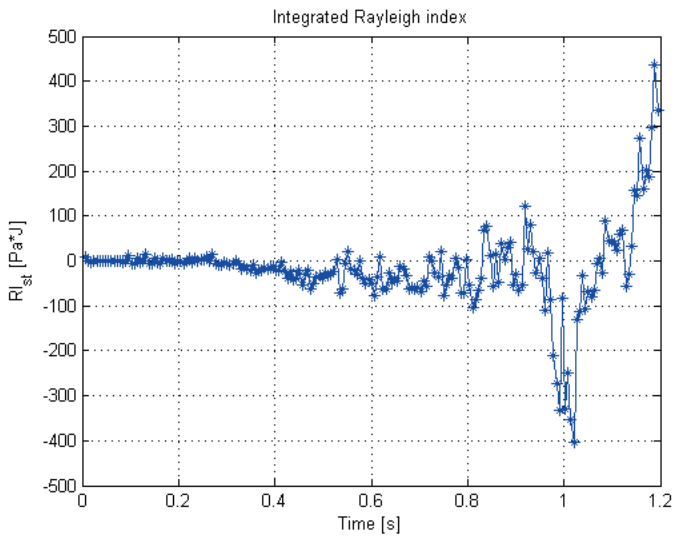

Figure 5.19: Time history plot of Rayleigh index integrated in space and time [Pa·J].

5.4.2 Sensitivity analysis

The sensitivity analysis is performed to investigate the effects of two boundary conditions, i.e. the inlet mass flux associated with the mass flow rate and the equivalence ratio, on the occurrence and development of thermoacoustic instabilities.

5.4.2.1 Sensitivity to g_{bc}

The effects of inlet mass flow rate boundary on the simulation of thermoacoustic instabilities are studied in this section. Since the momentum per unit volume g is the variable that is advanced in the momentum equation, and g_{bc} is proportional to the inlet mass flow rate $\dot{m}$, the sensitivities of field variables and the Rayleigh index with respect to g_{bc} are calculated instead of $\dot{m}$.

Figures 5.20 (a)-(c) depict the evolution of sensitivities of the pressure, the heat release rate and the Rayleigh index to variations of the incoming flow rate in time. Due to the large scale present in these plots, only the transition point for time series of sensitivities is visible. The transition point is identical for all three variables. The rapid drop at around 0.216s for the sensitivity of heat release rate does not agree with our understanding for general problems that increased mass flow rate brings more fuel-air mixture and consequent more heat release. However, the drop is exactly what thermoacoustic instabilities would induce for some specific

location and time point. At a particular moment, the fluctuations in pressure and heat release rate lead to some zero pressure or zero heat release locations, which are the responses of pressure and heat release to the boundary condition changes in mass flow rate. The flow rate is increased, but the pressure and heat release rate are reduced, resulting negative sensitivities with respect to the mass flow rate. The fluctuations may not make exactly "zero" heat release locations, but the pressure and heat release rate in those areas are too small compared to their old values before seeing the boundary changes so that negative sensitivities appear. It is also noted that decreases in pressure and heat release rate give rise to an increase in Rayleigh index, namely an increase in the opportunity of the amplification of acoustic pressure.

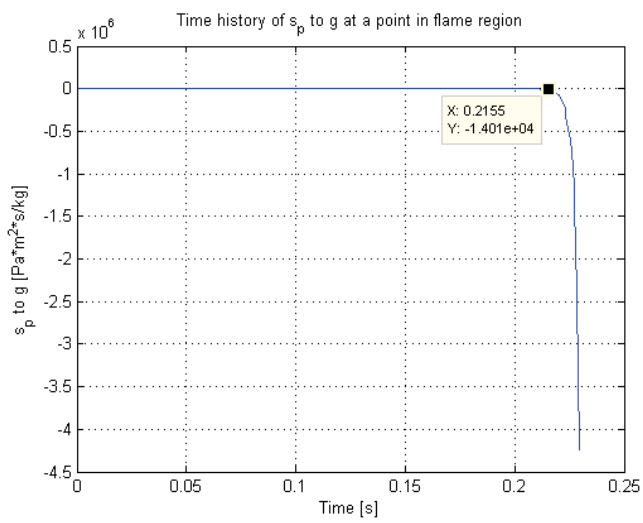

(a)

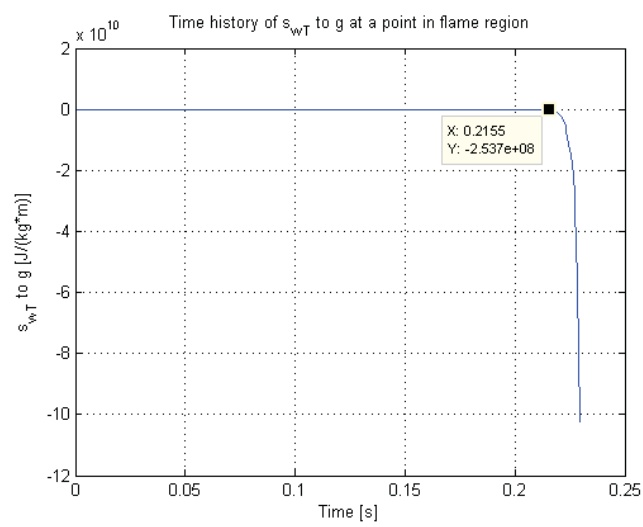

(b)

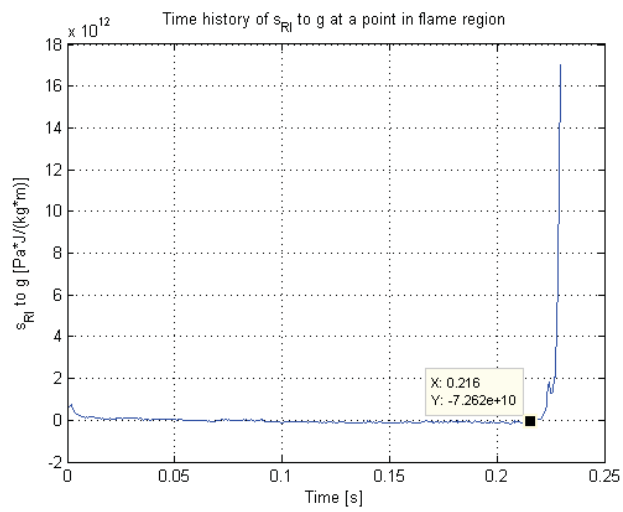

(c)

Figure 5.20: Time history plots for sensitivities of (a) pressure, (b) heat release rate, (c) local Rayleigh index to inlet flow rate at the point x=31.1in and y=0.75in.

Enlarged plots for the early stage developments of sensitivities supplement the information about the responses of variables to inlet flow rate variations. It is evident from Figure 5.21(a) that at different time points, the pressure at a specified spot in flame region responds quite differently. The amplitude of s_p is growing in time, indicating the pressure gets more sensitive to the inlet flow rate as time marches. It is also noted that the difference of responses at different time not only lies in the amount of changes, but also the direction of changes. The sensitivity of pressure is not always positive or negative. Instead, it is oscillating. The primary reason is that the oscillations of sensitivities are associated with the oscillatory nature of field variables, which is time dependent. This is especially true for the time points when the onset of thermoacoustic instabilities is observed. As to the change in the heat release rate, increased inlet flow rate leads to a rapid increase in the heat release rate for the early stage and little change for the period from 0.01s to 0.14s shown in Figure 5.21(b). Figure 5.21(a) and 5.21(b) together demonstrate that increased incoming flow aggravates the oscillations of field variables. The impact of the amplified oscillations of field variables on thermoacoustic instabilities depends on the coupling effects of sensitivities of pressure and heat release rate. The sensitivity of Rayleigh index shown in 5.21(c) increases with the enhanced inlet flow rate until 0.06s, and starts to oscillate and decrease. It suggests that the possibility of the occurrence of thermoacoustic instability is

increased before 0.06s, and decreased afterwards. This provides control of thermoacoustic instability with appropriate time points.

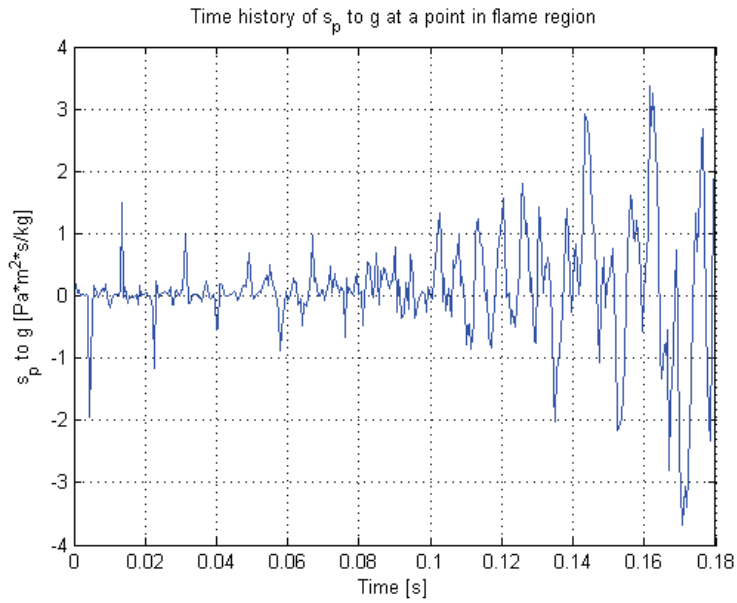

(a)

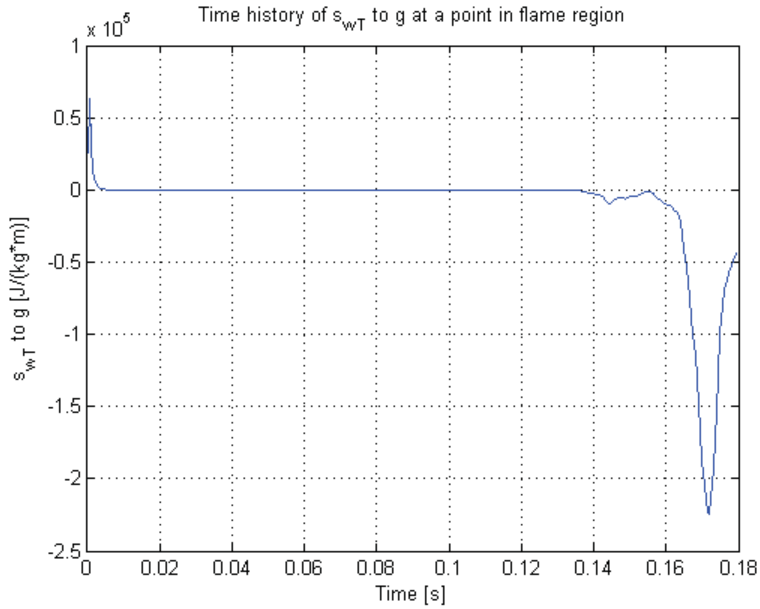

(b)

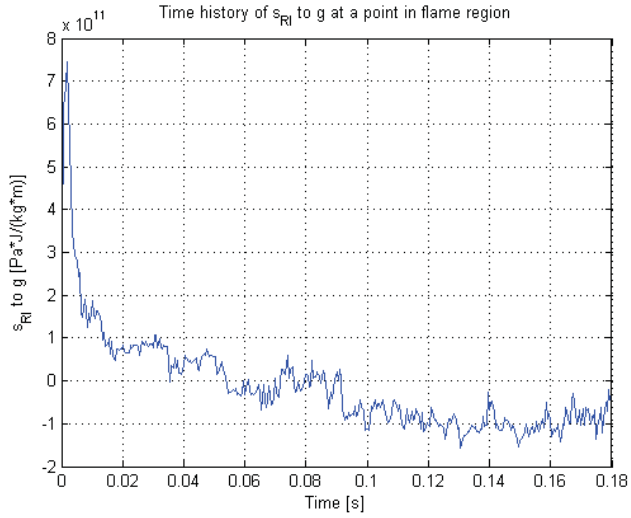

(c)

Figure 5.21: Time history plots for sensitivities of (a) pressure, (b) heat release rate, (c) local Rayleigh index to inlet flow rate at the point x=31.1in and y=0.75in from 0-0.18s.

Figure 5.22 is the integrated sensitivity of Rayleigh index over the entire computational domain. The plot on the right shows the amplitudes of the instantaneous sensitivity of Rayleigh index. Further integration over period gives the trend of sensitivity of Rayleigh index in Figure 5.23. The integrated sensitivity of Rayleigh index has a decreasing though oscillatory trend. Positive sensitivities appear before 0.035s and negative sensitivities exist until the system hits the transition point at 0.0216s, where a small disturbance will excite large oscillation of field variables.

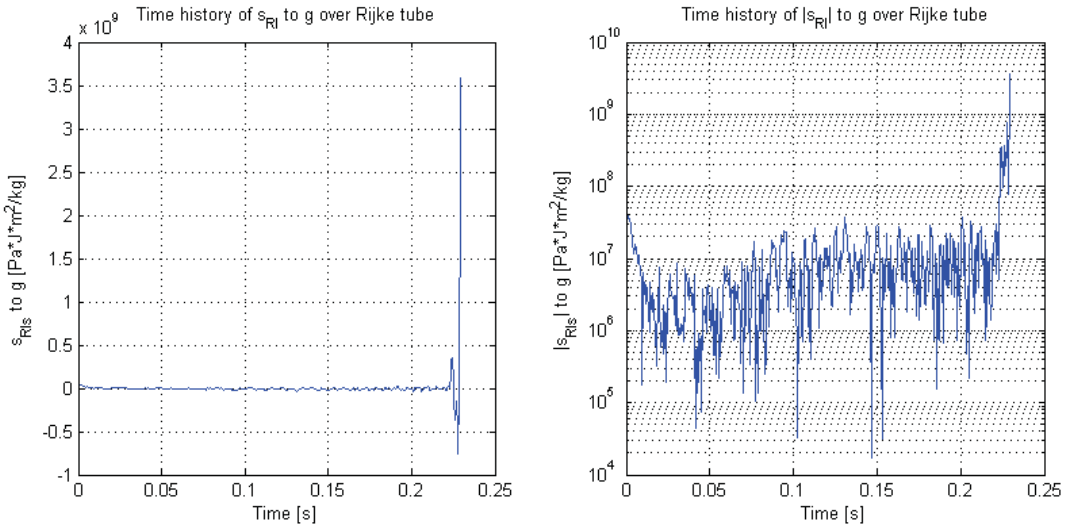

(a) (b)

Figure 5.22: Time history plot for sensitivities of Rayleigh index to inlet flow rate over Rijke tube (a) true value (b) absolute value in log scale [Pa·J·m^2/kg].

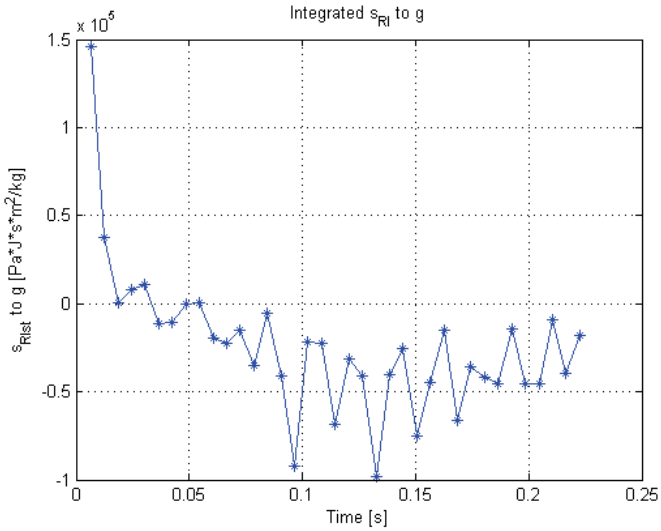

Figure 5.23: Time history plot for sensitivities of integrated Rayleigh index to inlet flow rate [Pa·J·s·m^2/kg].

5.4.2.2 Sensitivity to ϕ

Equivalence ratio has been proven previously to be a parameter that will affect the thermoacoustic phenomenon. But research was limited to qualitative conclusions. It is significant to study to what extent the field variables are sensitive to the equivalence ratio.

The sensitivities of field variables to equivalence ratio in Figure 5.24 present an opposite trend with those to inlet flow rate. The transition point is at 0.225s, later than that for the inlet flow rate case, 0.216s. The key feature is that the sensitivities of pressure and heat release rate to equivalence ratio have rapid increases at the transition point, with a rapid decrease of the Rayleigh index due to coupling.

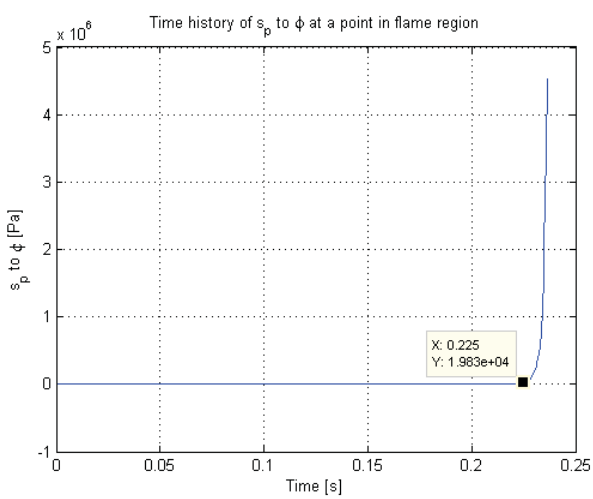

(a)

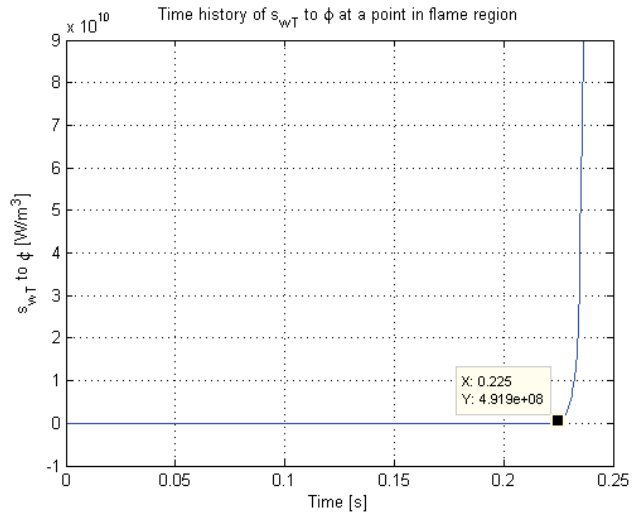

(b)

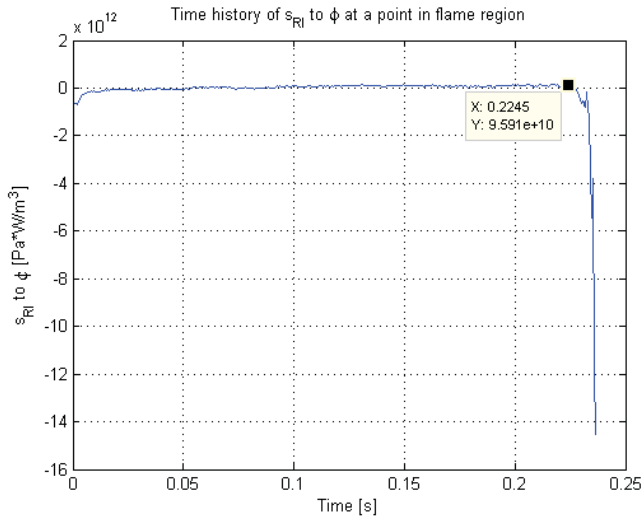

(c)

Figure 5.24: Time history plots for sensitivities of (a) pressure, (b) heat release rate, (c) local Rayleigh index to equivalence ratio at the point x=31.1in and y=0.75in.

It is interesting that the sensitivity of pressure with respect to the equivalence ratio possesses a primary frequency component. This oscillatory pattern shows a different period from what is used for Rayleigh criterion calculations as seen in Figure 5.25(a). However, this pattern "blows up" at around 0.2s. The mechanism behind this special pattern is still under investigation and not discussed in this dissertation. The sensitivity of heat release rate in Figure 5.25(b) shows a big variation starting at an earlier time of 0.16s. The resulting sensitivity of the Rayleigh index in Figure 5.25(c) is increasing in time, and becomes positive at around 0.09s, indicating an increase of the Rayleigh index as equivalence ratio increases.

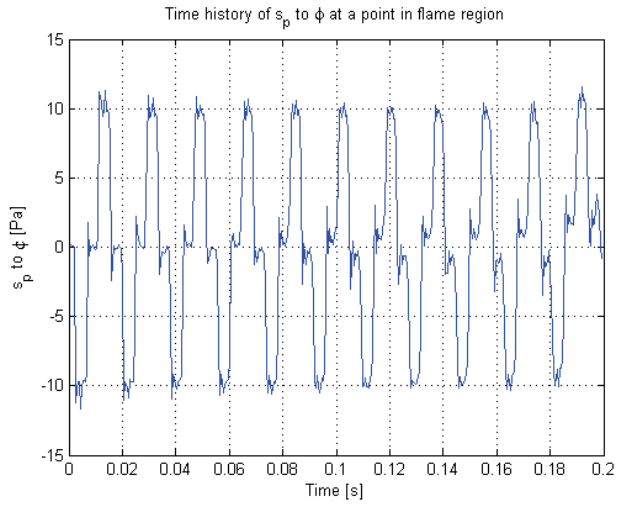

(a)

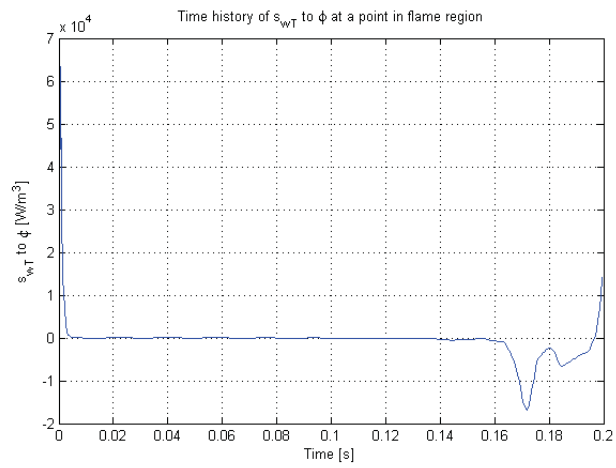

(b)

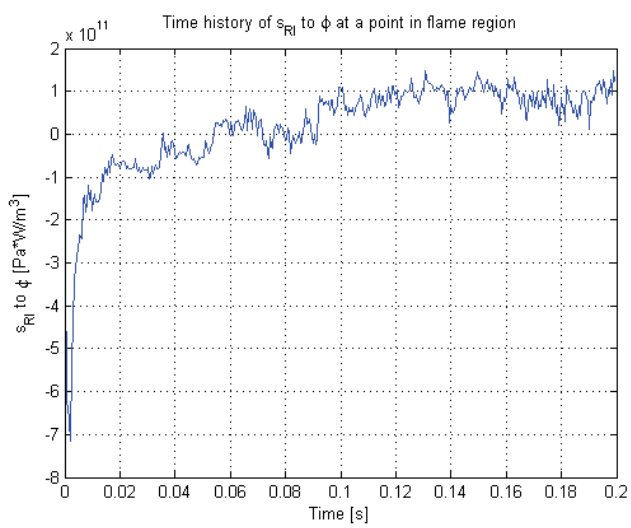

(c)

Figure 5.25: Time history plots for sensitivities of (a) pressure, (b) heat release rate, (c) local Rayleigh index to equivalence ratio at the point x=31.1in and y=0.75in from 0-0.2s.

Figures 5.26 and 5.27 plot the time series of integrated sensitivities of the Rayleigh index over the entire computational domain and the oscillation period respectively. The sensitivity of Rayleigh index has an increasing trend, with positive sensitivities of Rayleigh index showing up at 0.035s. This trend suggests that the possibility of the occurrence and aggravation of thermoacoustic instabilities will increase in time as the equivalence ratio increases. For the purpose of control, operation should be performed during the period when the Rayleigh index has great changes with variations in the equivalence ratio. It should be mentioned that the sensitivity is valid for a small range of variations. The fact that increased equivalence ratio destabilizes the lean premixed system does not suggest the influence of even higher equivalence ratios.

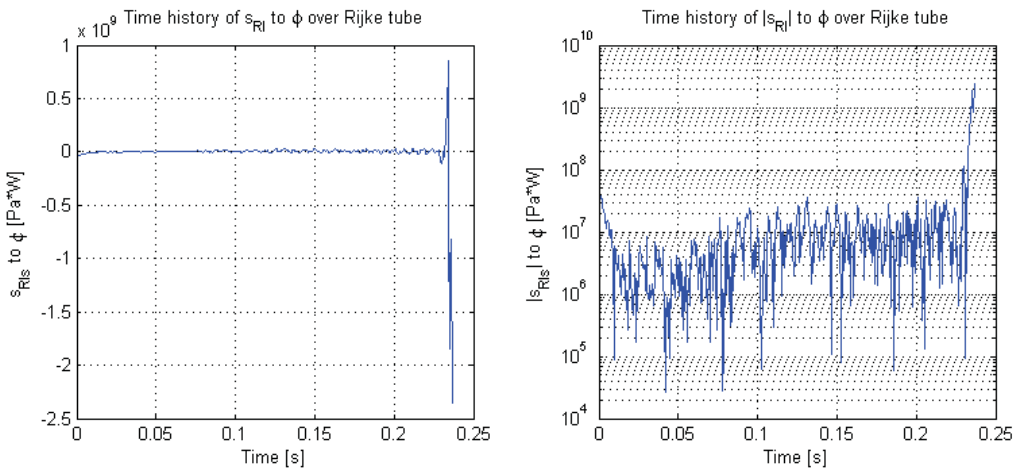

Figure 5.26: Time history plot for sensitivities of Rayleigh index to equivalence ratio over Rijke tube (a) true value (b) absolute value in log scale [Pa·W].

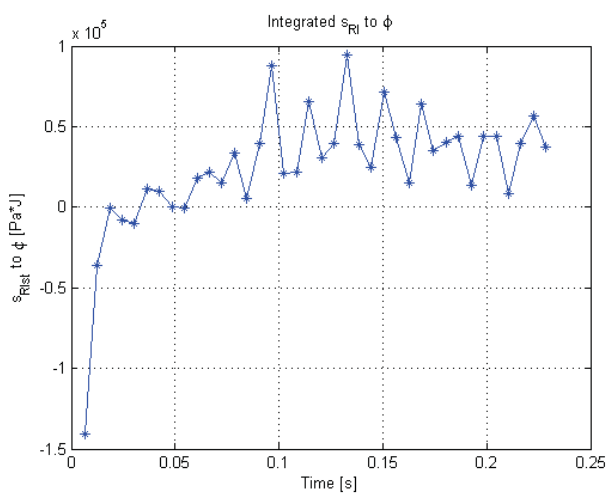

Figure 5.27: Time history plot for sensitivities of integrated Rayleigh index to equivalence ratio [Pa·J].

Chapter 6

Conclusions and Perspectives

Applications of the CSEM analysis to thermoacoustic instabilities were demonstrated by the one-dimensional thermoacoustic convection problem in Chapter 4 and the self-excited Rijke tube problem in Chapter 5. This chapter discusses the findings and future work for both the CFD simulation and the sensitivity analysis of thermoacoustic instabilities.

6.1 CFD simulations

For a specific thermoacoustic problem, only one CFD simulation case is required for the CSEM analysis of thermoacoustic instabilities. The computational models for thermoacoustic instabilities were built and improved to best resolve the physics. In the meantime, the influential modeling factors were also investigated.

The CFD simulations have successfully captured the mean flow effects and nonlinear effects by solving the coupled nonlinear governing equations. For the one-dimensional thermally induced acoustics, the heat source is a heated wall, and convection takes the main effects on modification of the flow and heat fields, which is relatively easy to model. The simulation results showed that the static pressure was monotonically increasing, and reached 1.3 times of the initial value asymptotically. The thermoacoustic instability occurred in the modified Rijke tube is much more complicated. With the CFD simulations carried out in ANSYS Fluent 14.0, two important,

but often ignored or simplified factors in accurate modeling of thermoacoustic instability phenomenon have been identified, i.e. the radiation model and reaction mechanism. The radiation as an effective damping mechanism plays a critical role in the prediction of the occurrence of thermoacoustic instability. The honeycomb top radiates heat radially to the Rijke tube wall and axially to the downstream region heating the products, all of which affect the heat release rate from the flame, significantly influencing the thermoacoustic instability. The other critical modeling factor that could have a large impact on the modeling of heat release process is the reaction mechanism employed. Comparisons have been made between the global reaction mechanism which has been widely used and the two-step reaction mechanism. The two-step reaction mechanism produced a flame temperature closer to the actual non-adiabatic flame temperature of methane, promoting the motivation of incorporating a multi-step reaction mechanism to represent the chemical reaction involved. However, the focus of the current research is on the sensitivity of boundary condition effects, the sensitivity of modeling parameters was not assessed.

With the detailed physical processes resolved and accurate field variables extracted, the Rayleigh criterion was evaluated. There existed a rapid change of the Rayleigh index during the start of the limit cycle in the Rijke tube. It is believed that this change corresponds to the nonlinear effects leading to the limit cycle, but the detailed interactions and causes are to be determined. The relative phase of fluctuations of pressure and heat release rate has been plotted, which was in agreement with the calculated Rayleigh index.

6.2 Sensitivity analysis

Because the CSEM are obtained by directly differentiating the governing equations with respect to parameters that may have influence on the field variables, it represents the sensitivities exactly the same way that governing equations represent field variables. The reliability of this approach is thus ensured. However, also because the CSEs are associated with the governing equations, the solutions of CSEs are strongly dependent on the solution of flow fields. The accuracy of the solution to governing equations for thermoacoustic instability problems is still a challenging task. Although positivity of the Rayleigh index is a direct indicator of the occurrence

of the excitation of thermoacoustic instability, an accurate quantitative expression is necessary to evaluate the sensitivities. A minor error in the Rayleigh index is likely to incorrectly predict the instability when some parameters have been changed. This issue involves verification and validation of the computational results. Experiences in experiments and qualitative solutions can be used to rule out some impractical results. The axisymmetric model of the Rijke tube with heating elements developed by Hantschk and Vortmeyer [6] provides a test bench for the application of the CSEM to thermoacoustic instability problems.

The CSEs with respect to the heated wall temperature were solved by an explicit finite difference scheme for the one-dimensional thermoacoustic convection problem. The application of the CSEM to thermoacoustic instability in a Rijke tube combustor was performed using a pressure-correction solver written in MATLAB. Responses of field variables to variations in the inlet mass flow rate and the equivalence ratio were obtained and utilized to evaluate the sensitivity of the Rayleigh index. Both applications showed rapid increases in the magnitudes of sensitivities of the field variables and the Rayleigh index, leading to "blowup" of sensitivity values in the early stage of the development of thermoacoustic instabilities. Moreover, the mass flux boundary and the equivalence ratio turned out to have opposite influence on the stability of the lean premixed combustion system. The oscillatory nature of the sensitivity of the Rayleigh index suggests the necessity of treating the occurrence of thermoacoustic instabilities as an overall effect of the coupling process, which could guide the suppression of thermoacoustic instabilities. By applying the CSEM, all sensitivities were obtained for small variations around the reference state, i.e. the selected CFD simulation case. Therefore, prediction of thermoacoustic instabilities is reliable over a small range of the investigated boundary parameter.

Since the CSEM only requires one case of the CFD simulation, similarly, only one set of experimental data for one set of boundary conditions is required to predict thermoacoustic instability phenomenon under different operating conditions in industry. It reduces a considerable amount of time of conducting experiments and cost in updating equipment. More promisingly, if the amplitude of pressure could be appropriately represented, the response of amplitude to boundary condition changes could be predicted, providing reliable reference for control of thermoacoustic instabilities.

6.3 Perspectives

The ability of the CSEM to predict thermoacoustic instabilities has been demonstrated with much potential to be exploited. In order to maximize the advantage of the application of the CSEM to thermoacoustic problems and acquire a more thorough and accurate prediction of the onset of thermoacoustic instabilities, there is still continued work that could be accomplished.

1. The CSEM is not only applicable to the analysis of the effects of boundary parameters, but also capable of evaluating the influence of modeling factors. As the importance of more detailed radiation model and reaction mechanism has been elucidated, it is necessary to incorporate them into the sensitivity solver and take into account their effects on the heat release rate calculation. Both the explicit finite difference solver and implicit pressure-correction solver have the flexibility of incorporating more detailed physics and more complicated representation of boundary conditions and modeling factors.
2. The present work applied the classic Rayleigh criterion to predict the occurrence of thermoacoustic instabilities, which is simple but adequate for the purpose of this research. However, some recent research reveals that additional loss mechanism of energy in the combustion system also plays a significant role. The proposed formulation in this dissertation could be easily extended to the Chu criterion from the classic Rayleigh criterion to account for the effects of additional mechanisms.
3. Although the sensitivity equations share the same structure as the governing equations, the sensitivities cannot be obtained simultaneously in the commercial CFD software, such as ANSYS Fluent 14.0. It is desirable to build the CFD and sensitivity solver in the same loop so that sensitivities can be obtained once CFD results are available at any time, saving the exporting and importing efforts, especially for the considerably large data set. To realize the desired solution process, the solver used in this dissertation needs to be tailored and optimized in terms of the scheme method employed, or converted to C language or Fortran to accelerate the computing process.
4. OpenFOAM is a potential substitute for ANSYS Fluent 14.0. As an open CFD source, OpenFOAM is able to solve a variety of CFD problems. More importantly, the sensitivity solver developed in this dissertation could be applied to any CFD problems, provided the feature of incorporating the chemical reactions and acoustics. Therefore, the sensitivity

solver will expand the functionality of OpenFOAM, contributing to the in-depth exploration of CFD problems.

Bibliography

[1] Chishty, W. A., and Klein, M., "Combustion and Emission Issues in Gas Turbines " Proc. 2009 IAGT symposium : innovative and reliable energy solutions, Industrial Application of Gas Turbines Committee.

[2] Rayleigh, L., 1878, "The explanation of certain acoustical phenomena," Nature, 18(455), pp. 319-321.

[3] Kopitz, J., Huber, A., Sattelmayer, T., and Polifke, W., 2005, "Thermoacoustic stability analysis of an annular combustion chamber with acoustic low order modeling and validation against experiment," Proceedings of the ASME Turbo Expo, 2, pp. 583-593.

[4] Kopitz, J., and Polifke, W., 2008, "CFD-based application of the Nyquist criterion to thermo-acoustic instabilities," J Comput Phys, 227(14), pp. 6754-6778.

[5] Palies, P., Schuller, T., Durox, D., and Candel, S., 2011, "Modeling of premixed swirling flames transfer functions," P Combust Inst, 33, pp. 2967-2974.

[6] Hantschk, C. C., and Vortmeyer, D., 1999, "Numerical simulation of self-excited thermoacoustic instabilities in a Rijke tube," J Sound Vib, 227(3), pp. 511-522.

[7] Chatterjee, P., 2004, "A computational fluid dynamics investigation of thermoacoustic instabilities in premixed laminar and turbulent combustion systems,"Doctoral dissertation, Virginia Polytechnic Institute and State University.

[8] Mantel, T., Egolfopoulos, F. N., and Bowman, C. T., "A new methodology to determine kinetic parameters for one- and two-step chemical models," Proc. the Summer Program 1996.

[9] Zambon, A. C., and Chelliah, H. K., 2007, "Acoustic-wave interactions with counterflow single- and twin-premixed flames: Finite-rate kinetics, heat release and phase effects," P Combust Inst, 31 I, pp. 1247-1255.

[10] Poinsot, F. N. a. T., 2005, "Thermoacoustic instabilities: Should the Rayleigh criterion be extended to include entropy changes?," Combust Flame, 142(1-2), pp. 153-159.

[11] "A cookbook for applying sensitivity analysis in practical cases of modelling."

[12] Spradley, L. W., Bourgeois, S. V., Fan, C., and Grodzka, P. G., 1973, "A Numerical Solution for Thermoacoustic Convection of Fluids in Low Gravity," United States.

[13] Tyndall, J., 1867, Sound: A Course of Eight Lectures Delivered at the Royal institution of Great Britain, Longmans, Green and Co., London.

[14] Rayleigh, J., 1945, The Theory of Sound, Dover Publications, New York.

[15] Feldman Jr, K. T., 1968, "Review of the literature on Rijke thermoacoustic phenomena," J Sound Vib, 7(1), pp. 83-89.

[16] Raun, R. L., Beckstead, M. W., Finlinson, J. C., and Brooks, K. P., 1993, "A review of Rijke tubes, Rijke burners and related devices," Prog Energ Combust, 19(4), pp. 313-364.

[17] Bisio, G., and Rubatto, G., 1999, "Sondhauss and Rijke oscillations—thermodynamic analysis, possible applications and analogies," Energy, 24(2), pp. 117-131.

[18] Culick, F. E. C., 2006, Unsteady Motions in Combustion Chambers for Propulsion Systems, RTO/NATO.

[19] Dennis, A. A. P. a. W. R., 1954, "Burner oscillations of the gauze-tone type," J Acoust Soc Am, 26, pp. 716-725.

[20] Chu, B. T., 1956, "Stability of systems containing a heat source - the Rayleigh criterion," NACA Research memorandum NACA RM 56D27.

[21] Mcmanus, K. R., Poinsot, T., and Candel, S. M., 1993, "A Review of Active Control of Combustion Instabilities," Prog Energ Combust, 19(1), pp. 1-29.

[22] Venkataraman, K. K., Preston, L. H., Simons, D. W., Lee, B. J., Lee, J. G., and Santavicca, D. A., 1999, "Mechanism of Combustion Instability in a Lean Premixed Dump Combustor," J Propul Power, 15(6), pp. 909-918.

[23] Lieuwen, T., 2003, "Modeling Premixed Combustion-Acoustic Wave Interactions: A Review," J Propul Power, 19(5), pp. 765-781.

[24] Sé, Ducruix, b., Schuller, T., Durox, D., Sé, and Candel, b., 2003, "Combustion Dynamics and Instabilities: Elementary Coupling and Driving Mechanisms," J Propul Power, 19(5), pp. 722-734.

[25] Huang, Y., and Yang, V., 2009, "Dynamics and stability of lean-premixed swirl-stabilized combustion," Prog Energ Combust, 35(4), pp. 293-364.

[26] Renard, P. H., Thévenin, D., Rolon, J. C., and Candel, S., 2000, "Dynamics of flame/vortex interactions," Prog Energ Combust, 26(3), pp. 225-282.

[27] Smith, D. A., 1985, "COMBUSTION INSTABILITY SUSTAINED BY UNSTEADY VORTEX COMBUSTION," AIAA paper (New York, N.Y. : 1966).

[28] Poinsot, T. J., 1987, "Vortex-driven acoustically coupled combustion instabilities," J Fluid Mech, 177, pp. 265-292.

[29] Schadow, K. C., and Gutmark, E., 1992, "Combustion instability related to vortex shedding in dump combustors and their passive control," Prog Energ Combust, 18(2), pp. 117-132.

[30] Ducruix, S., Durox, D., and Candel, S., 2000, "Theoretical and experimental determinations of the transfer function of a laminar premixed flame," P Combust Inst, 28(1), pp. 765-773.

[31] Fleifil, M., Annaswamy, A. M., Ghoneim, Z. A., and Ghoniem, A. F., 1996, "Response of a laminar premixed flame to flow oscillations: A kinematic model and thermoacoustic instability results," Combust Flame, 106(4), pp. 487-510.

[32] Durox, D., Schuller, T., and Gandel, S., 2002, "Self-induced instability of a premixed jet flame impinging on a plate," P Combust Inst, 29(1), pp. 69-75.

[33] Zinn, T. L. a. B. T., 1998, "The role of equivalence ratio oscillations in driving combustion instabilities in low NOx gas turbines," In 27th Symposium (International) on Combustion/The Combustion Institute, pp. 1809-1816.

[34] Lee, J. G., Kim, K., and Santavicca, D. A., 2000, "Measurement of equivalence ratio fluctuation and its effect on heat release during unstable combustion," P Combust Inst, 28(1), pp. 415-421.

[35] Lieuwen, T., Torres, H., Johnson, C., and Zinn, B. T., 2001, "A Mechanism of Combustion Instability in Lean Premixed Gas Turbine Combustors," Journal of Engineering for Gas Turbines and Power, 123(1), pp. 182-189.

[36] Ducruix, S., Schuller, T., Durox, D., and Candel, S., 2005, "Combustion instability mechanisms in premixed combustors," Combustion Instabilities in Gas Turbine Engines, T. Lieuwen, and Yang, V., ed., AIAA Press, Reston, VA.

[37] Lieuwen, B. T. Z. a. T. C., 2005, "Combustion Instabilities: Basic Concepts," Combustion Instabilities in Gas Turbine Engines, T. C. a. Y. Lieuwen, Vigor ed., AIAA.

[38] Lieuwen, T., and Yang, V, 2005, Combustion Instabilities in Gas Turbine Engines AIAA.

[39] Broda, J. C., Seo, S., Santoro, R. J., Shirhattikar, G., and Yang, V., 1998, "An experimental study of combustion dynamics of a premixed swirl injector," Twenty-Seventh Symposium (International) on Combustion, Vols 1 and 2, pp. 1849-1856.

[40] Richards, G. A., and Janus, M. C., 1998, "Characterization of Oscillations During Premix Gas Turbine Combustion," Journal of Engineering for Gas Turbines and Power, 120(2), pp. 294-302.

[41] Moeck, J. P., Bourgouin, J.-F., Durox, D., Schuller, T., and Candel, S., 2012, "Nonlinear interaction between a precessing vortex core and acoustic oscillations in a turbulent swirling flame," Combust Flame, 159(8), pp. 2650-2668.

[42] Lieuwen, T. C., 2002, "Experimental Investigation of Limit-Cycle Oscillations in an Unstable Gas Turbine Combustor," J Propul Power, 18(1), pp. 61-67.

[43] Bernier, D., Lacas, F., and Candel, S., 2004, "Instability Mechanisms in a Premixed Prevaporized Combustor," J Propul Power, 20(4), pp. 648-656.

[44] Yoon, C., Huang, C., Gejji, R., Anderson, W., and Sankaran, V., 2013, "Computational Investigation of Combustion Instabilities in a Laboratory-Scale LDI Gas Turbine Engine," 49th AIAA/ASME/SAE/ASEE Joint Propulsion Conference, American Institute of Aeronautics and Astronautics.

[45] Z.M.Ibrahim, F. A. W. a. S. G. B., 2005, "A Review of Previous Studies of Oscillatory Combustion in Gas Turbines," University of California, San Diego.

[46] McLaughlin, G. F., and Keller, J. J., 1995, "Thermoacoustic oscillations in combustion chambers of gas turbines," Aiaa J, 33(12), pp. 2280-2287.

[47] Polifke, W., Poncet, A., Paschereit, C. O., and DÖBbeling, K., 2001, "RECONSTRUCTION OF ACOUSTIC TRANSFER MATRICES BY INSTATIONARY COMPUTATIONAL FLUID DYNAMICS," J Sound Vib, 245(3), pp. 483-510.

[48] Werner, K., Guenther, W., and Stefan, H., 1999, "Thermoacoustic analysis of annular combustor," 5th AIAA Aeroacoustics ConferenceSeattle, WA.

[49] Ananthkrishnan, N., 2005, "Reduced-order modeling and dynamics of nonlinear acoustic waves in a combustion chamber," Combust Sci Technol, 177(2), pp. 221-247.

[50] Huang, X., and Baumann*, W. T., 2007, "REDUCED-ORDER MODELING OF DYNAMIC HEAT RELEASE FOR THERMOACOUSTIC INSTABILITY PREDICTION," Combust Sci Technol, 179(3), pp. 617-636.

[51] Putnam., A. A., 1971, *Combustion-Driven Oscillations in Industry*, American Elsevier Publishing Company, New York.

[52] Veynante, D. a. P., T., 1997, "Large Eddy Simulation of Combustion Instabilities in Turbulent Premixed Burners," Center for Turbulence Research, Stanford, CA.

[53] Angelberger, C., Veynante, D., and Egolfopoulos, F., 2000, "LES of chemical and acoustic forcing of a premixed dump combustor," Flow Turbul Combust, 65(2), pp. 205-222.

[54] Selle, L., Lartigue, G., Poinsot, T., Koch, R., Schildmacher, K. U., Krebs, W., Prade, B., Kaufmann, P., and Veynante, D., 2004, "Compressible large eddy simulation of turbulent combustion in complex geometry on unstructured meshes," Combust Flame, 137(4), pp. 489-505.

[55] Staffelbach, G., Gicquel, L. Y. M., Boudier, G., and Poinsot, T., 2009, "Large Eddy Simulation of self excited azimuthal modes in annular combustors," P Combust Inst, 32(2), pp. 2909-2916.

[56] Zhao, W., and Frankel, S. H., 2001, "Numerical simulations of sound radiated from an axisymmetric premixed reacting jet," Phys Fluids, 13(9), pp. 2671-2681.

[57] Laverdant, A., and Thévenin, D., 2003, "Interaction of a Gaussian acoustic wave with a turbulent premixed flame," Combust Flame, 134(1–2), pp. 11-19.

[58] Shalaby, H., Laverdant, A., and Thévenin, D., 2009, "Direct numerical simulation of a realistic acoustic wave interacting with a premixed flame," P Combust Inst, 32(1), pp. 1473-1480.

[59] Talei, M., Brear, M. J., and Hawkes, E. R., 2012, "A parametric study of sound generation by premixed laminar flame annihilation," Combust Flame, 159(2), pp. 757-769.

[60] Polifke, W. a. G., A. M. G., 2004, "Order and realizability of impulse response filters for accurate identification of acoustic multi-ports from transient CFD," Int. J. of Acoustics and Vibration, 9(3), pp. 139-148.

[61] Zhu, M., Dowling, A. P., and Bray, K. N. C., 2005, "Transfer Function Calculations for Aeroengine Combustion Oscillations," Journal of Engineering for Gas Turbines and Power, 127(1), pp. 18-26.

[62] Giauque, A., 2008, "Validation of a flame tranfer function reconstruction method for complex turbulent configurations."

[63] Poinsot, T. J., and Lelef, S. K., 1992, "Boundary conditions for direct simulations of compressible viscous flows," J Comput Phys, 101(1), pp. 104-129.

[64] Baum, M., Poinsot, T., and Thévenin, D., 1995, "Accurate Boundary Conditions for Multicomponent Reactive Flows," J Comput Phys, 116(2), pp. 247-261.

[65] Selle, L., Nicoud, F., and Poinsot, T., 2004, "Actual Impedance of Nonreflecting Boundary Conditions: Implications for Computation of Resonators," Aiaa J, 42(5), pp. 958-964.

[66] Polifke, W., Wall, C., and Moin, P., 2006, "Partially reflecting and non-reflecting boundary conditions for simulation of compressible viscous flow," J Comput Phys, 213(1), pp. 437-449.

[67] Rudy, D. H., and Strikwerda, J. C., 1980, "A nonreflecting outflow boundary condition for subsonic navier-stokes calculations," J Comput Phys, 36(1), pp. 55-70.

[68] Martin, M. P., 2007, "Direct numerical simulation of hypersonic turbulent boundary layers. Part 1. Initialization and comparison with experiments," J Fluid Mech, 570, pp. 347-364.

[69] Schuermans, B., Luebcke, H., Bajusz, D., and Flohr, P., 2005, "Thermoacoustic Analysis of Gas Turbine Combustion Systems Using Unsteady CFD," ASME Conference Proceedings, 2005(4725X), pp. 287-297.

[70] Huber, A., Romann, P., and Polifke, W., 2008, "Filter-Based Time-Domain Impedance Boundary Conditions for CFD Applications," ASME Conference Proceedings, 2008(43130), pp. 901-911.

[71] Silva, C. F., Durán, I., Nicoud, F., and Moreau, S., 2014, "Boundary Conditions for the Computation of Thermoacoustic Modes in Combustion Chambers," Aiaa J, 52(6), pp. 1180-1193.

[72] Kaufmann, A., Nicoud, F., and Poinsot, T., 2002, "Flow forcing techniques for numerical simulation of combustion instabilities," Combust Flame, 131(4), pp. 371-385.

[73] Duchaine, F., Boudy, F., Durox, D., and Poinsot, T., 2011, "Sensitivity analysis of transfer functions of laminar flames," Combust Flame, 158(12), pp. 2384-2394.

[74] Hermeth, S., Staffelbach, G., Gicquel, L. Y. M., and Poinsot, T., 2013, "LES evaluation of the effects of equivalence ratio fluctuations on the dynamic flame response in a real gas turbine combustion chamber," P Combust Inst, 34(2), pp. 3165-3173.

[75] Saltelli, A., Chan, K., and Scott, E. M., 2009, Sensitivity Analysis, Wiley.

[76] Rabitz, H., Kramer, M., and Dacol, D., 1983, "Sensitivity Analysis in Chemical Kinetics," Annual Review of Physical Chemistry, 34(1), pp. 419-461.

[77] Giovangigli, V., and Smooke, M. D., 1993, "Application of Continuation Methods to Plane Premixed Laminar Flames," Combust Sci Technol, 87(1-6), pp. 241-256.

[78] Magri, L., and Juniper, M. P., 2013, "Sensitivity analysis of a time-delayed thermo-acoustic system via an adjoint-based approach," J Fluid Mech, 719, pp. 183-202.

[79] Magri, L., and Juniper, M., 2014, "Adjoint-based linear analysis in reduced-order thermo-acoustic models," International Journal of Spray and Combustion Dynamics, 6(3), pp. 225-246.

[80] Lutz, A. E., Kee, R. J., and Miller, J. A., 1988, "SENKIN: A Fortran program for predicting homogeneous gas phase chemical kinetics with sensitivity analysis," No. SAND-87-8248; Other: ON: DE88006928 United StatesOther: ON: DE88006928Wed Feb 06 20:48:29 EST 2008NTIS, PC A03/MF A01; 1.SNL; EDB-88-067169English.

[81] Borggaard, J., and Burns, J., 1997, "A PDE Sensitivity Equation Method for Optimal Aerodynamic Design," J Comput Phys, 136(2), pp. 366-384.

[82] Andrew, G., William, E., and Eugene, C., 1998, "Using sensitivity equations for chemically reacting flows," American Institute of Aeronautics and Astronautics.

[83] Borggaard, J., and Verma, A., 2000, "On Efficient Solutions to the Continuous Sensitivity Equation Using Automatic Differentiation," SIAM Journal on Scientific Computing, 22(1), pp. 39-62.

[84] Hristova, H., Étienne, S., Pelletier, D., and Borggaard, J., 2006, "A continuous sensitivity equation method for time-dependent incompressible laminar flows," Int J Numer Meth Fl, 50(7), pp. 817-844.

[85] Turgeon, É., Pelletier, D., Borggaard, J., and Etienne, S., 2007, "Application of a sensitivity equation method to the k-ε model of turbulence," Optimization and Engineering, 8(4), pp. 341-372.

[86] Pelletier, D., Hay, A., Etienne, S., and Borggaard, J., 2008, "The sensitivity equation method in fluid mechanics," European Journal of Computational Mechanics, 17(1-2), pp. 31-61.

[87] Giguère, J.-S., Ilinca, F., and Pelletier, D., 2010, "Finite element and sensitivity analysis of thermally induced flow instabilities," Int J Numer Meth Fl, 63(10), pp. 1167-1192.

[88] Margolis, S. B., 1980, "Bifurcation Phenomena in Burner-Stabilized Premixed Flames," Combust Sci Technol, 22(3-4), pp. 143-169.

[89] "The Engineering Toolbox-Convective Heat Transfer ", http://www.engineeringtoolbox.com/convective-heat-transfer-d_430.html.

[90] Turns, S. R., 2000, An introduction to combustion: concepts and applications, The McGraw-Hill Companies, Inc. , Singapore.

[91] ANSYS FLUENT 12.0/12.1 Documentation, ANSYS, Inc.

[92] PANTANO, C., 2004, "Direct simulation of non-premixed flame extinction in a methane–air jet with reduced chemistry," J Fluid Mech, 514, pp. 231-270.

[93] Hou, Y., and Mahesh, K., 2005, "A robust, colocated, implicit algorithm for direct numerical simulation of compressible, turbulent flows," J. Comput. Phys., 205(1), pp. 205-221.

[94] Doom, J. J., 2009, "Direct numerical simulation of turbulent, chemically reacting flows," Ph.D. Dissertation, University of Minnesota.

[95] PIERCE, C. D., 2001, "Progress-variable approach for large-eddy simulation of turbulent combustion," Ph.D. Dissertation.

[96] Wall, C., Pierce, C. D., and Moin, P., 2002, "A Semi-implicit Method for Resolution of Acoustic Waves in Low Mach Number Flows," J Comput Phys, 181(2), pp. 545-563.

[97] Casulli, V., and Greenspan, D., 1984, "Pressure method for the numerical solution of transient, compressible fluid flows," Int J Numer Meth Fl, 4(11), pp. 1001-1012.